1-1-2011

Simulation Of A Convective Loop For The NTED™ Low Energy House

Ian Stahlbrand
Ryerson University

SIMULATION OF A CONVECTIVE LOOP FOR THE NTED™ LOW ENERGY HOUSE

by

Ian Stahlbrand, B.Sc. Engineering Physics, Queen's University, 2008

A thesis

presented to Ryerson University

In partial fulfillment of the

requirements for the degree of

Master of Applied Science

in the Program of

Building Science

Toronto, Ontario, Canada, 2011

AUTHOR'S DECLARATION

I hereby declare that I am the sole author of this thesis.

I authorize Ryerson University to lend this thesis to other institutions or individuals for the purpose of scholarly research.

I further authorize Ryerson University to reproduce this thesis by photocopying or by other means, in total or in part, at the request of other institutions or individuals for the purpose of scholarly research.

ABSTRACT

Simulation of a Convective Loop for the NTED™ Low Energy House

Ian Stahlbrand

M.A.Sc. Building Science, Ryerson University, 2011

The Nested Thermal Envelope Design (NTED™) is an innovative low energy house design that incorporates two thermal envelopes to create a core and perimeter zone. The perimeter acts as a thermal buffer zone, where heat loss from the core and solar gain in the perimeter is recovered to the core via an inter-zone heat pump. In order to optimize heat recovery from the perimeter and minimize temperature stratification, a complete loop is formed around the core living space, through which air may flow in a convective loop. A simplified convective loop was modelled with a commercial CFD software package. Simulations show the convective loop distributes solar gains and reduces temperature stratification in the perimeter. The location of the heat pump in the convective loop was found to affect the COP by up to 21%.

ACKNOWLEDGEMENTS

I would like to gratefully acknowledge the funding support and valuable guidance of my supervisor Russell Richman. Thanks as well to David Naylor for providing technical support and valuable resources along the way. As always, I greatly appreciate my parents' financial support and positive influence.

Table of Contents

List of Tables

List of Figures

Nomenclature

a	absorption coefficient (m^{-1})
A	area (m^2)
c_p	specific heat (kJ/kgK)
COP	coefficint of performance
E	specific energy (m^2/s^2)
g	acceleration due to gravity (m/s^2)
h	heat transfer coefficient (W/m^2K)
i	specific energy (m^2/s^2)
I	radiation intensity (W/m^2)
k	thermal conductivity (W/mK)
K	specific turbulent kinetic energy (m^2/s^2)
L	characteristic length (m)
m	mass (kg)
P	pressure (Pa)
Q	heat flux (W/m^2)
S	energy source term (W/m^3)
S_{ij}	rate of fluid deformation (s^{-1})
$SHGC$	solar heat gain coefficient
T	temperature (^oC)
u	velocity (m/s)
u^+	dimensionless velocity
u'	velocity fluctuation (m/s)
$\overline{u'}$	time averaged velocity fluctuation (m/s)
μ_τ	turbulent viscosity (kg/ms)
U	average velocity (m/s)
U_τ	friction velocity (m/s)
v	y-component velocity (m/s)
w	z-component velocity (m/s)
y^+	dimensionless wall distance

Greek letters

α	thermal diffusivity (m^2/s)
α^*	absorptance
β	thermal expansion coefficient (K^{-1})
ϵ	turbulence dissipation rate (m^2/s^3)
ε	emissivity
σ	Stefan-Boltzmann constant (W/m^2K^4)
ρ	density (kg/m^3)
ρ^*	reflectance
τ_w	wall shear stress (kg/ms^2)
τ^*	transmittance
μ	viscosity (kg/ms)
ν	kinematic viscosity (m^2/s)
ϕ	scalar transport
Γ	diffusion coefficient (w/mK)
Δ	gradient operator
Ψ	dissipation function (m^2/s^2)
∇	divergenc operator

Dimensionless groups

Gr	Grashof Number
Nu	Nusselt Number
Pr	Prandtl Number
Ra	Rayleigh Number
Re	Reynolds Number
Re_y	Turbulent Reynolds Number

1 Introduction

Due to environmental imperatives, limited conventional fuel resources, and escalating energy prices, there is increasingly a need to design and build low-energy, more "sustainable" buildings. Buildings represent a great opportunity for reducing energy consumption without compromising occupant comfort or functionality. The NTED™ is an innovative low energy house design developed by Pressnail and Richman (2009) that incorporates two thermal envelopes, one nested within the other. A three-season perimeter space acts as a thermal buffer zone, where heat loss from the core space and solar gain in the perimeter is recovered via an inter-zone heat pump. In the heating season, the perimeter space is maintained at a lower temperature (T = 5^{o}C) and the core is maintained at a comfortable living temperature (T = 21^{o}C). Dixon et al. (2009) showed through detailed building energy simulations that energy savings per unit floor area of 70% are achievable compared to the scenario where both perimeter and core spaces are heated.

1.1 Problem Definition

Building energy simulations by Dixon et al. (2010) assume uniform temperature distribution in the core and perimeter spaces. More specifically, EnergyPlus assumes full mixing and even zone distribution when calculating heat transfer. However, experimental houses have shown high degrees of temperature stratification leading to overheating in the upper floor spaces (Jones et al, 1982). Temperature stratification also has implications for efficiently recovering heat from the perimeter space, since the coefficient of performance (COP) of commercial heat pumps is highly dependent on the air temperature at the evaporator/condenser.

In order to address the issue of uneven heat distribution, the NTED™ was modified to include a closed convective air loop in the perimeter space surrounding the core. The intent of the convective loop is to allow solar heat gains to be distributed around the perimeter space via convective heat transfer. The loop acts as a complex thermosiphon driven by buoyant forces, where heat gain due to solar radiation in the south perimeter cavity tends to drive the flow in a circular loop. Temperature stratification can be minimized by optimizing air flow rates in the loop via natural or forced convection. As a result, the core space is surrounded by a well mixed warm buffer zone, reducing heat loss through both thermal envelopes and allowing the inter-zone heat pump to operate at a higher efficiency (COP).

1.2 Objectives

This work analyzes the use of a closed convective air loop in the perimeter space of the NTED™ house. There is a need for detailed air flow simulation in order to optimize the overall performance of the NTED™ low energy house. Also, although there exists in the literature extensive work on buoyant flows in open and closed cavities (Gan 2006, Rundle et al. 2011, Walsh et al. 2003 etc.), the author is aware of no such study on flows in closed loop cavities. The aim is to address both aspects through detailed computational fluid dynamics (CFD) studies. It is important to note that some research (Reno, 1980) has shown little benefit in a convective loop, suggesting the buffer zone alone may be sufficient in itself to achieve the desired energy savings. This work also will examine the relative importance of the convective loop in the NTED™ design.

1.2.1 Primary Objectives

The primary objectives are to:

1. Create a CFD model to study the convective loop air flow in a simplified building geometry reflecting the proposed NTED™ low energy house
2. Use the model to optimize the convective loop design and maximize the performance of the NTED™ in the heating season; in particular, by optimizing heat recovery from the perimeter space and minimizing temperature stratification

1.2.2 Secondary Objectives

To achieve Primary Objective 1,

1. Analyze the existing work on double envelope houses to inform model considerations
2. Create a simplified building geometry meshed appropriately for simulation in a commercial CFD package.
3. Perform a grid independence study and compare results from different simulation methods in order to verify the models accuracy
3. Apply the model to a second geometry representative of the NTED™ low energy house

To achieve Primary Objective 2,

1. Perform steady state and transient simulations to study natural convective flow over a 24 hour period during the heating season
2. Determine the degree to which natural convection distributes heat throughout the perimeter space during the day and night by examining velocity flow fields and flow rates in the domain
3. Determine the degree of temperature stratification by examining temperature fields in the domain
4. Create a simplified heat pump model and determine how its operation affects the heat distribution in the perimeter space
5. Investigate different heat pump locations in order to optimize heat recovery from the perimeter space

1.3 Outline

In the following sections, studies on the double envelope house, from which the NTED™ draws inspiration, are analyzed to help inform design decisions and the methodology for this research. The NTED™ concept is described in detail which leads to the development of a problem definition and research objectives. The next section includes the relevant theory and literature pertaining to simulating buoyant flow using computational fluid dynamics (CFD) software.

A simplified double envelope house geometry is used to analyze the flow and verify the CFD model's accuracy. The model is then applied to a larger more complex geometry representative of the NTED™ house. Simulations are performed using steady state and transient simulations. Simulation results using different flow models are also compared. Finally, a heat pump model is incorporated into the NTED™ house model and results assessing the heat pump's energy performance and effect on heat distribution in the space are presented.

2 Background

2.1 The Double Envelope House

2.1.1 Concept

The double-envelope house, also referred to as a double-shell, double-wall, thermal envelope, or simply envelope house, is a passive solar building design characterized by two envelopes, i.e. a house within a house. The house typically has two northern and southern walls, an inner and outer roof, an under floor space, and single east and west walls. A complete loop cavity is formed around the inner living space, through which air may flow passively in a convective loop. The principle of operation is that the loop acts as a complex thermosiphon driven by buoyant forces. Heat gain due to solar radiation in the south cavity and heat loss in the north side and basement tend to drive the flow in a circular loop (counter clockwise for the orientation shown in Figure 2.1. The intent of the convective loop is to surround the building with a warm air layer or buffer zone, reducing temperature gradients across each envelope. Many designs incorporate sensible thermal storage, generally in the form of thermal mass in the basement or lower portion of the convective loop to store excess heat during the day. Several hundred double-envelope homes were built during the late 70's and early 80's.

2.1.2 Experimental House Studies

2.1.2.1 Mastin House

The Mastin house is an Ekose'a designed double-envelope house built by Robert Mastin in Middletown, Rhode Island in early 1979. The three story, 242 m^2 house has an outer shell consisting of a two story attached solarium and basement utility room, as shown in Figure 2.1. The outer walls are of 2 x 6 in. wood frame construction with RSI-3.3 (R-19) fibreglass batt insulation and the inner walls are of 2 x 4 in. construction with RSI-1.9 (R-11) batt. The south elevation has 48m^2 of glazing, 2/3 of which are on the 45^o sloped roof.

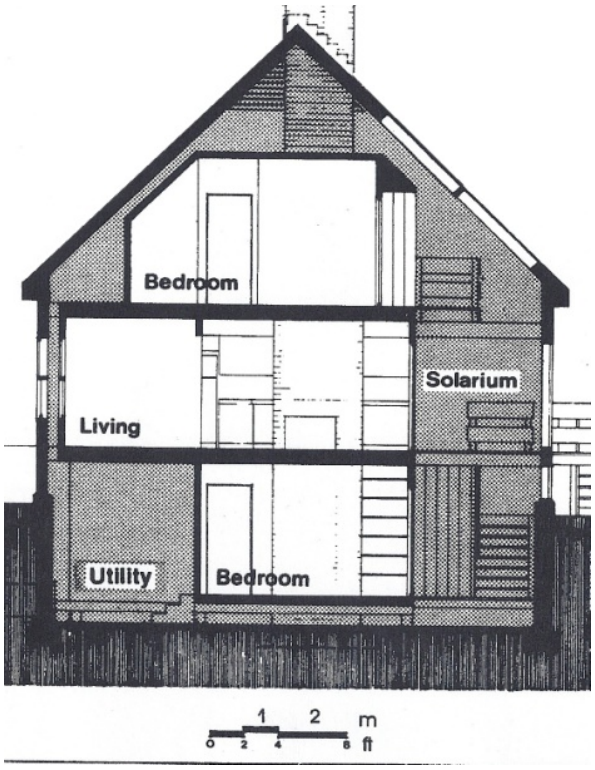

Figure 2.1 - Section of the Mastin double-envelope house (Jones et al., 1982)

Brookhaven National Laboratory (BNL) performed experimental measurements on the house in the winter of 1980 and analysed the results to evaluate the performance of the house and gain insight into its operation (Jones et al. 1982). The report was one of the few rigorous experimental studies on the subject. The parameters measured were the temperature throughout the house, the ambient temperature, and the insolation.

The occupied house was maintained at 18C during the three month testing period using temperature controlled 1500W electric heaters on each floor. The energy usage of the electric heaters was logged to determine the auxiliary heat required for the house, a measurement technique known as the electric co-heating method. During sunny days in January the attic reached up to 41C, while the bottom loop was maintained at 7-13C. It was concluded that natural convection led to a high degree of stratification where upper occupied levels overheat and lower levels require auxiliary heating. One of the most important results from the experiments is that when the convective loop was blocked, there was no increase in auxiliary heat required; indicating that the convective loop did not contribute to energy savings. However, the authors' indicate that perhaps closing the loop had no adverse effects because of isolated convective air circulation in the north and south cavities.

Minimal heat storage was apparent in the basement slab based on temperature measurements at different depths. Insignificant ground storage was also found at the Tom Smith House in Lake Tahoe, and the Stokes House in Canton, Georgia. It is clear that the ground coupling storage method is ineffective, and a more substantial storage system such as a rock or gravel bed would be necessary. Measurements of air flow were less than ~0.5m/s

and provided no conclusive evidence of a convective loop. Based on the authors' calculations, approximately 8.8kW (the heating design load) would be transported to the crawl space with forced circulation at 28m^3/min. Forced circulation would also lead to more uniform temperatures in the convective loop and allow for more substantial energy storage. Another reason for the ineffectiveness of the convective loop and storage may have been due to opening the internal doors to the solarium when its temperature was higher than inside. The authors' concluded that the low energy needs of the house are mainly attributed to the excellent insulation value gained by using a double envelope.

The main advantage of the design is the ability to provide large areas of south glazing, excellent natural daylighting, and an attractive solarium which can be enjoyed through most of the year. Other advantages include very low air infiltration, increased comfort due to radiation exchange with the warmer walls, and high sound attenuation.

2.1.2.2 Mastin House - Forced Circulation

Ghaffari et al. (1981) examined the possibility of forced circulation as an extension to the Mastin House experiments. Experiments were conducted in the Mastin house with two small 1/8 hp blowers installed in the attic. The amount of ground storage was not substantial, but did noticeably diminish the ground thermal losses. A hypothetical model was then simulated with a well insulated 10 by 15 foot parallelepiped shaped hypocaust consisting of a feolite slab (iron-oxide compound used extensively in storage systems in the UK) with multiple flow channels. A Fourier series transient solution for thermal exchanges in the slab was utilized for air velocity of ~0.25m/s. The authors' determined that the total thermal storage would be very significant, on the order of 8 times that of the ground concrete slab thermal storage.

Reno (1980) analyzed the basic physics of the double-envelope house, similar to the Ekose'a design. He notes that for the convective loop to function as intended, heat must be lost through the north wall, and is thus inherently inefficient. Furthermore there is significant thermal loss through the large glazing as later confirmed in the BNL Mastin house experiments. Allowing air to convect over the ground surface is a highly inefficient method of transferring energy, as the hot air will stratify under the floor. Earth coupling does however have an advantage in that heat from the earth acts to moderate the air temperature as it cools. Reno suggests eliminating the open loop, and using forced convection to remove excess heat from the solarium to an insulated storage, while maintaining earth contact for the tempering effect.

2.1.2.3 Demmel House

Chen et al. (1981) monitored the performance of the Demmel Double-Shell Home in Hartington, Nebraska, modelled after the Mastin home in Rhode Island. The authors' found no internal convective loops in the cavities and measured flow due to natural convection at up to 0.1m/s during the day and was proportional to insolation. At night the flow approximately doubled that of the days and in the reverse direction. As in the Mastin house,

insignificant thermal storage was measured. Heat transfer models indicated that heat migration from the earth in the crawl space to the convective air loop is significant and preliminary results support this. The authors' conclude that the double envelope house is a viable passive solar technique and owners of these houses are pleased with the thermal performance.

2.1.2.4 Bergstedt Residence

A passive solar double envelope house was built in Duluth, Minnesota and monitored by the US DOE (Williams, 1981). The design incorporated 12 in. mass walls as the primary storage and the basement as a secondary storage. It was expected that due to the harsh climate (10,000 HDD), little useable heat would reach the basement storage. This was confirmed by temperature readings. The house performed well with an estimated solar heating fraction of 59%. Based on the experimental results, the author suggested that the double envelope be closed off, pulling heat from the sun space via forced convection directly to the basement storage.

2.1.3 Simulation Studies

Hsu et al. (1981) developed a 1D mathematical model of a simplified 135m^2 two-story double shell solar house with 0.3m separation between envelopes, 32m^2 south glazing, and a 0.1m concrete slab insulated from the ground for thermal storage. The flow was assumed steady and turbulent. In natural convection, the flow is driven by a weight difference between air in the north and south cavities. For constant velocity (steady state), the buoyant force is balanced by the pressure losses due to friction. In the double envelope, the Bernoulli equation simplifies to

$$(\rho_n - \rho_s)gh = f\frac{L}{d}\rho_o\frac{v^2}{2} \quad (1)$$

Where ρ_n and ρ_s are the north and south wall air densities respectively, $\rho_o$is the average air density, f is the friction factor, L is the path length, d is the hydraulic diameter, and v is the air velocity. An energy balance was performed on a control volume and integrated over the convective loop. The velocities and temperatures in the loop were determined using the energy balance and Equation (1) through an iterative guessing process. The model was simulated with an insolation of 400W/m^2, resulting in an air velocity between 0.17m/s and 0.45m/s depending on the ambient temperature. The velocity of flow in the reverse direction was nearly the same when the insolation was zero. The temperature rise in the concrete slab floor was ~5C, yielding a 7% savings compared to a system without storage. The authors' found that forced convection is best for transferring heat to the underground slab.

Allen et al. (1983) created a simplified one dimensional finite difference model of a one story double shell solar house as shown in Figure 2.2 to study the effect of various design parameters. These include the amount of south glazing, amount of insulation in the inner envelope, the thermal storage heat capacity and heat transfer coefficient, and the effect of forced circulation.

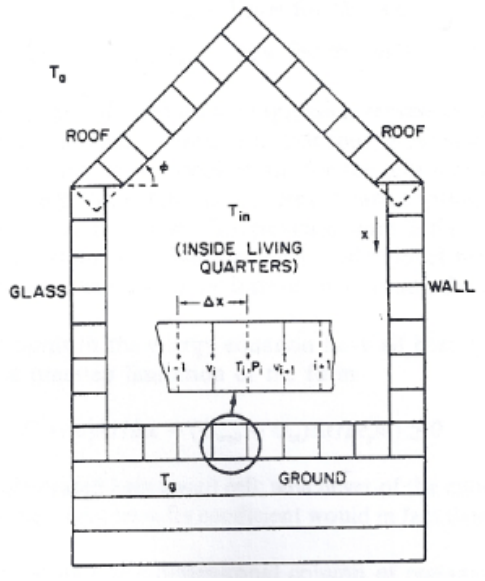

Figure 2.2 - Nodal representation for the double-envelope numerical model

The differential momentum and energy formulations were applied using the finite difference method. A major simplifying assumption is that radiant energy is applied directly to the flow as opposed to being heated convectively by the warm absorber surface. The Boussinesq approximation has been applied which states that the air density is constant except where it appears in terms multiplied by the acceleration due to gravity. This is a common simplification for buoyancy driven flows, i.e. natural convection. The air density is a function of temperature

$$\rho = \rho_o[1 - \beta(T - T_o)] \quad (2)$$

Where β is the coefficient of thermal expansion for air (β= 3.43x10^{-3}K^{-1}).

The authors' found that increasing the insulation in the inner wall, the conductivity of the ground, and the overall heat capacity of the house had a positive effect by dampening the temperature swings in the internal space. The height to which the south wall is glazed greatly reduces the effectiveness of the thermosiphon convective loop. As more glass is added higher up the wall, the effective centre of the heat source rises relative to the heat sink and the maximum air velocity in the loop drops drastically (from approximately 0.45m/s to 0.1m/s). This leads to overheating since the flow has nearly stagnated. Fixing the air velocity at a constant rate, i.e. forced circulation acts to moderate or flatten the temperature distribution over the day as is the intent of the design (Figure 2.3).

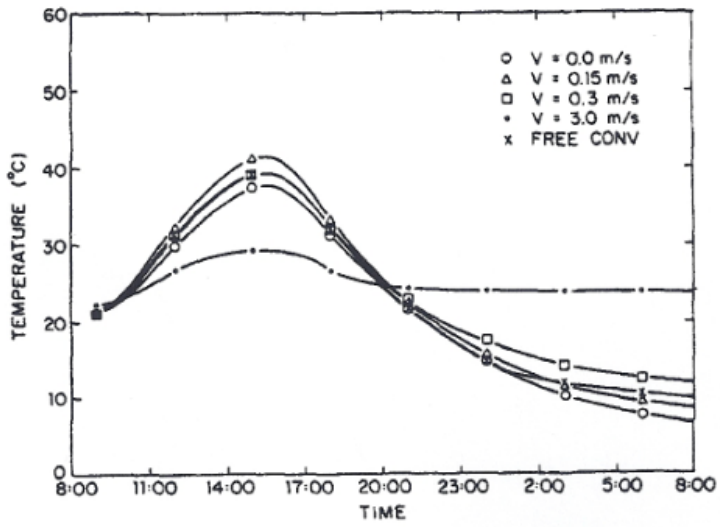

Figure 2.3 - The effect of forced convection on moderating the internal space temperature

The author notes that the 1D model of limited accuracy in that air flow in a wide sunspace may be multidimensional, with up flow near the absorbing surface and down flow near the cooler glass. Also, with only a single node inside the house, the internal temperature distribution is ignored which may be important if stratification effects are predominant. Thermal mass in the house and forced circulation greatly improve the performance of the double shell solar house.

2.1.4 Design Considerations

Experimental and simulation studies on the double envelope house lead to some key results which can inform future designs. First, most of the research points towards the need for forced convection to reduce temperature stratification in the perimeter spaces. Second, thermal storage may be difficult to implement in an effective manner; this points to an alternative method for heat extraction from the convective air loop- the heat pump. Table 2.1 summarizes the key conclusions from the experimental case studies and models described above.

Table 2.1 - Key findings from review of double envelope houses

Case Study	Key Findings
Mastin House (Jones et al. 1982)	Natural convection led to high stratification Convective loop did not contribute to energy savings Minimal heat storage in ground coupling Low flow velocities (< 0.5m/s)
Demmel House (Chen et al. 1981)	Low flow velocities (~0.1m/s) No isolated internal convective loops Minimal heat storage Earth coupling moderates temperature
Bergstedt Residence (Williams et al. 1981)	Minimal heat storage Removing loop and forced convection recommended
Model	**Key Findings**
1D Mathematical Model (Hsu et al. 1981)	Velocities between 0.17-0.45m/s Reverse flow of equal magnitude at night 7% energy savings, forced convection recommended
1D Finite Difference Model (Allen et al. 1983)	Internal space temperature moderated by increasing the inner wall insulation, overall heat capacity of house, and the conductivity of thermal storage Glazing high up on south wall reduces flow velocity Forced circulation effective

2.2 Closed Loop Building Integrated Solar Air Collection Systems

2.2.1 Introduction

Transporting heat from solar collection systems with air is a very old and long practiced idea. Active solar air systems are free of many of the design challenges related to solar hot water collectors and can be integrated with mechanical ventilation systems. The following is a review of relevant systems from the book, *Solar Air Systems: A Design Handbook* (Hastings et al., 2000), a result of contributions from 20 experts from 9 countries working under the IEA Solar Heat and Cooling Programme.

2.2.2 Closed Loop Systems

The active loop solar air collector system integrated with double envelope storage walls have been demonstrated in apartment buildings in Denmark and Sweden. These systems are convenient for retrofits and are well suited for multi storey buildings as shown in Figure 2.5. The collector can be a commercial style flat plate solar air collector ducted to the thermally massive storage walls as shown in Figure 2.4. A sunspace can also be used as a collector to serve as an additional living space with excellent daylighting. The disadvantage of this system is that sunspace collectors are inefficient relative to flat plate collectors (see Figure 2.7).

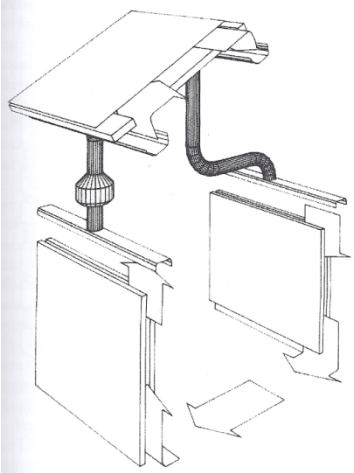

Figure 2.4 - Solar collector with double-envelope storage walls

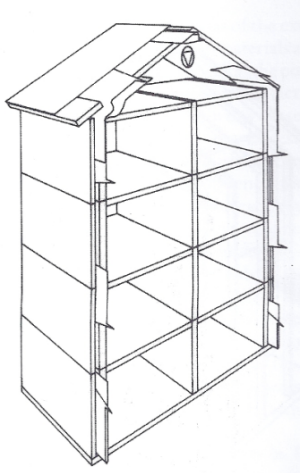

Figure 2.5 - Multi-storey double-envelope

The system in Figure 2.4 was used as a reference system for modelling in TRNSAIR. TRNSAIR was a simulation program based on the widely used dynamic simulation program TRNSYS. The following results and design consideration are based on simulations with this program. (TRNSYS now includes solar air systems as add-ons to the standard package).

The wall construction for the double envelope used in the simulations is shown in Figure 2.6. Hollow concrete blocks provide efficient heat transfer and storage and expanded polystyrene insulation forms the outer envelope minimizing heat loss. The system was modelled with a high insulation (RSI-5.89) and low insulation (RSI-1.72). The simulated saved energy fraction, i.e. the net heat load with and without the solar system in operation for a sunny/cold climate (based on Denver, CO) was up to 70% for a collector area to floor area ratio of 0.15. The net heating load for this system was 35kWh/m^2. Concrete performs better than brick due to a higher thermal conductivity and heat capacity.

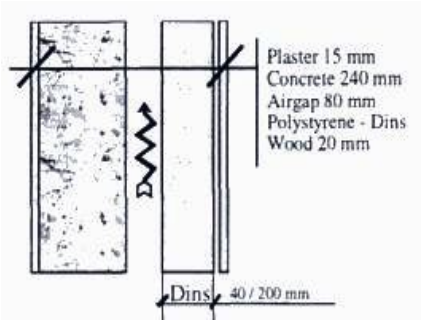

Figure 2.6 - Double-envelope wall construction

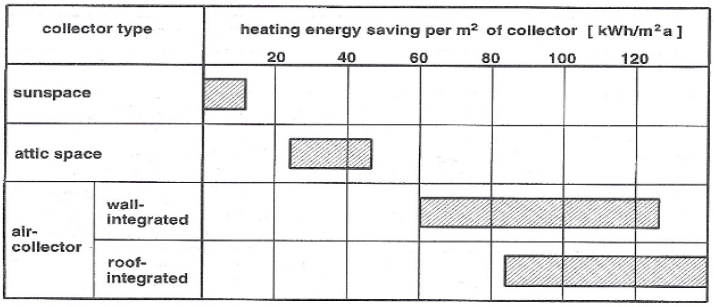

Figure 2.7 - Energy savings for different collector types

Figure 2.7 compares the percentage heating energy saved per m^2 of collector for different air collector systems. The data is based on real systems constructed in Germany and Denmark. Roof and sunspace collectors are much less efficient, as high air temperatures are difficult to achieve. Experience from built examples show that collectors should provide air to storage at >50^{o}C. Incorporating storage within or near heating spaces in buildings is important otherwise storage losses dominate the energy balance. Open loop discharge systems can be made more efficient if combined with ventilation systems, such that discharging occurs with cooler outdoor air.

2.2.3 Thermal Storage

Closed collection loops can be integrated with thermal storage units often located under floors or in a basement space. Thermal storage is generally in the form of a rock bed, hypocaust, thermal mass floor/wall, or phase change material (PCM). Rock beds are among the most common and require forced circulation due to high pressure losses. The pressure drop as a function of air velocity, rock diameter, and also the bed length required for full heat transfer is shown in Figure 2.8.

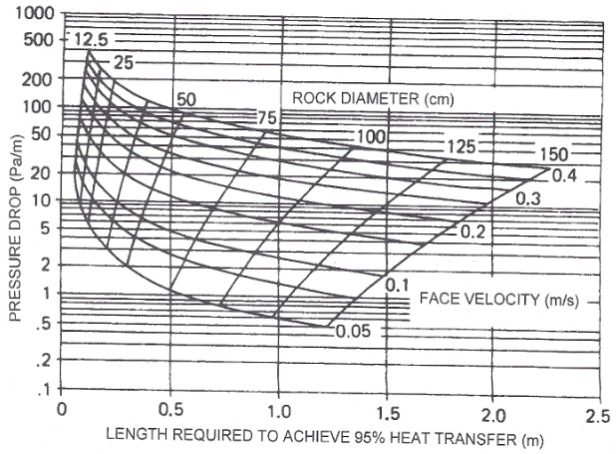

Figure 2.8 - Pressure drop and critical depth for varying stone size and flow velocity

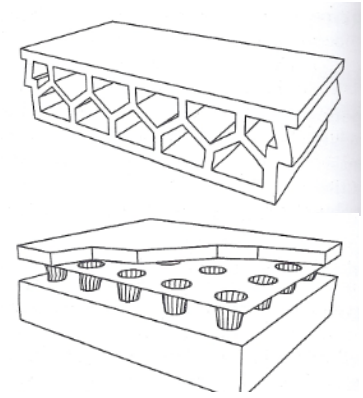

Figure 2.9 - Common hypocaust designs

A hypocaust is a massive floor slab generally made of concrete with air channels through the structure. It is based on an ancient roman system for space heating where the floor is raised by distributed small pillars, creating an under floor space for channelling hot air. A murocaust is a similar system for a wall. Figure 2.9 illustrates common hypocaust geometries and Figure 2.10 shows the system schematic. These systems are also generally used with forced circulation (40-70m^3/h/m^2 collector) for higher efficiency. The radiant discharge of the hypocaust can improve thermal comfort, but the floor temperatures should be maintained below 26^{o}C.

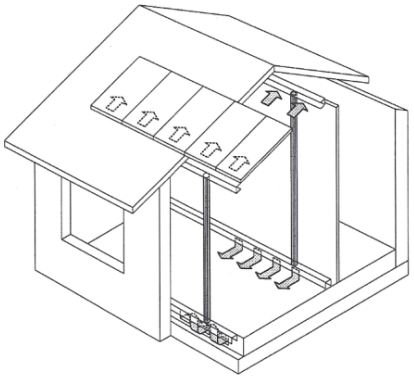

Figure 2.10 - Roof collector with hypocaust thermal storage

Hypocausts are defined by the characteristic time, τ at which point 63% of the energy absorbed is released to the space. For an uninsulated hypocaust, τ is approximately 5 – 17 hours. By insulating the hypocaust storage, τ can be many days. Hypocaust storage units result in far lower air pressure drops and have slightly higher efficiencies than rock beds. Hypocausts have a greater heat capacity per volume than rock beds however rock beds compensate with a higher coefficient of heat transfer.

2.2.4 Conclusions

The work presented by Hastings et al. (2000) provides a more detailed analysis of a more updated version of the double envelope house. The performance of the double envelope house is best when a flat plate solar air heater is integrated with thermal storage walls or a hypocaust floor. Sunspaces can be at least 4 times less efficient than flat plate or wall/roof integrated collectors. The systems presented avoid the use of atria/sunspaces and use forced circulation to drive the solar heated air through small cavities.

2.3 NTED™

2.3.1 Concept

Pressnail et al. (2009) developed an innovative low energy house design that incorporates two nested thermal envelopes (NTED™). A three-season perimeter space acts as a thermal buffer zone, where heat loss from the core space and solar gain in the perimeter is recovered via a heat pump. The core space contains the primary rooms of the house including bedrooms, a bathroom, kitchen, and family room and is maintained at a comfortable temperature year-round (20^{o}C). Many rooms such as dining rooms, laundry rooms, spare bedrooms, living rooms, etc. not used on a daily basis are located in the perimeter space held at 5^{o}C. Operating the core and perimeter spaces at different temperatures is termed the 'Gemini' mode. As a result the temperature gradient across the external/perimeter envelope would be greatly reduced yielding huge potential energy savings.

2.3.2 Simulation

Pressnail et al. (2009) demonstrated through preliminary HOT2000 simulations that energy savings on the order of 70% or better can be realistically achieved in the winter heating season relative to the R-2000 house construction standard. Of course, the house could be operated in 'Traditional' mode, where both the core and perimeter spaces are heated to a comfortable temperature. In this case, more modest energy savings are achieved due to the effective R-value in the core from the combined two envelopes. Nested thermal envelopes provide residents with the flexibility to choose how they live in the available space based on lifestyle and energy costs.

Dixon et al. (2010) continued the work of Pressnail et al. (2009) by performing detailed building energy simulation for the heating season using the US Department of Energy's EnergyPlus whole building energy simulation program. The author modified the EnergyPlus source code to allow a heat pump to operate between different thermal zones in a building instead of only between a zone and the exterior. Example heating and cooling loads using this model were analyzed to verify the accuracy of the modified inter-zone heat pump model. In the Traditional mode of operation for a 144m^2 house (equal core and perimeter areas), the heating energy use was 61kWh/m^2, compared to 18kWh/m^2 in Gemini mode, a savings of 70%. Figure 2.11 shows the total energy use in the heating season for the Gemini and Traditional modes of operation. A 'Moderate' operational mode was included where the Gemini mode is used during weekdays and Traditional mode used on weekends and holidays.

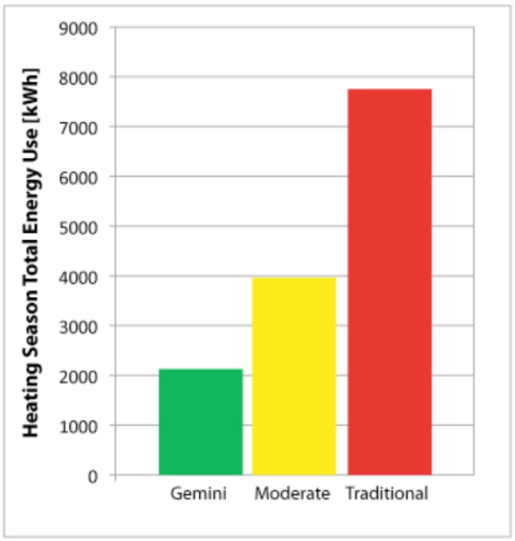

Figure 2.11 – Heating season energy use for various operating modes (Dixon et al., 2009)

Based on equipment performance data and operating temperatures, the inter-zone heat pump was able to operate at a COP between 3.4 and 3.8. No supplementary heating was necessary to maintain the perimeter temperature setpoint.

NTED™ is a particularly promising technology in that it is suitable for both new construction and renovation. A second envelope could be retrofitted to an existing building or alternatively an existing internal space could be renovated to create nested envelopes. Thus, NTED™ has applicability for a large number of buildings and has the potential to significantly reducing energy consumption in the building sector.

The NTED™ concept is expected to be applied to an existing residential building in Toronto, Canada. The building and its section shown in Figure 2.12, is located at 31 Sussex Avenue on the property of the University of Toronto and will be inhabited and monitored by students to gain further insight on its performance.

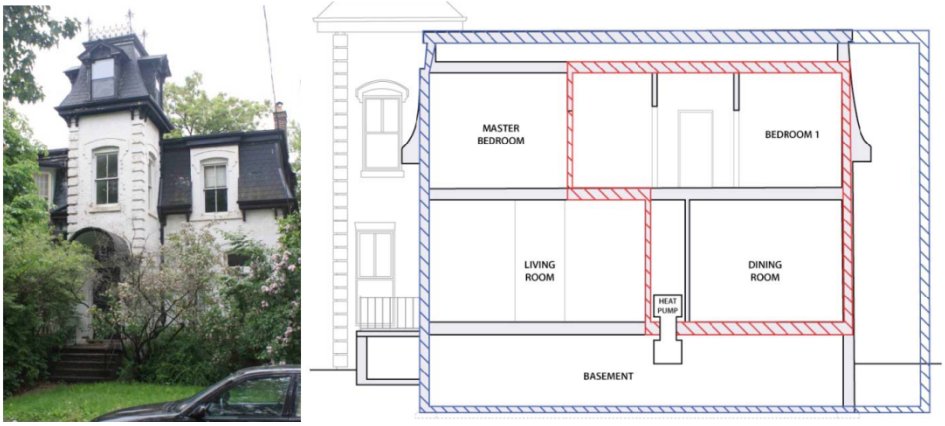

Figure 2.12 – NTED experimental house and section schematic (Dixon et al., 2009)

As shown in the section drawing in Figure 12, the preliminary schematic design incorporates a complete closed perimeter loop surrounding the core space (outlined in red). The intent of the work presented in this thesis is to combine the NTED™ concept with the convective loop concept of the double envelope house. This design negates the need for thermal storage as excess heat is extracted from the perimeter to the core via the heat pump.

3 Theory

3.1 Convective Heat Transfer

In convective heat transfer in general, the important dimensionless parameters are the following: the Reynolds number, defined as the ratio of inertial to viscous forces, the Nusselt number Nu, defined as the ratio of the convective to conductive heat transfer across a boundary, the Prandtl number Pr, which relates the momentum diffusivity to the thermal diffusivity, and the Stanton number St, which measures the ratio of the heat transfer to the thermal capacity of a fluid,

$$Re = \frac{\rho U L}{\mu} \qquad Nu = \frac{Lh}{k} \qquad (3), (4)$$

$$\text{Pr} = \frac{c_p \mu}{k} \qquad St = \frac{h}{c_p \rho U} \qquad (5), (6)$$

$$Nu = Re \cdot Pr \cdot St \qquad (7)$$

Where L is the characteristic length, h is the convective heat transfer coefficient, k is the conductivity, c_p is the heat capacity, μ is the dynamic viscosity, and U is the air velocity

For fully developed duct flow between parallel plates of width *w* and depth *l*, where *w*<<*l*, the hydraulic diameter d, is

$$L = 2w \qquad (8)$$

3.2 Buoyant Flow

Buoyancy driven flow or natural convection occurs when temperature changes occurring in a fluid cause corresponding changes in density. Flow can be induced due to the gravitational force acting on fluid regions of different density. The Grashof number measures the ratio of the buoyant to viscous forces

$$\text{Gr} = \frac{g\beta\Delta T L^3}{v^2} \qquad (9)$$

Where v is the kinematic viscosity, L is the length scale, and β is the thermal expansion coefficient,

$$\beta = -\frac{1}{\rho}\left(\frac{\partial \rho}{\partial T}\right) \qquad (10)$$

The importance of buoyancy in a mixed convection (natural and forced) flow can be determined by the ratio of the Grashof and Reynolds numbers:

$$\frac{Gr}{Re^2} = \frac{g\beta\Delta TL}{U^2} \tag{11}$$

When this ratio is greater than or equal to unity, it expected that buoyant forces contribute strongly to the flow. When this ratio is much less than unity, buoyant forces may be negligible. In natural convection, the important of buoyancy can be determined by the Rayleigh number

$$Ra \equiv Gr \cdot Pr \tag{12}$$

$$Ra = \frac{g\beta\Delta TL^3\rho}{\mu\alpha} \tag{13}$$

where α is the thermal diffusivity

$$\alpha = \frac{k}{\rho c_p} \tag{14}$$

In general the transition to turbulence occurs over the range of $10^8 < Ra < 10^{10}$.

When solving flow fields with buoyant forces, the Boussinesq approximation is often applied. The Boussinesq approximation states that the air density is constant except where it appears in terms multiplied by the acceleration due to gravity. This is a common simplification for buoyancy driven flows, i.e. natural convection. In the appropriate terms, the air density becomes a function of temperature

$$\rho = \rho_o[1 - \beta(T - T_o)] \tag{15}$$

Where ρ_o and T_o are the operating density and temperature. This approximation is valid as long as density variations are small or specifically when

$$\beta(T - T_o) \ll 1 \tag{16}$$

3.3 CFD Theory

3.3.1 The Control Volume Method

Computational fluid dynamics is a powerful tool for modelling systems involving fluid flow, heat transfer, chemical reactions, combustion, etc., with a wide range of applications. CFD has been a prominent design and analysis tool in the aerospace industry for decades especially for aerodynamics. It is now a tool used in such areas as electronics engineering (cooling), turbomachinery, atmospheric science, and heating, ventilating and air-conditioning (HVAC)

in buildings. CFD is really a computer-aided engineering (CAE) tool which can provide flexible, cost-effective simulation for complex systems without the need for physical experiments.

Commercial CFD packages contain three main elements: the pre-processor, solver, and post-processor.

i. Pre-processor:

The pre-processor consists of creating the computational domain (geometry), generation of control volume elements in the form of a grid or mesh, problem definition and boundary conditions.

The governing fluid equations are solved at each node of each cell or control volume in a mesh. The mesh often defines the computational resources (time, computer hardware) required to solve the domain. In general, finer or more refined meshes are required in areas of the domain where the flow is expected to change most significantly. Defining the domain and generating an appropriate mesh can generally require over half the amount of time and work spent on a given problem.

ii. Solver:

The finite-volume method is central to most commercial CFD codes including ANSYS Fluent and ANSYS CFX. The finite element and finite difference methods are other numerical solution techniques which will not be discussed.

The algorithm basically involves three steps: integrating the governing equations on the individual control volumes, discretization of the equations into a system of algebraic equations, and finally solving the algebraic equations using an iterative method.

iii. Post-processor:

Graphical results are a major component of data analysis. Line, vector, and contour plots, particle tracking, and animations help visualize results.

(Versteeg et al. 2007)

3.3.2 Governing Equations

Computational fluid dynamics follows the governing equations for fluid flow based on the classic conservation laws, i.e. conservation of mass, conservation of momentum (Newton's second law), and conservation of energy. The fluid is described by its macroscopic properties such as velocity, pressure, density, and temperature. Structures and motion on the microscopic scale are ignored, or in other words, a continuum approach is used to describe the fluid behaviour. The most general form of the mass conservation or continuity equation for an unsteady compressible fluid in three-dimensions is

$$\frac{\partial \rho}{\partial t} + \nabla(\rho \boldsymbol{u}) = 0 \tag{17}$$

where ρ is the fluid density, $\boldsymbol{u}$ is the velocity vector $\boldsymbol{u} = u\hat{\boldsymbol{i}} + v\hat{\boldsymbol{j}} + w\hat{\boldsymbol{k}}$, and ∇ is the divergence.

$$\nabla(\rho\boldsymbol{u}) = div(\rho\boldsymbol{u}) = \frac{\partial(\rho u)}{\partial x} + \frac{\partial(\rho v)}{\partial x} + \frac{\partial(\rho w)}{\partial x} \tag{18}$$

The continuity equation states that the rate of change over time of mass in a fluid element is equal to the net rate of mass flow into/out of the element. Please refer to Versteeg, H.K., et al. (2007) for a full derivation of these equations.

The momentum equation is based on Newton's second law, which states that the rate of change in the momentum of a fluid element is equal to the sum of the forces on the element.

$$\rho\frac{Du}{Dt} = \frac{\partial(\rho u)}{\partial t} + \nabla(\rho u\boldsymbol{u}) = \sum F_x \tag{19}$$

Where F_x is the force per unit volume in the x-direction and D is the total or substantive derivative. These forces could be due to pressure, gravity, or shear forces due to viscous effects. Accounting for shear stress and pressure forces, the momentum equation in the x-direction becomes

$$\frac{\partial(\rho u)}{\partial t} + \nabla(\rho u\boldsymbol{u}) = -\frac{\partial p}{\partial x} + \nabla(\mu\Delta u) + S_{Mx} \tag{20}$$

Where p is the pressure, μ is the fluid viscosity, Δu is the gradient vector, and S_{Mx} is an x-momentum source. If gravity is acting the x-direction, this is accounted for with S_{Mx}=-ρg. The x, y, and z momentum equations form the Navier-Stokes equations.

The energy equation is based on the first law of thermodynamics, which states that the rate of change of energy for a fluid element is equal to the net heat added to the element plus the work done on the element. The total energy E is

$$E = i + \frac{1}{2}(u^2 + v^2 + w^2) \tag{21}$$

where *i* is the internal energy. The energy equation based on *i* is

$$\rho\frac{Di}{Dt} = \frac{\partial(\rho i)}{\partial t} + \nabla(\rho i\boldsymbol{u}) = -p\nabla\boldsymbol{u} + \nabla(k\Delta\mathrm{T}) + \Psi + \mathrm{S_i} \tag{22}$$

Where k is the conductivity, Ψ is the dissipation function, T is the temperature, and S_i is an internal energy source. In words this equation can be written as

Rate of increase of energy in fluid element	=	Rate of work done by surface stresses	+	Rate of heat addition due to conduction	+	Rate of heat loss due to viscous dissipation	+	Rate of internal heat generation due to a source

A general equation can be written in a similar form to the energy equation for any scalar quantity including temperature, turbulence energy, etc. The equation for a general scalar variable ϕ is termed the transport equation for ϕ

$$\frac{\partial(\rho\phi)}{\partial t} + \nabla(\rho\phi\boldsymbol{u}) = \nabla(\Gamma\Delta\phi) + S_\phi \tag{23}$$

where Γ is the diffusion coefficient and S_ϕ is a source term.

Rate of increase of ϕ in fluid element	+	Rate of change in ϕ due to convection	=	Rate of change in ϕ due to diffusion	+	Rate of change of ϕ due to sources		

3.3.3 Turbulence

Laminar fluid flow is flow which is streamlined and orderly. Flow layers are parallel to each other with no disruption between them in the form of mixing, eddies, or swirls. The Reynolds number is a non-dimensional number used as a criterion for distinguishing laminar from turbulent flow.

$$Re = \frac{\rho UL}{\mu} \tag{24}$$

Where U and L are the characteristic velocity and length scale respectively, μ is the dynamic viscosity, and ρ is the fluid density. The Reynolds number is a ratio of the inertial forces to the viscous forces. Thus, low Reynolds number flows are highly viscous and laminar and high Reynolds number flows are turbulent.

For flow between parallel surfaces, the characteristic dimension is twice the distance between surfaces, and the flow is laminar for Re < 1400. In natural convection in buildings where air velocities are low ($U \approx 10^{-1}$ m/s) and distances are large (L > 1 m), the flow is expected to be transitional or fully turbulent due to the low viscosity of air ($\mu = 1.8 \times 10^{-5}$ kg/ms).

Turbulent flow is characterized by random and chaotic motion in the flow. Furthermore, turbulent flow also can contain rotational flow structures called turbulent eddies. Eddies cause fluid regions separated by great distance to be brought together, allowing heat, mass, and momentum to be transferred very effectively. Essentially, there is a high degree of mixing in turbulent flow.

Turbulent flow is characterized by small random fluctuations in the main velocity field. The velocity u (as well as *v* and *w*) is decomposed into a mean or time averaged component, U and a fluctuating component u'. This is called the Reynolds decomposition,

$$u = U + u' \tag{25}$$

where by definition the time average of u', $\overline{u'}$ is zero.

$$\overline{u'} = \frac{1}{\Delta t}\int_0^{\Delta t} u'(t)dt \equiv 0 \tag{26}$$

The fluctuating component is therefore described by its root mean square and variance. The Reynolds decomposition is applied to all the scalar transport quantities ϕ. Substituting the new expression for velocity into the instantaneous momentum equations (Navier Stokes) yields the time-averaged or Reynolds-averaged Navier Stokes equations (RANS). The turbulent momentum equation in the x-direction is

$$\frac{\partial(\rho U)}{\partial t} + \nabla(\rho U \boldsymbol{U}) = -\frac{\partial P}{\partial x} + \nabla(\mu \Delta U) - \left[\frac{\partial\left(-\rho\overline{u'^2}\right)}{\partial x} + \frac{\partial(\rho\overline{u'v'})}{\partial y} + \frac{\partial(\rho\overline{u'w'})}{\partial z}\right] + S_{Mx} \tag{27}$$

The extra terms turbulent terms $-\rho\overline{u'^2}$, $\rho\overline{u'v'}$, $\rho\overline{u'w'}$ are called the Reynolds stresses. The density and pressure also fluctuate due to turbulence so P and ρ in the RANS equation are actually time averaged variables. The scalar transport equation for turbulent flow is

$$\frac{\partial(\rho\phi)}{\partial t} + \nabla(\rho\phi \boldsymbol{U}) = \nabla\left(\Gamma_\phi \Delta U\right) - \left[\frac{\partial\left(-\rho\overline{\phi'u'}\right)}{\partial x} + \frac{\partial\left(\rho\overline{\phi'v'}\right)}{\partial y} + \frac{\partial\left(\rho\overline{\phi'w'}\right)}{\partial z}\right] + S_\phi \tag{28}$$

Where Γ_ϕ is the diffusion coefficient for ϕ.

The mean flow is computed using Favre averaging in most commercial CFD software packages.

3.3.4 Turbulence Models

The choice of a turbulence model is highly dependent on the application and the computational resources available. The most common and widely applicable models are based on the Reynolds-averaged Navier Stokes (RANS) equations. The RANS equations allow the fluctuations to be time-averaged such that each small high frequency fluctuation is not solved directly. The RANS equations are based on the instantaneous Navier-Stokes equations with added terms to account for the fluctuating components. These extra variables require a turbulence model to solve.

3.3.4.1 Standard k-ϵ model

The standard k-ϵ is the most widely used and verified turbulence model for practical engineering flow simulations. It is a semi-empirical model two equation model, involving transport equations for the turbulence kinetic energy k, and the turbulence dissipation rate ϵ. The model is valid only for fully turbulent flows. The turbulent kinetic energy per unit mass is defined as

$$k = \frac{1}{2}\left(\overline{u'^2} + \overline{v'^2} + \overline{w'^2}\right) \tag{29}$$

Thus the total instantaneous kinetic energy per unit mass in a turbulent flow is

$$k(t) = \frac{1}{2}(U^2 + V^2 + W^2) + \frac{1}{2}\left(\overline{u'^2} + \overline{v'^2} + \overline{w'^2}\right) \tag{30}$$

The transport equation for the turbulent kinetic energy follows the same form as transport equations for energy

$$\frac{\partial(\rho k)}{\partial t} + \nabla(\rho k \boldsymbol{U}) = \nabla\left(\frac{\mu_\tau}{\sigma_k}\Delta\phi\right) + 2\mu_\tau S_{ij}.S_{ij} - \rho\epsilon \tag{31}$$

Where S_{ij} is the rate of fluid deformation and μ_τ is the turbulent viscosity which relates to the turbulent diffusion constant by $\Gamma_t = {}^{\mu_\tau}/_{\sigma_k}$. The last two terms represent the rate of production and dissipation of *k* respectively

$$S_{ij} = \left(\frac{\partial U_i}{\partial x_j} + \frac{\partial U_j}{\partial x_i}\right) \tag{32}$$

The rate of turbulence dissipation per unit mass is

$$\epsilon = 2\frac{\mu}{\rho}\overline{s'_{ij}.s'_{ij}} \tag{33}$$

Where

$$s'_{ij} = \left(\frac{\partial u'_i}{\partial x_j} + \frac{\partial u'_j}{\partial x_i}\right) \tag{34}$$

The terms k and ε are related through the eddy or turbulent viscosity μ_τ

$$\mu_\tau = \rho C_\mu \frac{k^2}{\epsilon} \tag{35}$$

The transport equation for ϵ

$$\frac{\partial(\rho\epsilon)}{\partial t} + \nabla(\rho\epsilon \boldsymbol{U}) = \nabla\left(\frac{\mu_\tau}{\sigma_\epsilon}\Delta\epsilon\right) + \mathrm{C}_{1\mathrm{e}}\frac{\epsilon}{\mathrm{k}}2\mu_\tau S_{ij}.S_{ij} - \mathrm{C}_{2\mathrm{e}}\rho\frac{\epsilon^2}{k} \quad (36)$$

The last two terms represent the rate of production and dissipation of ϵ respectively. The k-ϵ model contains five adjustable constants

$\mathrm{C}_{1\mathrm{e}}$ = 1.44, $\mathrm{C}_{2\mathrm{e}}$ = 1.92, C_μ = 0.09 , σ_k = 1.00, σ_ϵ = 1.30

The Boussinesq hypothesis is used in the k-ϵ and k-ω models to relate the Reynold's stresses to the velocity gradients (rates of deformation) as follows

$$\rho\overline{u'_\iota u'_j} = \mu_\tau\left(\frac{\partial U_i}{\partial x_j} + \frac{\partial U_j}{\partial x_i}\right) - \frac{2}{3}\rho k\delta_{ij} \quad (37)$$

The standard k-ϵ model is known to be poor in modeling flows with large strains (e.g. curved boundary layers, swirling flows), rotating flows. Please refer to the Fluent User Guide and Versteeg et al. (2007) for a full mathematical description of these models.

(Versteeg et al. 2007)

3.3.4.2 RNG k-ϵ model

The RNG k-ϵ model is a modification of the standard k-ϵ model using renormalization group theory. One particular advantage of the RNG k-ϵ model is that it includes a differential formula for effective viscosity that accounts for low-Reynolds-number or viscous effects. However, the effective viscosity option requires that the near wall region be resolved, thus has no advantage for coarse meshes which use the wall function approach. The standard wall function and enhanced wall treatment methods are available in Fluent with the k-ϵ models. (ANSYS Fluent Theory Guide, 2009)

The RNG k-ϵ model requires 10-15% more computational time due to a higher degree of non-linearity and other complexities with the governing equations. (ANSYS Fluent User Guide, 2009)

3.3.4.3 Standard k-ω model

The standard k-ω turbulence model is also a two equation model based on the transport equations for the turbulence kinetic energy k, and the specific dissipation rate ω, representing approximately the ratio of k to ϵ. The transport equation for ω is very similar to the transport equation for ϵ, except with a different form to the rate of production and dissipation terms equations and different constants.

The standard k-ω turbulence model is an empirical model which includes a low Reynolds number correction when a refined grid is used. In Fluent, the k-ω model uses enhanced wall functions as the near wall treatment. The standard k-ω turbulence model is similar in computational time to the standard k-ϵ model.

Both the k-ω model are RNG k-ϵ model with the enhanced wall treatment are capable of modelling coarse meshes, and have low Reynolds number treatments when the near wall region is resolved. Therefore both should be suitable for coarse and fine meshes. (ANSYS Fluent Theory Guide, 2009)

3.3.5 Radiation Models

Air is transparent to infrared radiation and thus does not participate in radiative heat exchange. Therefore only radiation between surfaces will be considered. In general, radiative heat transfer is important in a simulation with the radiative heat flux is large compared to the heat flux due to convection or conduction. Typically this occurs when surface temperatures are high due to the fourth order dependence on temperature. In natural convection radiative heat fluxes are low but comparable in size to convective heat fluxes since buoyancy driven flow has low velocities. Radiation between surfaces in buildings, especially between glazing surfaces and internal surfaces (where there are large temperature differences) is therefore expected to be significant.

The emissive power E (W/m^2) a surface at the absolute temperature T (K) is given by

$$E = \varepsilon\sigma T^4 \tag{38}$$

Where σ is the Stefan-Boltzmann's constant $\sigma = 5.67 \times 10^{-8}$ (W/m^2K^4), and ε is the surface emissivity $\varepsilon < 1$.

The fraction of radiation incident on a surface that is reflected, absorbed, or transmitted is denoted by the reflectance ρ^*, absorptance α^*, and transmittance τ^*respectively, where

$$\alpha^* + \rho^* + \tau^* = 1 \tag{39}$$

In general, the emissivity depends on the wavelength of the radiation. The "gray" assumption is common for practical radiation problems and assumes there is no emissivity dependence on wavelength..

For an opaque surface ($\tau^* = 0$) at constant temperature, the amount of radiation being absorbed and emitted is equal. In this case and if the surface is gray, the absorptivity equals the emissivity.

$$\varepsilon = \alpha^* \tag{40}$$

Fluent offers a selection of radiation models, of which the P1, S2S, and DO will be described.

The optical thickness of the fluid medium can be used to determine which radiation model is suitable for the application. The optical thickness of a fluid medium is defined as

$$optical\ thickness = (a + \sigma_s)L \tag{41}$$

Where a is the absorption coefficient, σ_s is the scattering coefficient, and L is the characteristic length.

For air, the absorption and scattering coefficients are zero however Fluent uses a default absorption coefficient of $0.01m^{-1}$ for a non-participating fluid medium (a participating medium has non-zero absorption and/or scattering coefficients and thus participates in radiation exchange).

Using the cavity width as characteristic length the optical thickness for the convective loop geometry is

$$optical\ thickness = (0.01m^{-1})0.45m = 0.0045 \ll 1$$

(ANSYS Fluent Theory Guide, 2009)

3.3.5.1 P1 Model

The P-1 model assumes gray radiation. It also assumes that all surfaces are diffuse, meaning that incident radiation is reflected equally in all direction (isotropic). The P1 model is among the least computationally expensive radiation models but is not valid for optical thicknesses less than one; only the DTRM and DO models are appropriate. Furthermore, only the DO model can model interior and exterior transparent walls such as glass. Thus only the DO model will be described. (ANSYS Fluent Theory Guide, 2009)

3.3.5.2 DO Model

The governing equation for radiative heat transfer is termed the radiative transfer equation (RTE). The RTE contains integrals of intensity over a spherical geometry. The DO model solves the RTE over a finite number of discrete solid angles. The solution depends on the incident radiation intensity at a surface, which is not initially known. Therefore an iterative approach is necessary where the boundary conditions are continually updated.

In general, no coupling exists between radiation and the flow field since thermal radiation exchange is effectively instantaneous compared to the rate of heat exchange due to conduction or convection. In this case, the energy and radiation equations are solved separately in an iterative fashion. The DO model has an option for coupling radiation and energy, whereby the equations for energy and radiation are solved simultaneously. The coupled method however is not suitable for applications where the optical thickness is less than ten.

The discrete-ordinates (DO) model can be used for the entire range of optical thicknesses. It can solve surface to surface radiation problems as well as those with participating media. For problems with non-participating media, radiation influences the flow field indirectly by changing the boundary conditions at surfaces. The DO model can be

used to model gray and non-gray radiation using a discretized gray band model, essentially dividing the radiation spectrum into N wavelength bands. Each band is then assumed gray.

The radiative transfer equation is discretized in terms of the polar coordinate system shown in Figure 3.1, where the angles θ and ϕ are the polar and azimuthal angles respectively. Each octant of the angular space is discretized into N_θ x N_φ solid angles or control angles. For most practical problems the number, setting the number of θ and ϕ divisions to 2 is sufficient ($N_\theta = 2$, $N_\varphi = 2$). Finer angular discretization is more important for complex geometries and where specular radiation exchange is significant.

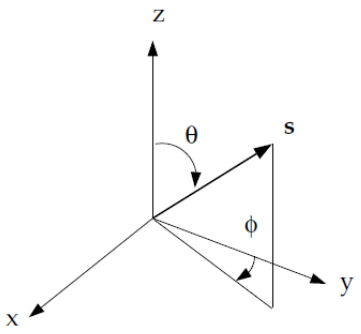

Figure 3.1 - Polar coordinate system for DO model angular discretization (ANSYS 2009)

Each discretized control angle is divided into pixels, with higher pixel resolution representing greater accuracy but also increased computational cost. The default 1 x 1 pixel resolution is sufficiently accurate for most problems.

The most important aspect of the DO model is its ability to model semi-transparent walls (both interior and exterior). Only the DO model has this capability. Radiation flux through a semi-transparent wall is characterized by the absorption or attenuation coefficient a, as opposed to the absorptivity. For an incident radiation intensity I_o (W/m^2), the radiation intensity I, a distance x through a medium is

$$I = I_o e^{-ax} \tag{42}$$

Therefore the absorption coefficient a and transmissivity, τ can be related by

$$a = -\frac{1}{x}\ln\left(\frac{I}{I_o}\right) = -\frac{1}{x}\ln\tau \tag{43}$$

(ANSYS Fluent Theory Guide, 2009)

3.3.5.3 Solar Load Model

Solar ray tracing

ANSYS Fluent provides a solar-load model with a solar ray tracing algorithm to compute solar loads on a domain. It is only available for the 3D solver and can be used for transient simulations. The solar calculator tool determines the solar ray direction vector based on given time of day, date, longitude, and latitude. Direct normal irradiation is computed using the ASHRAE Fair Weather Conditions method. Direct radiation is modelled using a two band spectral model for the visible and IR components. The spectral fraction defines the proportion of visible radiation intensity to the total

$$spectral\ fraction = \frac{V}{V + IR} \tag{44}$$

Diffuse radiation is also accounted for based on a single band model and accounts for radiation reflected off the ground. The solar load model does not model emission from surfaces, thus it should be accompanied by a radiation model (e.g., DO).

The ray tracing algorithm is able to trace out a path through the domain until an opaque surface is reached. It performs a shading analysis to accurately determine which surfaces will be shaded from the incident radiation. Incident radiation on an external opaque surface is completely disregarded; it does not contribute to any heat gain. Incident radiation passing through a semi-transparent wall will be attenuated. The absorptivity and transmissivity of a semi-transparent wall are specified based on the two band model. The heat flux is then calculated at each surface adjacent to the fluid zone. Note that surfaces participating in solar ray tracing can be individually specified. The heat flux is applied through a source term in the energy equation for a computational cell. The heat source can be applied to either a solid cell, conduction cell (for a wall with thickness but not a solid mesh), or an adjacent fluid cell.

The Fluent tutorial "Using Solar Load Model for Indoor Ventilation" (ANSYS Fluent, 2009) recommends applying the solar heat flux directly to the adjacent fluid cell. Applying the heat flux to the wall can lead to an over-predicted wall temperature, especially if the near wall region is not fully resolved with a fine mesh.

Because the solar ray tracing model itself is not a full radiation model, the reflected component of the primary incident radiation on a surface within the domain is simply distributed equally across all surfaces participating in solar ray tracing. In other words, the reflected component is not traced directly to other surfaces. For a domain which is highly glazed, a significant fraction of the reflected component from an internal opaque surface will actually be lost through the glazing and instead of being distributed along the glazing surface. In this case, the scattering fraction, i.e. the fraction of the reflected radiation distributed uniformly among all participating surfaces will be less than the default value of 1.0. This value can be adjusted accordingly.

DO Irradiation

The alternative to the solar load ray tracing model is the DO irradiation model. In this model, the solar load is applied as radiative boundary condition and is used with the DO radiation model. This option is a more realistic approach to modelling solar loading than the solar ray tracing method, however is not available for transient simulations. (ANSYS Fluent Theory Guide, 2009)

3.3.6 Near Wall Treatment

The near wall region is the most critical region for an accurate model. It is the region where the scalar transports such as momentum and energy change most rapidly. In natural convection the near wall is the region where heat transfer occurs, and where buoyant forces drive the flow. Buoyant flow is known to be generally turbulent. Turbulent models can accurately model the mean flow away from the wall where the flow is fully turbulent. In the near wall region however, a different model is required.

The near wall region can be divided into the inner-layer and outer-layer. The inner layer itself contains three important regions, the viscous sublayer, buffer layer, and log-law or turbulent layer. The inner layer makes up 10-20% of the total thickness of the near wall region. The outer layer is free from viscous effects and is modelled with the law of the wake. The following will focus on the inner-layer, refer to Versteeg et al. (2007) for more information regarding the outer layer.

At the surface of the wall, the no-slip condition exists where the flow velocity is zero. Due to this interaction the flow very close to the wall is highly viscous and nearly laminar. This layer is termed the viscous sublayer.

Close to the wall, the flow is influenced by viscous effects and the mean velocity U depends only on the distance from the wall y, the fluid viscosity μ (μ = ρν) and density ρ, and the wall shear stress τ_w. Dimensional analysis provides dimensionless parameters for the velocity u^+ and distance from the wall y^+, where

$$u^+ = \frac{U}{U_\tau} \tag{45}$$

$$y^+ \equiv U_\tau \frac{\rho y}{\mu} \tag{46}$$

where U_τ is the friction velocity, defined as

$$U_\tau = \sqrt{\frac{\tau_w}{\rho}} \tag{47}$$

Figure 3.2 shows a typical treatment of the near wall region with a semi-log plot. The non dimensional velocity U/U_τ in the vertical axis is plotted against the natural logarithm of the non-dimensional distance from the wall, y+ in the horizontal axis.

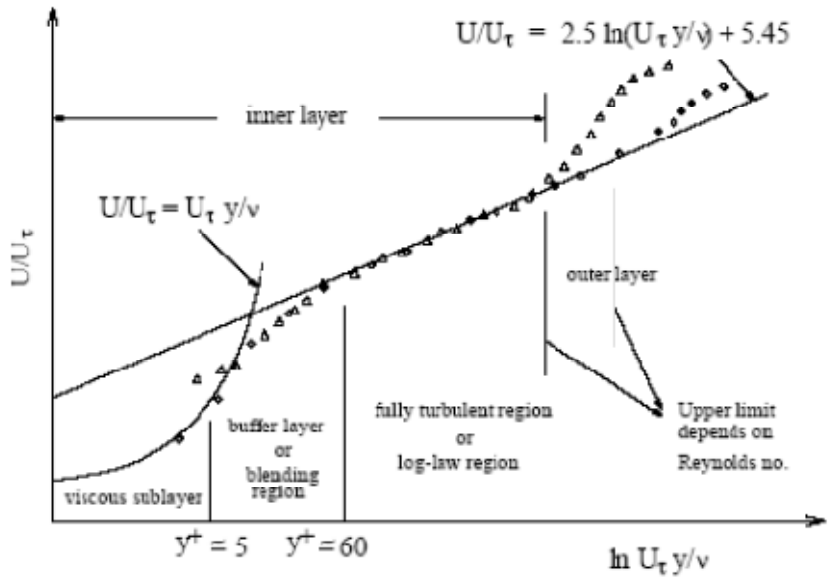

Figure 3.2 - Subdivisions of the Near Wall Region (ANSYS Fluent Theory Guide, 2009)

In the viscous sub-layer, the mean velocity is directly proportional to the shear stress τ_w, from which follows

$$u^+ = y^+ \tag{48}$$

meaning there is a linear relationship between velocity and distance. The viscous (or linear) sub-layer is generally defined by y+ < 5. In the outer-layer, where viscous effects play a less predominant role and the velocity gradient is smaller, there is a logarithmic relationship between the velocity and wall distance

$$u^+ = \frac{1}{\kappa}\ln y^+ + B = \frac{1}{\kappa}\ln Ey^+ \tag{49}$$

where von Karman's constant $\kappa \approx 0.4$, and B ≈ 5.5 (E ≈ 9.8). This layer is termed the log-law layer and is defined by 30 < y+ < 500. The flow is mainly turbulent as it is heavily influenced by the main flow. In between these regions is a buffer layer where viscosity and turbulence both play important roles and must be accounted for. The functions describing the surrounding areas must be blended in some manner.

There are two methods for modelling the near wall region. In the first method the viscosity affected near-wall region is not resolved, and instead emprical wall-functions are used to model the region. However these wall functions may not be accurate for bouyancy driven flows and flows with low Reynolds number effects. The second

method is to you use a two-layer model to resolve the the near wall region completely with a fine mesh. This requires substantially more computational resources.

Wall Function Method

With standard wall functions, the wall adjacent cell should be located in the log-law or fully turbulent region, 30 < y+ < 300, ideally closer to the boundary. Wall functions become less accurate when applied outside this range and in all cases, wall adjacent cells should not be placed in the buffer or transitional region 5 < y+ < 30.

Two-layer Model

The two-layer model is an approach where the whole domain is subdivided into a viscosity affected region and a fully turbulent region. The two-layer approach requires that the near wall region including the viscous sub-layer is resolved with a fine mesh. The viscous sub-layer is considered to be resolved when the wall adjacent cell is at y+ ≈ 1 with an upper limit of y+ < 5. The layers are a divided based on the turbulent Reynolds number, Re_y

$$Re_y \equiv \frac{\rho y \sqrt{k}}{\mu} \tag{50}$$

where the flow is considered fully turbulent for Re_y > 200. It is recommended that at least 10 cells be located in the viscosity affected region of the two layer model. The two layer model is used as part of the enhanced wall treatment in Fluent for the k-ϵ models. If the mesh is sufficiently fine, the two layer model is applied. However, the enhanced wall treatment is also able to handle coarser meshes through a combined two-layer and enhanced wall function approach. Therefore the enhanced wall treatment is suitable for coarse and fine meshes.

Enhanced Wall Functions

The enhanced wall functions provide more flexibility as to what region the wall adjacent cells are located. It applies a single wall function for the entire near wall region (viscous sub-layer, bugger layer, turbulent layer) by blending the linear and logarithmic functions used in the standard wall function formulation. The enhanced wall functions are designed to be accurate for all values of y+ including the buffer region. Enhanced wall functions are used with the k-ω model which can act as a low Reynolds number model (refined grid) or high Reynolds number model (coarse grid). (ANSYS Fluent Theory Guide, 2009)

3.3.7 Boundary Conditions

The thermal boundary conditions at the walls of a closed fluid domain define the energy transfer into and out of the domain. There are five types of thermal boundary conditions available in ANSYS Fluent:

- Fixed heat flux
- Fixed temperature
- Convective heat transfer
- External radiation heat transfer
- Combined external radiation and convective heat transfer

Conduction at the walls can be handled in two ways. First, the solid wall can be meshed allowing the diffusion (conduction) equations to be solved in the solid domain with a thermal boundary condition defined at the external surface of the solid wall. Alternatively, a thin wall can be modelled whereby the wall is modelled as a single surface with a defined thickness. A 1D steady conduction equation is then used to compute the conduction through the wall. Figure 3.3 shows a schematic of a thin wall with specified thickness Δx.

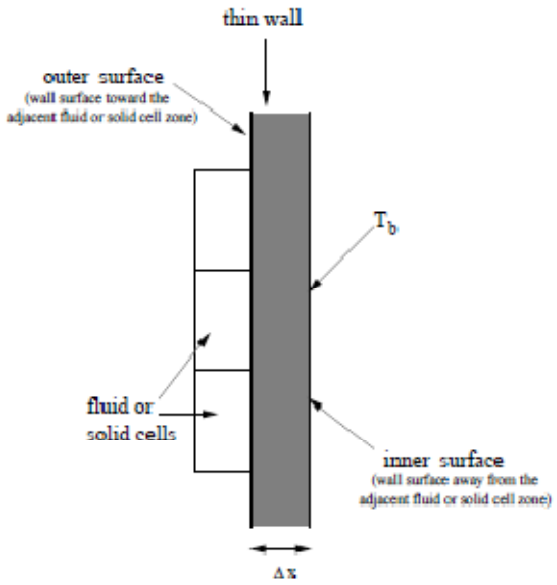

Figure 3.3 - Thin wall model (ANSYS Fluent Theory Guide, 2009)

The thin wall model also has a shell conduction option which computes heat conduction within the wall (along the surface) as well through the wall.

The temperature boundary condition calculates the heat flux based on a fixed wall temperature

$$Q_w = h_f(T_w - T_f) + Q_{rad} \tag{51}$$

Where h_f is the local heat transfer coefficient at the fluid and wall boundary, T_w is the wall temperature, T_f is the fluid temperature near the wall, and Q_{rad} is the radiative heat flux on the internal side of the wall. The local heat

transfer coefficient h_f is calculated by ANSYS Fluent based on the flow conditions (turbulence, velocity, temperature) at the near wall.

The heat flux boundary condition takes the exact form of the temperature boundary condition equation, except that the total flux Q_w is specified to calculate the wall temperature T_w.

The convective heat transfer boundary condition calculates the wall heat flux based on the external heat transfer coefficient, h_{ext}

$$Q_w = h_{ext}(T_{ext} - T_w) = h_f(T_w - T_f) + Q_{rad} \quad (52)$$

In practical terms, this means the external heat transfer coefficient is really the effective heat transfer coefficient accounting for both convection and radiation.

The external radiation boundary condition determines the heat flux based on the external wall emissivity ε_{ext} and the temperature of the surroundings T_{surr}, representing a radiation sink or source.

$$Q_w = \varepsilon_{ext}\sigma(T_{surr}^4 - T_w^4) = h_f(T_w - T_f) + Q_{rad} \quad (53)$$

Where σ = 5.67 x 10-8 W/m^{2}K^4 is the Stefan-Boltzmann constant.

The combined external radiation and convective heat transfer boundary condition is simply the combination of the convective and radiative boundary conditions.

$$Q_w = h_{ext}(T_{ext} - T_w) + \varepsilon_{ext}\sigma(T_{surr}^4 - T_w^4) = h_f(T_w - T_f) + Q_{rad} \quad (54)$$

In this case, the external heat transfer coefficient h_{ext} accounts for convection only since radiation is explicitly determined. (ANSYS Fluent Theory Guide, 2009)

3.4 Solver Methods

3.4.1 Pressure Velocity Coupling

Solvers employed by CFD software must compute the entire fluid field based on the governing equation for continuity, momentum, energy, and other scalar transport variable. The governing equation for energy is dependent on the velocity field, and in general the convection of a scalar variable depends highly on the local velocity field. The velocity field however is not initially known, but is solved for along with other flow variable as the iterative solution progresses.

The momentum and continuity equations are highly linked to each other through the velocity field. Furthermore, the momentum equations are linked by the pressure field, which also must also be solved for. This pressure-velocity coupling forms the basis for the solution algorithms used in CFD software.

There are two general numerical methods used in ANSYS Fluent; the pressure-based solver and the density based solver. In both methods, the velocity field is determined from the momentum equations, while the pressure field is determined in completely different ways.

The density based solver is a coupled solver, meaning the governing equations for continuity, momentum and energy etc. are solved simultaneously. The density field is determined with the continuity equation and then the pressure field is determined using the equation of state. Thus the density based solver is really intended for compressible flows, where the fluid density is not constant and rather a function of pressure. For more information on the density based solver refer to the ANSYS Fluent Theory Guide, 2009.

The pressure based solver uses an iterative solution where the governing equations are solved sequentially and separately from each other. The pressure field is determined based on a pressure correction equation derived from the continuity and momentum equations. The pressure based method was originally developed for low speed incompressible flows, but has been modified and extended to work for a wide range of flow conditions. (Versteeg et al., 2007)

3.4.1.1 SIMPLE algorithm

The SIMPLE or Semi-Implicit Method for Pressure Linked Equations algorithm is an iterative algorithm based on calculating the pressure field in a grid using a guess and correct method. The process is initiated with a guess at the pressure field p*. A correction term p' is defined such that

$$p = p^* + \alpha_p p' \tag{55}$$

where p is the correct pressure field and α_p is the under-relaxation factor for pressure. Similarly, guess and correction terms are defined for the velocity field e.g. $u = u^* + \alpha_u u'$. The discretized momentum equations are solved using *p** to determine the velocites *u*, v*, and w**. These velocities are then used to solve for p'. The pressure correction term is then used to correct the pressure and velocities. Using these new values, scalar quantities ϕ such as temperature and kinetic energy are solved for based on an initial guess ϕ'. These steps yield new values for *p, u, v, w,* and ϕ*,* which are then used as guesses for the next iteration.

The correction terms can lead to divergence in the solution without proper under-relaxation. An under-relaxation factor α of 0 leads to no correction at all while a value of 0 indicates maximum correction. Thus the under-relaxation value must fall between 0 and 1 and be carefully chosen. If α is too low, the solution may converge very slowly or not at all. However, if α is too high, the solution may oscillate or even diverge. Separate under-relaxation

factors are defined for pressure, momentum, energy, density, turbulent kinetic energy and other scalars depending on the model. The SIMPLE algorithm is shown schematically in Figure 3.4

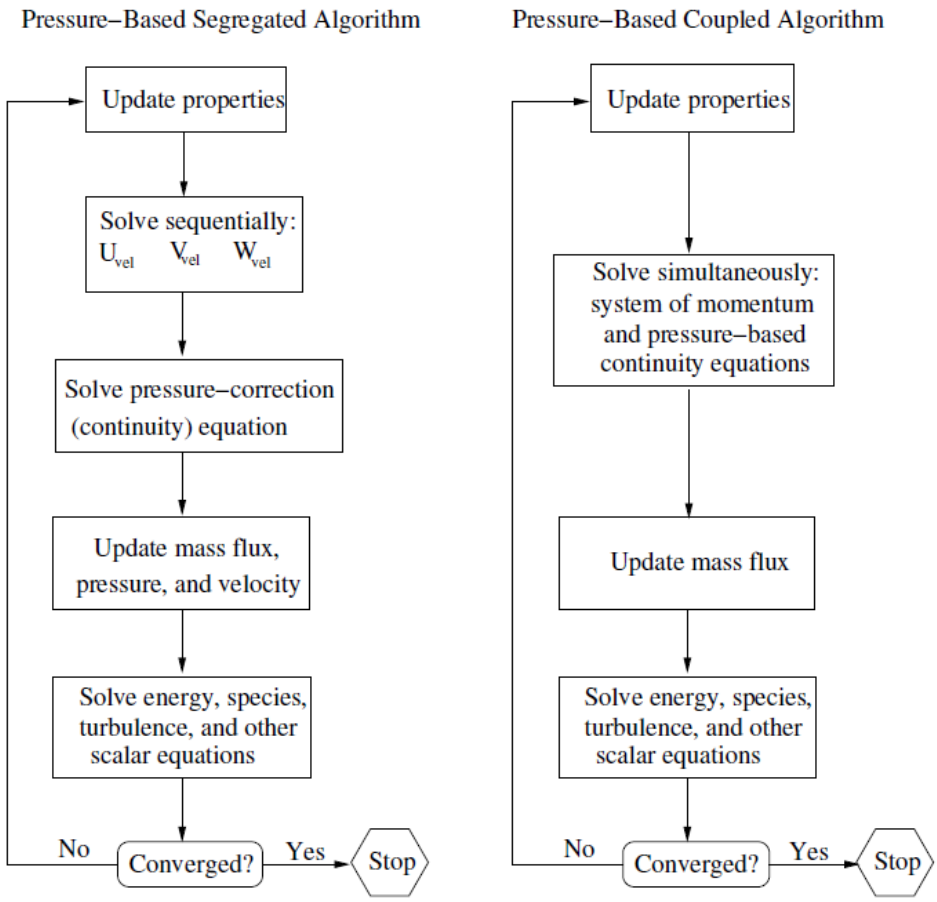

Figure 3.4 - Pressure-based Segregated and Coupled Algorithm Structure ((ANSYS Fluent Theory Guide, 2009)

3.4.1.2 SIMPLEC algorithm

The SIMPLEC algorithm is a modification of the SIMPLE algorithm which has not been definitively shown to be more accurate or achieve faster convergence.

3.4.1.3 PISO algorithm

The PISO algorithm or Pressure Implicit with Splitting of Operators is part of the family of SIMPLE with the main difference being an extra correction step in the algorithm. For steady-state problems, the PISO algorithm does not proved any significant advantage over SIMPLE or SIMPLEC when the under-relaxation factors are chosen properly. For transient problems, the PISO algorithm can reach convergence with a far lower number of iterations. Thus the PISO algorithm is suitable for transient problems especially with large time steps.

3.4.1.4 Coupled algorithm

The coupled algorithm is fundamentally different from the segregated SIMPLE, SIMPLEC, and PISO algorithms in that it solves the momentum and pressure based continuity equation simultaneously or in a coupled fashion. As a result of the coupling, convergence is reached much faster than with the segregated algorithm but requires 1.5-2 times more memory during the solution process. The coupled algorithm is also suitable for transient calculation in particular when the time steps are large and a coarse mesh is used.

3.4.2 Discretization

3.4.2.1 Spacial Discretization

Scalar transport quantities such as temperature, energy, turbulent kinetic energy, etc. are determined at each node of a cell in a discretized space or grid. The solution at the node of each cell is calculated by interpolation based on solving the flow equations at each face of the cell. The discretization scheme determines the interpolation function used which can be linear or higher order.

Discretization schemes must possess fundamental properties to ensure it is physically realistic; these are conservatism, boundedness, and transportiveness. Conservatism means the convective and diffusive fluxes of a general transported property ϕ out of one face a cell equal those into the next face of the adjacent cell. Boundedness and transportiveness must also be satisfied. Boundedness means the solution at a node is bounded by the values at each of its boundary faces. Transportiveness means that the transport of a property due to convection relative to diffusion is properly accounted for.

In ANSYS Fluent, the First Order Upwind, Second Order Upwind, Power Law, QUICK, and Third Order MUSCL spacial discretization schemes are available. Selecting the appropriate discretization scheme is especially important when meshes are coarser and thus larger gradients exist through the control-volume cells.

The upwind differencing scheme is one of the simplest and most common discretization schemes. It is more stable and achieves better convergence than higher order methods. However, when the flow is not aligned with the grid lines of the mesh, it can be inaccurate. This false diffusion in the transport values has been shown to be large enough to give non-physical results. Thus for triangular/tetrahedral meshes, where the flow is never aligned parallel to the mesh, second-order upwind differencing will provide more accurate results.

The QUICK scheme (quadratic upstream interpolation for convective kinetics) uses a quadratic interpolation between cell nodes and faces. The QUICK scheme minimizes false diffusion but is less computationally stable and more computationally expensive. The QUICK scheme may be more accurate for rotating or swirling flow. Other higher order methods such as the Power Law and Third Order MUSCL scheme are also available in ANSYS Fluent, however in general the second order upwind differencing scheme will achieve similar accuracy.

3.4.2.2 Pressure Interpolation

ANSYS Fluent offers five discretization methods for pressure. These are the standard, PRESTO!, linear, second order, and body force weighted schemes. The PRESTO! scheme is recommended for high speed rotating or swirling flows and high Rayleigh number natural convection. The body force weighted scheme is suitable for flows with strong buoyancy contributions or other body forces.

3.4.2.3 Gradient Evaluation

Calculation of the gradient of a scalar $\nabla\varphi$ at the cell faces of a control volume is necessary for determing the convection and diffusion terms in the governing flow equations. Gradients can be determined based on values of φ at the cell face or node. Node-based gradient methods such as the Green-Gauss Node Based gradient evaluation are more accurate than cell-based methods when the mesh is irregular or unstructured. Node-based gradient methods are more computationally expensive then cell based methods.

3.4.2.4 Transient Simulation

In steady state simulations, the time-dependent terms in the governing equations drop out to zero. In transient simulations, the governing equations are discretized in both space and time. The spacial discretization is identical to the steady state case. Temporal discretization, i.e. time based, involves integrating the governing equations over a time step Δt.

In general, a scalar property $\varphi(t)$ can used to evaluate the property $\varphi(t + \Delta t)$ using first order temporal discretization. In second order temporal discretization, $\varphi(t)$and $\varphi(t - \Delta t)$ are used to evaluate the property at the next time step.

There are two methods for integrating over time, the implicit and explicit time integration methods. In the explicit method the unknown value in each cell $\varphi(t + \Delta t)$ is determined based on its existing value at the previous time step $\varphi(t)$ and on existing values in neighbouring cells. For first order discretization, this is given by

$$\varphi(t + \Delta t) = \varphi(t) + \Delta t \frac{\partial \varphi(t)}{\partial t} \tag{56}$$

In the explicit method, the unknown value depends only on known values, thus the unknown values in each can be solved sequentially. Due to the nature of explicit discretization, a strict upper limit is set for the time step size. This is a major limitation of the explicit scheme and thus is not recommended for general transient problems. The explicit method is generally only used for specialized problems such as those involving shocks and is only available with the density based solver.

In the implicit method, the unknown value in each cell $\varphi(t + \Delta t)$ is determined based on its existing value at the previous time step $\varphi(t)$ and unknown values in neighboring cells.

$$\varphi(t + \Delta t) = \varphi(t) + \Delta t \frac{\partial \varphi(t + \Delta t)}{\partial t} \quad (57)$$

Because both sides of the equation have unknown values at the future time step $t + \Delta t$, a system of equations is set up to solve the entire domain simultaneously at each given time step. The implicit scheme is unconditionally stable for any time step size, however small times steps are necessary for accurate results. The first order implicit scheme is sufficiently accurate for most problems.

The most general method for solving transient problems uses the iterative time advancement scheme. At each time step, the solver is run for multiple iterations until the convergence criteria is met; the problem is then advanced to the next time step and the solution solved for again. In ANSYS Fluent, the time step should be chosen such that the number of iterations per time step is between 5 and 10. Increasing the time step requires more iterations per time step while decreasing the time step requires less. An appropriate time step size results in the Courant number not exceeding a value of 20-40 in the most transient portions of the domain.

(ANSYS Fluent Theory Guide, 2009)

4 Literature Review

4.1 Turbulence and Radiation Model Comparison

4.1.1 Closed Air Cavities

Buoyant flow (natural convection) is an important phenomenon in displacement ventilation and other aspects of HVAC in building design. Gan (1998) examined the appropriateness of the standard k-ϵ and RNG k-ϵ for modelling turbulent buoyant flow in enclosed air cavities. These flows in general have low Reynold's number influences due to low air velocities especially in the near wall regions. The standard k-ϵ is in general limited to fully turbulent flows far away from walls where shear stress is low and turbulent viscosity is isotropic, thus an accurate low-Re number k-ϵ turbulence model is necessary.

The author validated the standard and RNG k-ϵ model using benchmark experimental results for turbulent natural convection in a narrow tall cavity with one vertical wall maintained at high temperature and the other at a cold temperature (with the top and bottom walls insulated). The SIMPLE algorithm was employed with standard wall functions.

Figure 4.1 shows the velocity profile at the mid-height of the cavity for the standard k-ϵ, RNG k-ϵ, and measured values from the benchmark experiment (determined using laser-Doppler anemometry). The RNG k-ϵ model matches the experimental results much more closely than the standard k-ϵ model. The RNG k-ϵ model also predicts the temperature profiles and Nusselt numbers at the cold and hot walls more accurately.

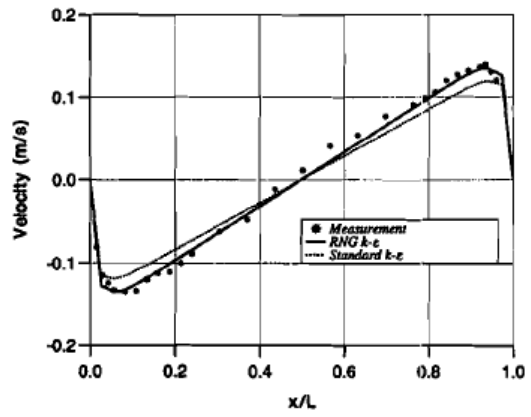

Figure 4.1 – Measured and simulated air velocity profiles in a tall cavity (Gan, 1998)

The author also compared simulation and experimental results using turbulent natural convection wall functions and found these functions are less accurate than the standard wall functions and thus have limited applicability. The reason for the natural convection wall function's lack of accuracy may be due to interfering boundary layers in the thin air cavity.

The author performed a parametric analysis on the variable turbulence parameters to determine which are most responsible for the RNG k-ϵ model's better performance. It was found that the inclusion of the rate of strain term in the ε equation is the main reason for the improved accuracy. Also using the effective viscosity in the diffusion terms as opposed to the turbulent viscosity is suggested as the flow is not entirely turbulent in all regions.

Walsh and Leong (2004) developed a benchmark problem for a comparison of the standard k-ϵ model, RNG k-ϵ model, and Reynold's Stress Model (RSM) for turbulent natural convection in a closed cavity. Numerical solutions are validated and experimental results. The 3D model expands on previous 2D models and uses linear temperature gradients between the hot and cold cavity walls as opposed to the less realistic adiabatic condition. Studies have shown that the effects of heat transfer are not significant until Rayleigh number is sufficiently high, i.e. $Ra > 10^6$, thus the pressure and temperature were adjusted such that $Ra > 10^7$.

The author deemed the two-layer zonal model most appropriate for the near wall treatment as the boundary layer assumptions used for the standard and non-equilibrium wall functions may not be justifiable. Trial modelling also showed the two-layer model having faster convergence rates.

In this model, the boundary layer is separated into two zones: a viscous sub-layer near the walls and a fully turbulent region further away. The turbulent region is treated with the selected turbulence model. The sub-layer must be resolved (i.e. meshed) to accurately determine the flow field parameters. Therefore, the grid off-wall spacing and expansion rate ER are critical to the accuracy of the model. Changes in the off-wall spacing were found to have a much great influence on the Nusselt number accuracy than the expansion rate. This is somewhat expected as the two-layer model has the requirement that y+ equal approximately 1.

The author's found the accuracy of the standard k-ϵ and RNG k-ϵ models to be similar for lower turbulence levels while the RSM was generally poorer. For higher turbulence production the RNG k-ϵ model outperformed the standard k-ϵ model. The angle or tilt of the cavity was also varied and in general the RSM was less accurate and was thus deemed not appropriate for closed cavity natural convection problems. Overall, the standard k-ϵ model had the best performance especially when accounting for the demand on computing resources. Mesh refinement did not yield significant benefits to the accuracy of the model.

4.1.2 Solar Chimneys

Gan (2006) used a validated CFD model to simulate buoyant flow in a solar chimney and double facade. The CFD model was validated using experimental results for a 2.4m double facade (Sandberg and Moshfegh) heated on one side. The Grashof number varied from 8.92×10^{10} and 2.86×10^{10} and was thus significantly high enough to suggest turbulent flow, although it was expected that there would low Re number flows near the unheated wall. The RNG k-ϵ is generally considered more accurate than the standard k- ε for buoyant flow and was thus use to validate the results obtained with the standard k-ϵ model. The mean velocity in the channel was used as the validation parameter with the heat flux as the varying parameter. It was found that with grid refinement, the RNG k-ϵ model

produced similar results to the standard k-ϵ model. As both models were in agreement with experimental data, it was concluded that the standard k-ϵ model would be used to study the solar chimney and double facade as it requires less computing time to achieve grid independent solutions.

A solar chimney consists of a storage wall and glazing between which air flows usually for the purpose of ventilation. The three main solar chimney types are shown in Figure 4.2, each with different inlet configurations. The solar chimney used in the simulation was 6m high with a cavity width varying from 0.2-0.8m. The storage wall was fixed at heat fluxes of 100W/m^2 and 300W/m^2. As the cavity width increased, the mean velocity and exit temperature decreased correspondingly. However, for cavities wider than 0.55m there was a downward/reverse flow which occurs along the unheated wall near the top of the chimney as shown by the velocity vector plot in Figure 4.4. This resulted in a maximum volumetric flow rate occurring for a chimney width of 0.55m, as shown in Figure 4.3.

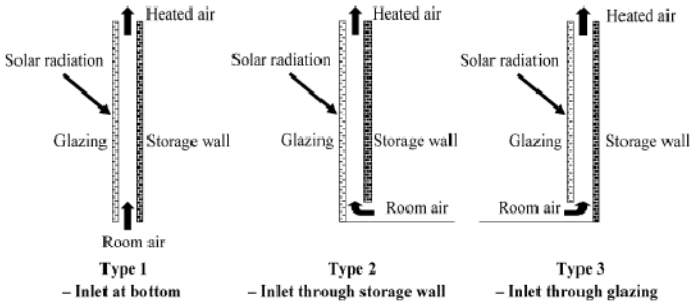

Figure 4.2 - Solar chimney flow configurations (Gan, 2006)

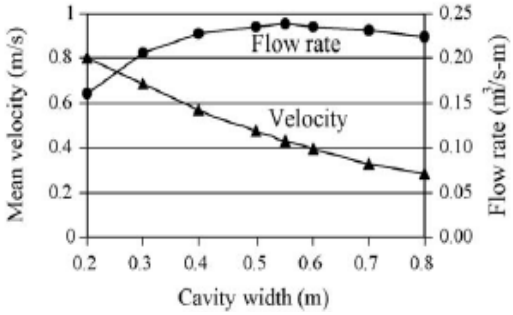

Figure 4.3 -Mean flow characteristics for varying cavity widths (Gan, 2006)

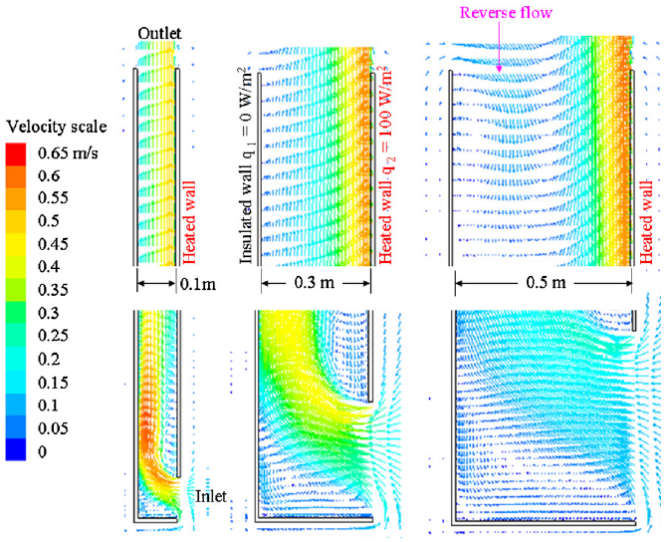

Figure 4.4 - Solar chimney velocity vector plot for three cavity widths (Gan, 2006)

The optimal cavity width, i.e. where the flow rate is maximized, increased with the total chimney height since in general the velocity boundary also increases with height. It was postulated a large heat loss through the glazing would reduce the buoyancy effect leading to downward flow near the glazing occurring at a smaller cavity width.

The author also simulated air flow in a double glazed facade and a hybrid double glazed facade with the outer glazing integrated with photovoltaics. In this case the heat gains on each facade were estimated using a heat balance for constant solar irradiation. The flow rate levelled off for cavity widths above approximately 0.8m. There was no flow reversal likely due to the fact that heat was distributed to both surfaces through solar transmission and heat exchange.

In an extension to the paper by Gan (2006), Gan (2009) presents results of CFD simulation for buoyant air flow in an open cavity of a double facade with different heat fluxes and heat distribution ratios on the two walls. For a typical cavity 3m tall and 0.3m wide with a symmetrical heat flux of 100W/m^2 on both walls, the Ra ≈ 6 x 10^7 suggesting the overall flow is turbulent. The RNG k-ϵ model was used to also account for less turbulent flow. The model was validated against a bench-mark experiment.

Figure 4.5 shows the air flow rate in a 3m tall cavity as a function of cavity width and heat distribution ratio varying from 0% (heat flux one wall only) to 50% (heat flux distributed equally on both walls). The air flow rate was maximized for a heat distribution ratio of 50%. The flow rate increased with cavity width up to 0.6m with diminishing returns. The variation in the flow rate was most pronounced with heat distribution ratios between 0% and 10%. For wider cavities, this is a result of reverse flow; thus the heat flux on either wall should be at least 10% of the total heat flux to maximize air flow.

Figure 4.6 shows the Nusselt number as a function of heat distribution ratio and cavity width. Heat transfer from the walls is highest for larger cavity widths, and when the heat flux is concentrated on one of the vertical cavity walls since temperature differences are highest in this scenario. However, the Nusselt number is relatively constant above a heat distribution ratio of 10%.

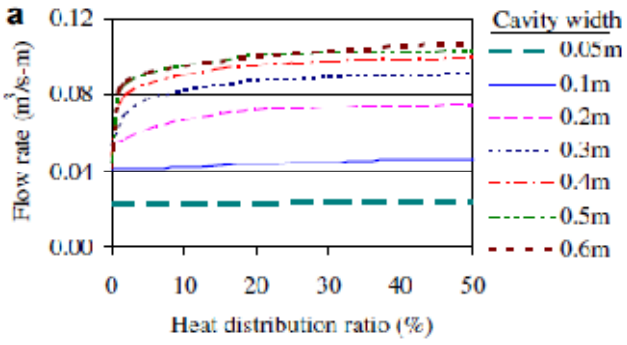

Figure 4.5 - Flow rate for varying heat distribution ratios (Gan, 2009)

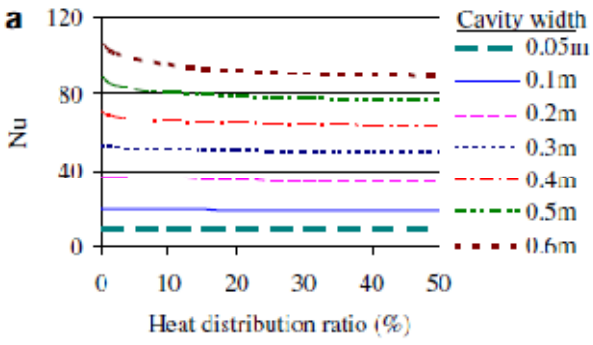

Figure 4.6 - Nusselt number for varying heat distribution ratios (Gan, 2009)

4.1.3 Double-glazed facade

The use of double-glazed (double skin) facades has trended upwards in recent years especially in office buildings as they have the potential for large energy savings especially in the heating season. Some studies have shown that natural convection is effective enough in extracting solar heat gain and that the amount of energy saved by using fans is negligible due to installation and maintenance costs.

Couissirat et al. (2008) modelled three different radiation models (DTRM, DO, P1) and five turbulence models (Spalart-Allmaras, standard k-ϵ, RNG k-ϵ, Realizable k-ϵ, standard k-ω, SST k-ω) against a well documented experimental study for validation and calibration.

The author estimated the order of magnitude of relevant dimensionless parameters using experimental data and empirical correlations. For solid surfaces the radiative Biot number is much greater than the standard Biot number indicating that radiation exchange dominates conduction and convection in the double-glazed facade. Based on the dimensional analysis the authors reiterated that a turbulence model capable of accounting for low Reynolds number effects is required since a laminar and turbulent model cannot both be applied. To account for the non-isotropic nature in the near wall region, the two-layer modelling approach was used for the k-ϵ family of models and enhanced wall functions were used for the Spalart-Allmaras and k-ω family of models. The 2nd order upwind discretization scheme was selected and the PISO pressure-velocity coupling scheme was selected for its suitability to buoyant flows. Convective boundary conditions were imposed with heat transfer coefficients of 12W/m^{2}K and 8W/m^{2}K for the outside and inside walls respectively. A comparison of the average exit temperature in the double facade over a 24h period for the 3 radiation models showed the P1 model having the best fit to the experimental data.

Using the P1 model, a comparison of the turbulence models showed the standard k-ϵ and RNG k-ϵ to have the best fit to experimental data. The number of meshing cells was also varied for each model, with each one showing monotonic convergence (i.e. reduction in error for increasing number of cells) except for the Realizable k-ϵ model. Again the standard k-ϵ and RNG k-ϵ models had the lowest error relative to the experimental results across the varied spectrum of meshing size.

4.1.4 Atria

Rundle et al. (2011) performed a systematic validation of commercial CFD code against experimental data for an atrium geometry with a heated floor surface as shown in Figure 4.7. The standard k-ϵ, standard k-ω, and SST k-ω turbulence models were considered, with the standard k-ω producing the most accurate predictions. The comparisons were done based on the Nusselt number at the wall and the velocity profile across the domain as shown in Figure 4.8.

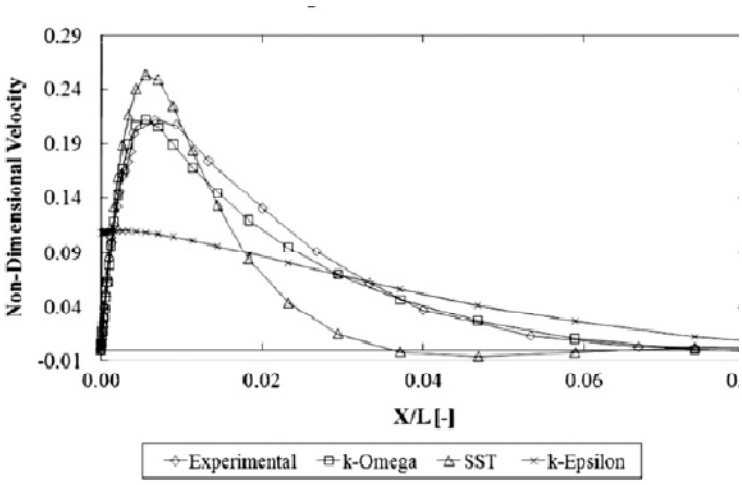

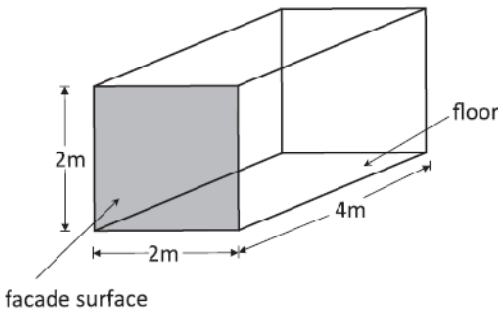

Figure 4.7 - Non-dimensional velocity profile from turbulence models and experiment (Rundle, 2011)

Figure 4.8 - Atrium geometry (Rundle, 2011)

The low Reynolds number near wall approach employed by the standard k-ω model allowed for the higher level of accuracy. The Discrete Transfer radiation model was found to produce more consistent results at a lower computational cost than the Monte Carlo radiation model. The authors concluded that CFD simulations are able to accurately capture the important feature in an atrium including temperature stratification and the link between temperature and velocity present in buoyant fluid flow.

4.1.5 Conclusions and Recommendations

In CFD studies dominated by buoyant flow, the most commonly used turbulence models are the standard k-ϵ and RNG k-ϵ as both provide sufficient accuracy with reasonable computational expense. Generally, both models yielded similar results when compared against benchmark experimental results, as was the case for Coussirat et al. 2008. In some cases (Gan 1998, Gan 2009), the RNG k-ϵ model was deemed most accurate because of its capability to account for low Re number flows. Walsh et al. (2003) and Gan (2005) chose to use the standard k-ϵ model simply because of a reduced computational time over the equally accurate RNG k-ϵ model. Rundle et al. (2011) found the standard k-ω to be superior to the standard k-ϵ model in accuracy. Thus, it is likely the RNG k-ϵ or standard k-ω model would be most suitable to simulate the convective air loop for the NTED™ house, however model comparisons would be advisable and informative.

The optimal cavity width in the solar chimney was shown to be 0.55m (Gan, 2005), greater than which flow reversal occurs. Also, the flow rate is maximized when there is an equal heat flux on each of the two walls forming the channel/cavity.

5 Methodology

5.1 Simplified Building Model

5.1.1 Geometry

Two building geometries were created for CFD simulations. ANSYS ICEM CFD was used to create the geometry and mesh to be exported to ANSYS Fluent. The first geometry, termed the "Basic" geometry, is a highly simplified uniform building model used to analyze the basic characteristics and functionality of the convective loop.

A second geometry more representative of the NTED™ house at 31 Sussex Ave, Toronto, ON is aptly termed the "31 Sussex" geometry. A 3D geometry was necessary to run the solar load model in ANSYS Fluent.

5.1.1.1 Basic Geometry

A simplified geometry with a relatively small (uninhabitable) perimeter space was chosen to represent the house. This was done mainly to simplify the flow regime to better understand the phenomena involved. The Basic geometry design was chosen to have a small scale idealized form whereby the CFD model could be verified through model comparison and grid independence studies.

As described in Hastings et al. (2000), most models and built examples of double envelope houses avoid the use of large sunspaces, and in the case of wall-integrated solar air collector systems, a thin cavity/perimeter space is used. Furthermore, studies on solar chimneys by Gan et al. (2005) indicate the optimal cavity width to be approximately 0.5m. The Basic geometry reflects these considerations.

The simplified house model for the Basic geometry is shown in Figure 5.1 where the x-coordinate represents due north. The core space height dimension is representative of a 10ft ceiling. For uniformity purposes, the south facade was glazed across its entire width and full height of the core. A 0.45m wide cavity separates the internal envelope from the external envelope. The building footprint was chosen to be small to limit the computational resources needed for simulations. Note the east and west walls of the core space are left open as these surfaces have a negligible effect on the cavity air loop. The analysis focuses on the perimeters space; the core space was not meshed.

5.1.1.2 31 Sussex Geometry

The 31 Sussex geometry, shown in Figure 5.2, was created to represent the geometry of the house at 31 Sussex Avenue, Toronto, ON, Canada. Please refer to the section 9.2 in the Appendices for a complete set of drawings for the 31 Sussex Avenue house. The model is a simplified version ignoring internal partition walls and floors. Although this is a major simplification, it was assumed prudent to begin with a highly simplified model and add complexities to subsequent models in a systematic fashion. A model based on a real building geometry was beyond the scope of this work

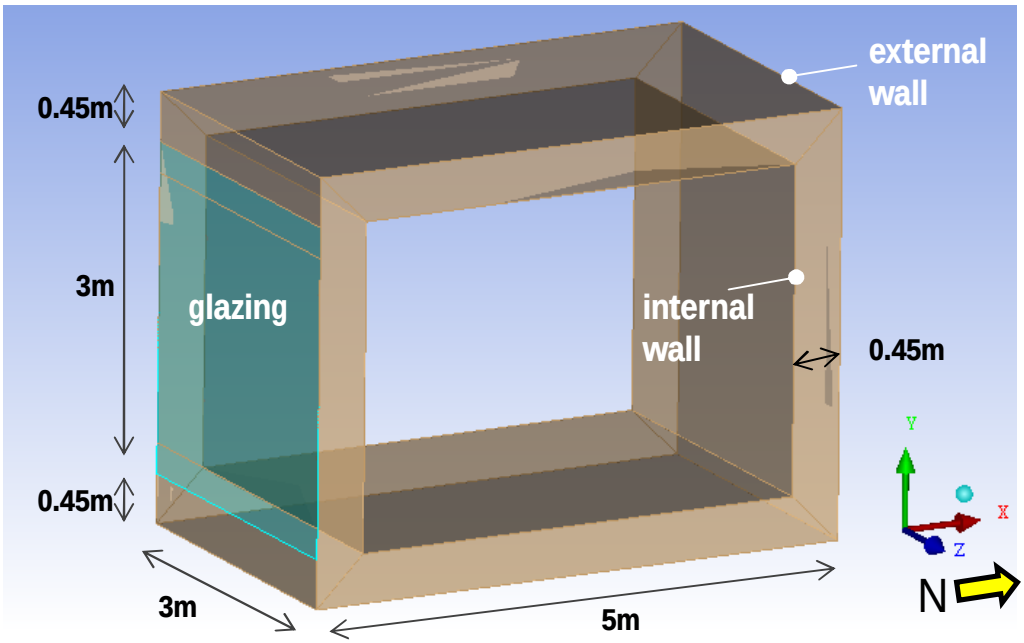

Figure 5.1 - Basic geometry

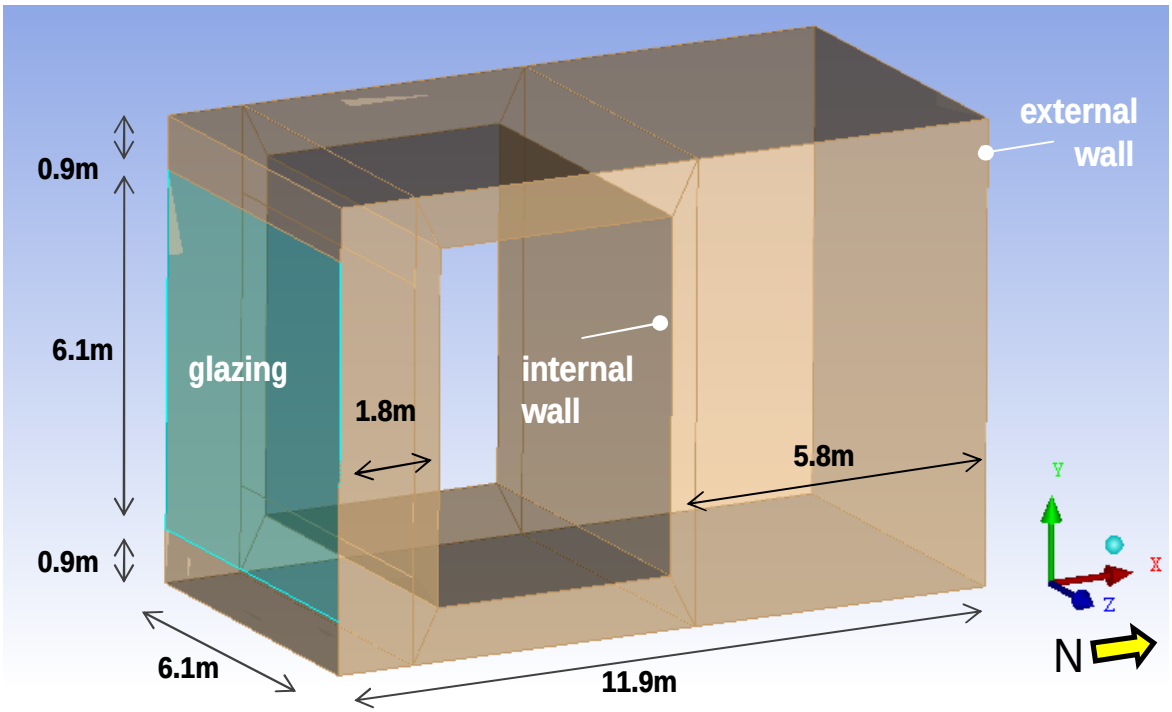

Figure 5.2 - 31 Sussex geometry

5.1.2 Envelope Construction

Identical envelope constructions were applied to both the Basic and 31 Sussex models. All envelopes were modelled as infinitely thin surfaces, i.e. the envelope was not solid meshed. Because the focus of the simulations was the fluid domain and not the solid surfaces, this is a reasonable approximation. Material properties were set to represent an envelope with real thickness. ANSYS Fluent uses these properties in its computations. A common double glazed low emissivity (ε) window with a high solar heat gain coefficient (SHGC) was chosen for the south glazing as shown in Table 5.1.

Table 5.1 - Fenestration properties

	U-Value (W/m^2K)	τ visible	τ IR	α visible	α IR	SHGC
Double glazed low- ε clear	1.99	0.76	0.59	0.10	0.25	0.7

*values estimated based on ε=0.2, 3mm glass, 12.7mm airspace (ASHRAE Fundamentals, 2009)

A typical wall composition was used to set material properties for the wall surface as follows:

- 0.1m by brick (ρ=1800 kg/m^3, c_p=900 J/kgK)
- 0.15m polyurethane foam (ρ=30 kg/m^3, c_p=1500 J/kgK)

(The Engineering Toolbox, 2011)

Since the wall is modelled as a single uniform surface, weighted average values for density and heat capacity were used. The volume weighted wall density is

$$\rho_w = 0.4(1800\ kg/m^3) + 0.6(30\ kg/m^3) = 738\ kg/m^3$$

The mass weighted wall heat capacity is

$$c_p \approx 900\ J/kgK$$

since the polyurethane foam mass is negligible relative to the brick.

To more accurately represent realistic temperatures in the space, the wall conductivity was based on the R-2000 insulation levels for the wall with 20% glazing to wall ratio. Note that the glazing was not accounted for in the wall heat capacity or density approximations. From OBC 2006, the wall U-value is 0.3 W/m^2K (3.34 RSI or R-19) (Dixon et. al 2010). Accounting for the glazing with a U-value of 2 W/m^2K, the net U-value for the wall is therefore

$$U_{wall} = 0.80*0.3\ W/m^2K + 0.20*2\ W/m^2K = 0.64\ W/m^2K\ (R\text{-}9)$$

Table 5.2 summarizes the wall properties used in the simulation

Table 5.2 - Wall properties

	Thickness (m)	U-Value (W/m^2K)	Density (kg/m^3)	Heat Capacity (J/kgK)	Emissivity
Uniform wall	0.15	0.64	740	900	0.9

*wall actually set to 0.15m in ANSYS Fluent despite the intention of setting it to 0.25m

5.1.3 Mesh

A coarse mesh was chosen such that 30 < y+ < 300. Since the y+ parameter is solution dependent, a trial and error process was used until the desired mesh size was achieved. Tetrahedral meshing using the Robust (Octree) method was applied to the geometry. Please refer to ANSYS ICEM CFD User Manual for more information on mesh generation. Multiple layers of rectangular prism cells were applied at all boundary surfaces. The rectangular prism cell shape is ideally suited to flat surface and facilitates uniform refinement in the near wall region.

Two progressively more refined meshes were used for the simulations. As will be shown later, the refined mesh was sufficiently fine for grid independence. Table 5.3 summarizes the three meshes used for the basic geometry and the number and type of cells used to form them.

Table 5.3 - Basic geometry mesh properties

Mesh Density	Total cells	Prism cells	Tetrahedral cells
Coarse	46452	16292	30160
Medium	110922	81460	29460
Refined	135062	97752	37310

Figure 5.3 shows a cross section of the Basic geometry coarse mesh in the north-south plane. A double layer of rectangular prism cells is clearly identifiable along the boundary surfaces. Figure 5.4 shows a close up of the mesh section for the more refined mesh. An expanding prism mesh is found along each boundary surface. The mesh is finest near the wall, with the height of the prism increasing by a factor of 1.2 for each subsequent layer. The expanding mesh approach allows the near wall region to be resolved while saving computational resources with a coarser mesh far away from the wall where the flow characteristics do not change as rapidly. A coarse mesh only was applied to the 31 Sussex geometry due its size and computational restraints.

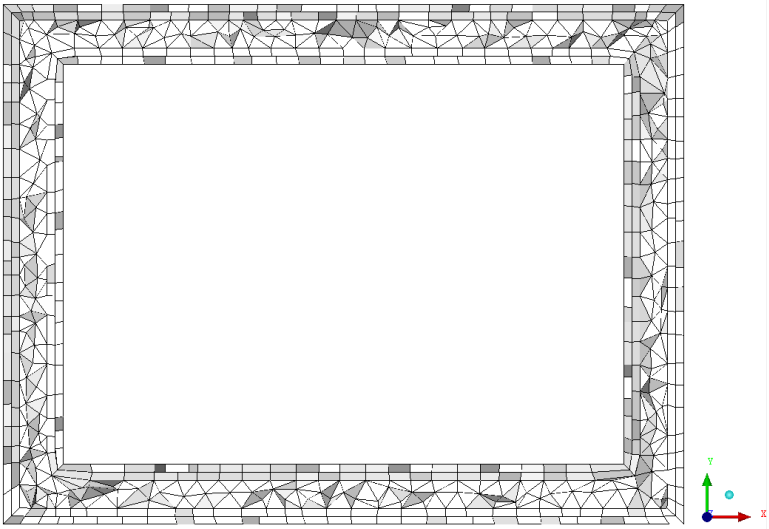

Figure 5.3 - Basic geometry coarse mesh in section

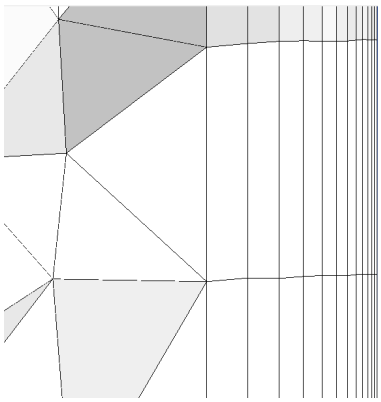

Figure 5.4 - Refined expanding mesh close-up

5.2 CFD Simulation

5.2.1 Computational Resources

The following section outlines the computational resources utilized to complete the simulations for this research

a. Hardware
   - Precision T5500, Intel® Xeon® Processor X5650 2.67GHz

b. Operating System
   - Windows 7, 64-bit (Windows x64)

c. Software
   - ANSYS ICEM CFD, ANSYS Release Version 12.0.1, Copyright 2009 SAS IP Inc.
   - ANSYS Fluent, ANSYS Release Version 12.0.1, Revision: 12.0.16, Copyright 2009 ANSYS Inc.
     - Academic License (maximum limit of 500,000 computational cells)

5.2.2 Model Selection and Settings

5.2.2.1 ANSYS Fluent Settings

Simulations were performed using the popular commercial CFD package ANSYS Fluent 12.0.16. The 3-D, double precision, pressure-based solver was used for all simulations.

In most cases, the single precision solver is sufficiently accurate. However, test simulations run with single precision were not able to achieve as low an error in the total energy balance in the domain as with double precision. Specifically, simulations using single precision were not able to meet the < 1% energy balance convergence criteria (see 5.2.4). Double precision carries more significant digits in the values used for computations and thus lowers round-off error. All simulations were therefore run with double precision

ANSYS Fluent provides a Parallel Processing option, which allows a host computer to access multiple computing nodes to solve multiple processes simultaneously. Multiple nodes can be located on the same computer (multi-core processor) or on different computers in a network cluster. Simulations were run with up to 6 parallel processes, increasing the computational speed by multiple times. Parallel processing was found to be critical for performing transient simulations, which are very computationally expensive. (ANSYS Fluent Theory Guide, 2009)

5.2.2.2 Modelling Natural Convection

Modelling natural convection in a closed domain requires that the total air mass in the domain be constant. There are only two methods to accurately model this scenario which properly conserve mass in the domain. The first is to perform a transient calculation, where the mass is determined based on the initial temperature and pressure, and is properly conserved over time.

The second is to perform a steady state calculation with the Boussinesq approximation for air density (See 3.2). If the ideal gas approximation is used, then the density will change as a function of temperature, and mass will not be conserved. If a constant density is specified for air, then no buoyant forces can act on the flow since there are no density variations. The Boussinesq approximation allows for density variations and properly conserves mass. This approximation is valid as long as temperature differences are small, or specifically when

$$\beta(T - T_o) \ll 1$$

where T_o is the operating temperature. Therefore for air (β = 0.0035 K^{-1}), the approximation is valid for ($T - T_o$) << 286°C or $\Delta T \cong$ 30°C, which should be nearly met for most natural convection problems in buildings. Table 5.4 summarizes the properties of air ANSYS Fluent used in its computations. (ANSYS Fluent User Guide, 2009)

Table 5.4 - Air properties

Dynamic viscosity	μ	1.789 x 10^{-5} kg/ms
Kinematic viscosity	$v = \mu/\rho$	15.16 x 10^{-5} m^2/s
Thermal diffusivity	α	2.0 x 10^{-5} m^2/s
Density	ρ_{air}	1.18 kg/m^3
Specific heat	$c_p\ (air)$	1006 J/kgK
Thermal expansion coefficient	β	0.0035 K^{-1}
Thermal conductivity	$k\ (air)$	0.0242 W/mK

5.2.2.3 Turbulence model and near wall treatment

Natural convection or buoyant flow is generally turbulent (Rundle et al. 2011). For air with a temperature difference of 20°C and a characteristic length of L=3m,

$$\frac{Gr}{Re^2} \gg 1$$

$$Ra \approx 6 \times 10^{10}$$

Therefore the flow is expected to be turbulent with strong buoyancy forces.

The RNG k-ϵ or standard k-ω turbulence models were used in all simulations. Both models have been validated in the literature (Rundle et al. 2001, Gan et al. 2006) for buoyant flows and are able to account for low Reynolds number effects when applied in ANSYS Fluent. The default Model Constants were used for both models (ANSYS Fluent Theory Guide, 2009). The enhanced wall treatment was applied with the RNG k-ϵ model, with the Full Buoyancy Effects option applied. The Full Buoyancy Effects option essentially accounts for buoyant effects in the dissipation of turbulent kinetic energy. When the model was used with a refined mesh the Differential Viscosity Model option was applied to account for low Reynolds number effects in the near wall region.

The standard k-ω turbulence model applies the Enhanced Wall Functions wall treatment automatically. When the model was used with a refined mesh the Low-Re Corrections option was applied to account for low Reynolds number effects in the near wall region.

5.2.2.4 Discretization

Table 5.5 and 5.6 summarize the solution methods used for all steady state and transient simulations respectively. Refer to the Theory section 3.4.2 for a full description of these methods and their suitability for this application.

Table 5.5 - Steady state solution methods

Property	Scheme
Pressure-velocity coupling	SIMPLE
Gradient	Green-Gauss Node Based
Pressure	Body Force Weighted
Energy	Second Order Upwind
Momentum	Second Order Upwind
Turbulent kinetic energy	Second Order Upwind
Turbulent dissipation rate*	Second Order Upwind
Discrete ordinates	Second Order Upwind

***** same scheme applied for specific turbulent dissipation rate as used in the standard k-ω model

Table 5.6 - Transient solution methods

Discretization	Scheme
Pressure-velocity coupling	COUPLED
Gradient	Green-Gauss Node Based
Pressure	Body Force Weighted
Energy	Second Order Upwind
Momentum	Second Order Upwind
Turbulent kinetic energy	Second Order Upwind
Turbulent dissipation rate	Second Order Upwind
Discrete ordinates	Second Order Upwind
Transient formulation	First Order Implicit

5.2.2.5 Solution Controls

Table 5.7 summarizes the under-relaxation factors used for all steady state simulations. All values were set to the ANSYS Fluent default values except the energy under-relaxation factor which was lowered from 1.0 to 0.9 for stability reasons.

Table 5.7 - Steady state under-relaxation factors

Property	Value
Pressure	0.3
Density	1
Body forces	1
Momentum	0.7
k	0.8
ε	0.8
Turbulent viscosity	1
Energy	0.9
Discrete ordinates	1

Lowering under-relaxation factors excessively led to a stable solution which was not accurate. In this case the residual criteria were met; however, the energy balance criterion was not and the final solution was highly dependent on the initialized valued. This highlights the importance of the energy balance convergence criterion discussed in 5.2.4.

Steady state simulations were run initially with the default under-relaxation factors. However, this led to high levels of oscillation which in some cases resulted in unstable solutions. In these cases, the energy under-relaxation factor was reduced from 1.0 to 0.9. Most simulations required the energy under-relaxation factor to be lowered to 0.9. Lowering the energy under-relaxation factor below 0.9 is not recommended as it may never lead to convergence i.e. the correction terms in the iteration process are too small to adjust the solution towards proper convergence. Further refinement of the momentum under-relaxation factor from 0.7 to 0.3 or lower allowed

residuals to meet the convergence criteria. Reducing under-relaxation factors in general leads to longer computation times.

For transient simulations, the default under-relaxation factors provided stable converged solutions. This is a result of the COUPLED pressure-velocity coupling scheme and its ability to reach convergence more quickly by solving the flow equations simultaneously. Table 5.8 summarizes the under-relaxation factors used for all transient simulations.

Table 5.8 - Transient under-relaxation factors

Property	Value
Courant Number	200
Explicit Relaxation Factor Pressure	0.75
Explicit Relaxation Factor Momentum	0.75
Density	1
Body forces	1
k	0.8
ε	0.8
Turbulent viscosity	1
Energy	1
Discrete ordinates	1

5.2.2.6 Radiation model

Radiation Model Selection and Settings

The DO model is the only radiation model with the ability to model semi-transparent surfaces and was therefore selected for every simulation (See Theory 3.3.5.2). For simplicity, all surfaces including the glazing were assumed diffuse, meaning that radiation is reflected equally in all directions as opposed to specularly.

It was found that for the simple geometry of this problem, the default 1 x 1 θ and ϕ pixelation and 2 x 2 angular discretization ($N_\theta = 2, N_\varphi = 2$) was sufficient in that higher resolutions afforded no substantial increase in accuracy.

The DO model uses the absorption coefficient a of the semi-transparent surface to determine the extent to which radiation is transmitted and absorbed. A two band model was used representing the visible (λ ≤ 700nm) and infrared band (λ > 700nm).

For the glass window with two 3mm panes used in the model, the absorption coefficient for the visible band was 46, and for the IR band was 88 as summarized in Table 5.9. The values were determined based on Table 5.1 and Equation 43.

Table 5.9 - Fenestration absorption coefficient

	U-Value (W/m^2K)	α visible	α IR
Double glazed low-e clear	1.99	46	88

Night Radiation

The DO model is necessary to properly simulate the semi-transparent surface in the model. The night time simulation serves the purpose of properly calibrating the boundary conditions. In addition to the mixed convection/radiation boundary condition, ANSYS Fluent includes an additional term at an external semi-transparent surface,

$$Q_{ext} = \varepsilon_{ext}\sigma T_{rad}^4 \tag{62}$$

where T_{rad} is the external surface radiation temperature (ANSYS Fluent Theory Guide, 2009). This term effectively adds a radiation boundary condition of 0K (-273°C), therefore the radiation from the surroundings must be applied as an additional flux in the DO model at the semi-transparent surface.

$$Q_{surr} = \varepsilon_{ext}\sigma T_{surr}^4 \tag{63}$$

Indeed it was found that without this term, temperatures existed below T_{surr} = -5 °C, which is not physically realistic. A flux of Q_{surr} = 173 W/m^2 was applied to account for radiation from the surroundings in all subsequent night, day, and transient simulations.

5.2.3 Boundary Conditions

Typical winter conditions for Toronto, ON were assumed (Environment Canada, 2010).

- External air temperature: -5°C
- Internal air temperature: 21°C

The convective boundary condition was used for the internal and external walls with heat transfer coefficients of $8W/m^2K$ and $33W/m^2K$. These values were approximated from ASHRAE Fundamentals 2009. By specifying the wall thickness for each boundary, Fluent calculates conduction heat transfer through a simple equation negating the need for solid meshing.

The mixed convection/radiation boundary condition was applied on the glazed surface. The ground was set to a constant temperature condition of 0°C.

Solar-ray tracing was used to determine the direct and normal solar flux, and solar ray vector shown in Table 5.10. These values were determined automatically with the solar-calculator based on a selected location time/day for "Fair Weather Conditions":

Table 5.10 - Solar ray tracing irradiation levels

Dec 21, 12:00pm, 43^{o} N 79^{o} W (Toronto, ON, Canada)	
Sun Direction Vector: X: -0.915161, Y: 0.399037, Z: 0.057009 (solar angle of 23.6^{o})	
Sunshine Fraction: 1	
Direct Normal Solar Irradiation (at Earth's surface)	863.806 W/m^2
Diffuse Solar Irradiation - vertical surface:	59.7668 W/m^2
Diffuse Solar Irradiation - horizontal surface	49.2369 W/m^2
Ground Reflected Solar Irradiation - vertical surface	39.3927 W/m^2

The Scattering Fraction, i.e. the fraction of the reflected solar radiation distributed uniformly among all participating surfaces was set to 0.3. This value was lowered from its default value of 1.0 since a significant fraction (70%) of the reflected solar radiation will be lost through the glazing. The value of 0.3 was approximated based on the average transmissivity of the glazing

$$scattering\ fraction\ \approx 1 - \frac{1}{2}(T\ IR + T\ visible) \approx 0.3 \tag{64}$$

The Sol-adjacent Fluid Cells option was applied meaning the heat source terms are applied directly to the wall adjacent fluid cells as opposed to the 1D conduction wall cells.

The Ground Reflectivity was set to the default value of 0.2 to account for ground reflected solar radiation which is applied as diffuse irradiation.

Solar loading is determined by the transmissivity and absorptivity of the glazing surface for the visible and infrared (IR) radiation bands from Table 5.1. Only the glazing surface and south facing internal wall were set to participate in Solar Ray Tracing. Table 5.11 and Table 5.12 summarize the solar energy applied as source terms in the fluid cells adjacent to the participating walls for the Basic and 31 Sussex geometry respectively.

Table 5.11 - Basic geometry solar load model energy source terms

	Glazing	South facing internal wall
Energy Source (W)	1980.8	4668.3
Internally Scattered Energy (W)	780.5	
Total Energy Source (W)	6649.1	

Table 5.12 - 31 Sussex geometry solar load model energy source terms

	Glazing	South facing internal wall
Energy Source (W)	7930.4	19369.2
Internally Scattered Energy (W)	3152	
Total Energy Source (W)	27299.7	

5.2.4 Convergence Criteria

There are no universal or standard criteria for judging convergence. The default convergence criterion used by ANSYS fluent is based on a threshold value for the residuals of transported properties including mass, energy, momentum, and the appropriate radiation residual when a radiation model is applied. For most problems, the default convergence criterion is sufficient, requiring that all scaled residuals decrease to 10^{-3} for all equations except energy which must decrease to 10^{-6}.

The residual based convergence criterion alone was found to not be sufficient for all cases. Therefore multiple criteria were used to better assess convergence. Clearly, for steady state simulations, the total energy transfer into the domain must equal the total energy transfer out of the domain. A maximum difference of 1% between these values was used as an additional criterion. In summary, convergence was deemed accurate when the following criteria were met

1. Total energy balance in the domain < 1% net difference for steady state simulations
2. All residuals < 1×10^{-3} and the energy < 1×10^{-6}

Figure 5.5 shows the plot of the residuals from a steady state day time simulation for the Basic geometry using the standard k-ω turbulence model. The under-relaxation factors were set according to Table 5.5. After approximately 800 iterations, the momentum under-relaxation factor was reduced to 0.3, allowing the residuals to meet the convergence threshold.

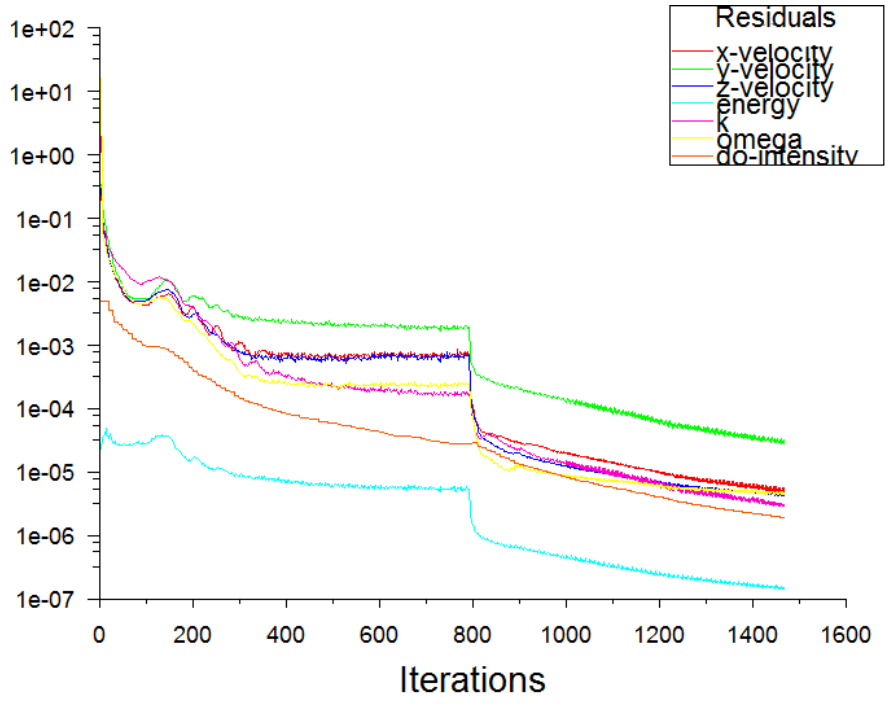

Figure 5.5 - Residual plot for basic geometry (y+ = 46)

5.2.5 Transient Simulations

Steady state simulations solve the domain at an instant in time. In reality, this represents a system under constant boundary conditions which has reached equilibrium after an indefinite period of time. Real systems may never reach steady state if the boundary conditions change too quickly. In the example of air flow in a building, the thermal diffusivity of the fluid and material are only accounted for in the transient case. The thermal diffusivity α (m^2/s) describes the rate at which heat is conducted through a material

$$\alpha = \frac{k}{\rho c_p} \tag{65}$$

where k is the conductivity (W/mK) , and c_p is the specific heat capacity (J/kgK). Essentially the thermal diffusivity is a measure of how quickly a material will heat up. The thermal diffusivity of air is $\alpha_{air} \approx 2 \times 10^{-5}$ m^2/s and for a brick/insulation wall is $\alpha_{wall} \approx 5 \times 10^{-7}$ m^2/s.

$$\frac{\alpha_{wall}}{\alpha_{air}} \approx 40$$

Therefore air heats up approximately 40 times faster than the wall material. However in a building, a significant thermal mass in the walls will limit the rate at which the air heats up. An order of magnitude estimate of the rate of temperature rise for the walls will give an indication of the importance of the thermal diffusivity of the wall. This

will suggest whether a transient solution is necessary or not. The rate of temperature rise in the wall is dependent on the mass, heat capacity and heat flux by

$$Q = mc_p \frac{dT}{dt} \tag{66}$$

Where the heat capacity of the wall is c_p = 900 J/kgK. For the simple shell geometry, the total wall mass is 11745 kg (wall area = 106.1m^2, wall thickness = 0.15m, ρ_{wall} = 738 kg/m^3). Based on the solar ray tracing model in ANSYS Fluent, the total energy source terms in the domain due to solar radiation is 6649.1 W. Thus the rate at which the walls heat up is

$$\frac{dT}{dt} \approx 2\,℃/hr$$

This value represents an order of magnitude estimate for how quickly the building structure will heat up. At this low rate, the system may not have enough time to reach steady state based on how quickly the solar boundary conditions change, and thus transient simulation may be necessary. For example, the direct normal radiation increases by approximately 306W/m^2 between 7:30am and 8:00am (ASHRAE Fair Weather Conditions), changing from 0 to 35% of the maximum irradiation in just 30 minutes. Thus transient simulation will be especially important early and late in the day, when the direct normal radiation changes most rapidly.

The standard k-ω turbulence model was used for all transient simulations as it was found to be faster than the RNG k-ϵ model and yield very similar results in the steady state case. The coarse mesh was used for all transient simulations due to the massive computational expense of running transient simulations.

The time step size was 2s for all simulations. This resulted in the solution converging after approximately 5 iterations. Figure 5.6 is a sample plot of the residuals over a period of 40 iterations. In this case 4 iterations represent a time step of 2s. After each time step, the residuals spike as ANSYS Fluent recalculates the solution at the new time. The energy residual rises above the 1 x 10^{-6} convergence threshold at each time step and then falls back down. It should be noted that the convergence criterion for every residual was not strictly met at all times during the simulation, but at times hovered very near it. The 2s time step size however ensured that the energy residual always met the convergence criteria.

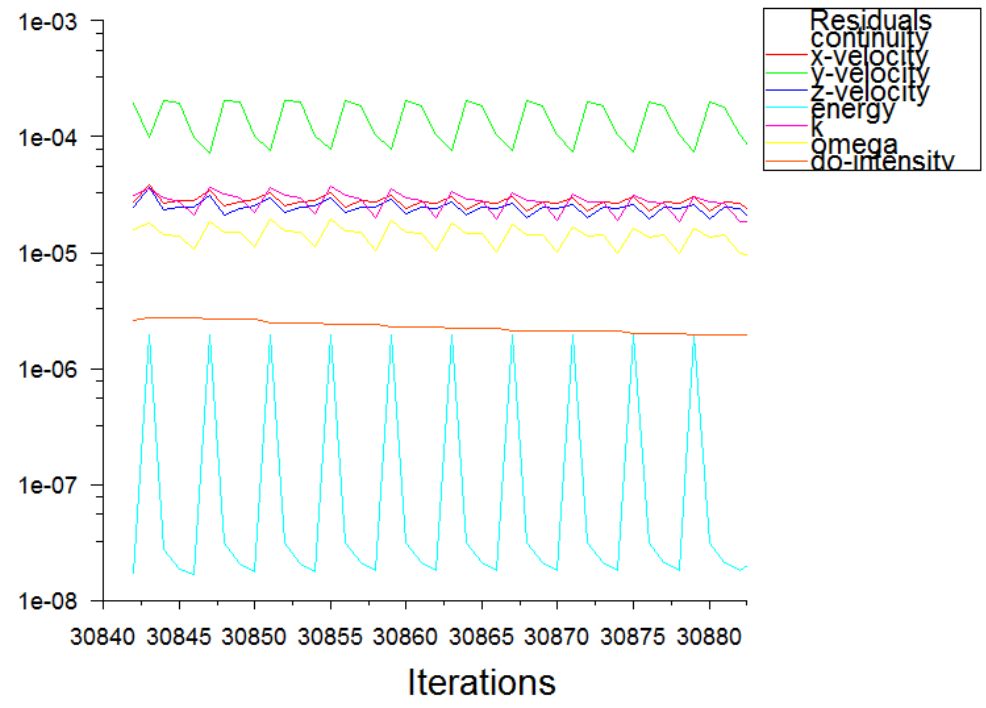

Figure 5.6 - Basic geometry transient sample residual plot

Figure 5.7 shows the solar irradiation data from the ANSYS Fluent Solar Calculator for Dec 21 (43°N 79°W). The maximum solar radiation occurred at 12:14pm with a direct normal value of 864.8W/m^2.

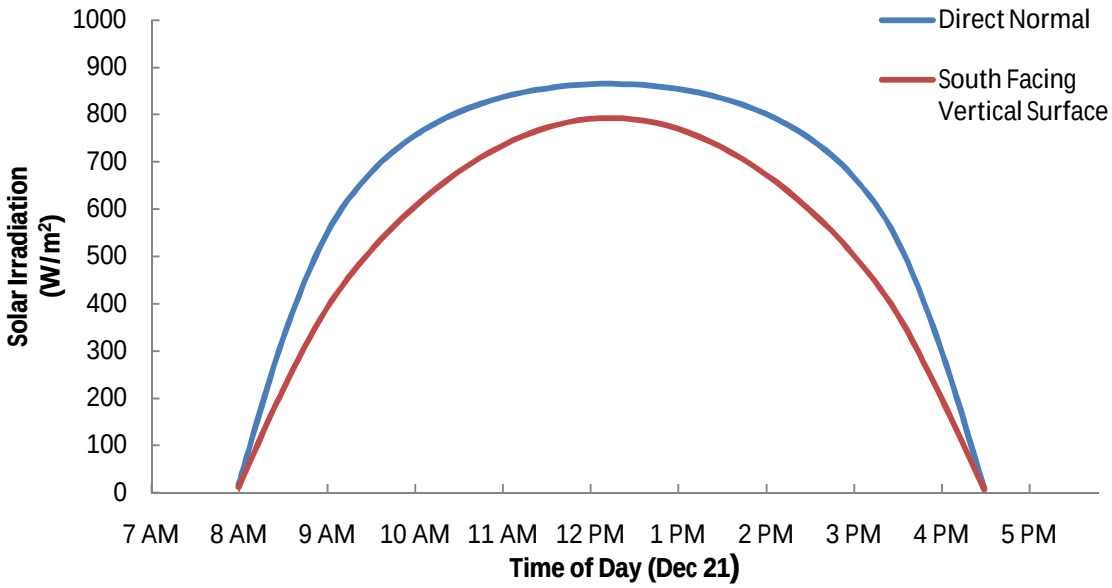

Figure 5.7 - Solar irradiation levels

5.2.6 Heat Pump Model

A simplified heat pump model was created with the function of extracting heat from the perimeter space. The output of the heat pump would realistically depend on the heat load in the core and would vary over a 24 hour period as the boundary conditions change, and thus a transient simulation is ideal. However, for simplicity, the following model was applied only in the steady state case. The level of irradiation was set to the average over the day. From Figure 5.7, the average direct irradiation on a vertical surface averaged over the day was 492W/m^2. The diffuse irradiation was estimated to be 62W/m^2.

In the practical case, the core would serve as the heat sink, maintaining its temperature at 21^{o}C. For this model, the core was not meshed and was assumed to be at 21^{o}C. The heat load for the core was estimated using a simple 1D conduction calculation.

- outdoor temperature of -5^{o}C and perimeter at 5^{o}C: core heat load ≈ 2kW
- winter design temperature of -18^{o}C and perimeter at 0^{o}C: core heat load ≈ 3kW

These values were used as a rough general range to specify the output of the heat pump.

The heat pump model was based off the Mitsubishi Mr. Slim series heat pumps shown schematically in Figure 5.8 (working in cooling mode). A fan located behind the front grille draws air through grilles on the side and out the front of the unit.

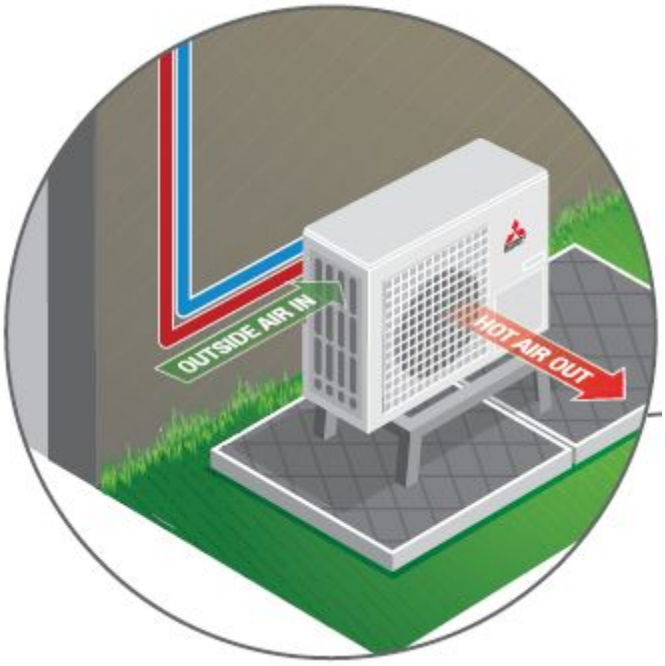

Figure 5.8 - Mr. Slim heat pump schematic (cooling mode)

The specifications for the Mr. Slim MSZ-GA24NA are summarized in Table 5.13 (Mr. Slim M-Series Specifications, 2011)

Table 5.13 - Mr. Slim heat pump specifications

Model	MSZ-GA24NA
Dimensions (in)	33-7/16 x 33-1/16 x 13
Heating Capacity	1055 – 7149 W (3600 – 24400 Btu/hr)
COP (seasonally averaged)	2.8 (HSPF = 9.5)
Air Flow Rate	0.140 – 0.294 m^3/s (296 – 624 cfm)
Temperature Range	-10 – 24 ^oC DB

The heat pump model included a fan, heat exchanger, and solid aluminum casing surrounding the volume. The fan draws air through the heat exchange surface as shown in Figure 5.9. The heat pump was located in the bottom cavity centred under the floor of the core space as shown in the inset of Figure 5.9. The major geometric simplification was that the air was not entering through side grilles as is the case with the Mr. Slim unit.

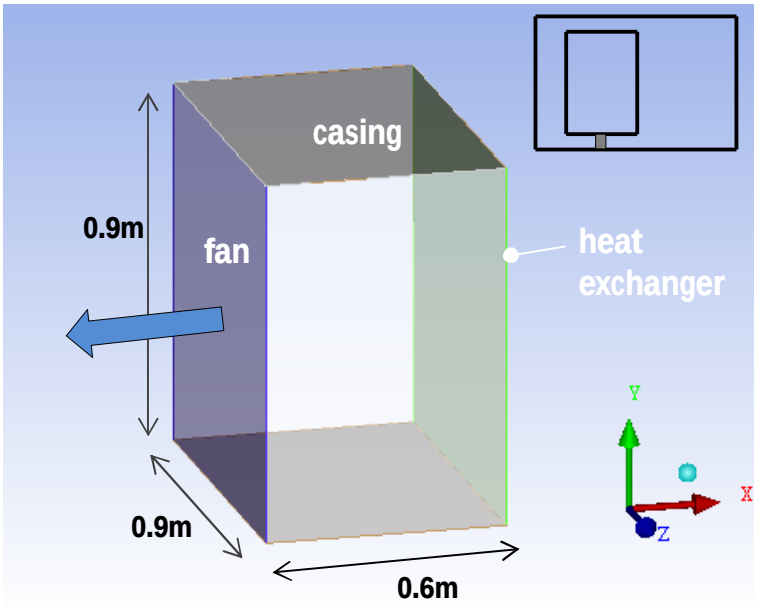

Figure 5.9 -Heat pump model geometry and location within 31 Sussex geometry shown inset

An infinitely thin internal surface was used to represent the fan. The fan was modelled by specifying a constant pressure jump and a direction. The constant pressure jump was selected such that the resulting volume flow rate matched that of the Mr. Slim heat pump, i.e. approximately 0.3m^3/s (624 cubic feet per minute).

The heat pump heat exchanger (evaporator) was modelled as another infinitely thin surface using the simplified radiator boundary condition in ANSYS Fluent. The heat exchanger flux is given by

$$Q_{hp} = h_{hp}(T_{air} - T_{ref}) \tag{65}$$

Where h_{hp} is the convective heat transfer coefficient, and T_{ref} is the temperature representing the fluid in the evaporator tubing. The heat transfer coefficient can be made dependent on the local flow velocity. The pressure drop across the heat exchanger is given by

$$\Delta p = \gamma \frac{1}{2} \rho U^2 \tag{65}$$

where γ is the pressure loss coefficient and in general is dependent on the local flow velocity. For simplicity the pressure loss coefficient was set to $\gamma = 0$. This assumption is reasonable for this simplified model since the fan is defined by an arbitrary pressure jump.

The heat exchanger model was set to have a reference temperature of $T_{ref} = -10℃$ (based on the lowest value in operating range), and a heat transfer coefficient of $h_{hp} = 250\ W/m^2K$. These values were chosen such that a reasonable heat flux resulted (≈ 2-3 kW) based on the 1D heat load calculation for the core.

6 Results

6.1 Outline

The purpose of this work was to present a simplified model to better understand the phenomena and implications for more complex geometries. The presentation of results follows an order of increasing complexity in the models being simulated. The order also represents the general process undertook during the research process.

First steady state results are presented for the Basic geometry for a night time and a day time (representing peak solar irradiation) simulation. The steady day time simulation was performed to give an indication of the maximum velocities and temperatures possible for this idealized scenario. It was important to consider the night time simulation because the heat pump may operate during the night as well depending on how cool the perimeter gets. Also, Hsu et al. (1981) predicted reverse flow of equal magnitude to the day time flow, driven by heat loss through the glazing surface.

A grid independence study was performed based on steady simulations with the Basic geometry. Grid independence is an essential criterion for any CFD simulation; it means that the solution is not dependent on the mesh used. Due to the computational limit of 500,000 cells for the ANSYS Fluent academic license, a grid independence study using the 31 Sussex geometry was not feasible. However, results from a study of the Basic geometry serve to help estimate the accuracy and limitations of simulations using the large 31 Sussex geometry. As will be shown, simulation results using the coarse (not grid-independent) mesh deviated from results using the refined (grid independent) mesh, but provided a reasonable estimate and captured the important features of the flow and temperature distribution.

Next, the set of results for transient simulations using the Basic geometry and coarse mesh are presented. The importance of transient simulations in accounting for the thermal diffusivity of materials has been described. Furthermore, transient simulations allow for key results such as average temperature and flow rate to be tracked over the entire day, providing a more complete understanding of the convective loop's performance. The computational limit of simulation time necessitated that transient solutions be performed using coarse meshes. Using the Basic coarse mesh, real run times exceeded the simulation time (9hrs) for all transient simulations since a small time step was required for accurately model the transient flow behaviour. The Basic refined mesh, having 3 times more computational cells (see Table 5.3) would likely require a real run time of at least 27hrs. For the 31 Sussex geometry, the transient computational time would far exceed this given the larger scale. Since the coarse mesh provided a reasonably accurate results for the steady state case, all transient simulations were formed using coarse (not grid-independent) meshes.

Finally, results from simulations with the heat pump implemented in the 31 Sussex geometry are presented. These simulations are intended to provide insight into the performance of the NTED™ house. Due to the simplicity of the

heat pump model, a steady state simulation was necessary. An average daily solar irradiation level was used as opposed to the maximum solar irradiation level to better represent the heat pump functionality over the entire day.

6.2 Steady State Simulations

6.2.1 Basic Geometry Night

The night time simulation with a coarse grid (y+ = 46) was run first as a sort of benchmark to ensure the model was producing physical results and to investigate the extent to which flow reversal occurs. Based on a 1D conduction calculation, the average temperature in the perimeter zone should be 3.7°C. Accounting for radiation, lower temperatures are expected.

Figure 6.1 shows the temperature contours on a vertical cross section half way through the geometry in the north-south plane for a solar radiation flux of zero, representing a night time scenario. The RNG k-ϵ turbulence model was used. The temperature on the south facing glazing and inside wall was approximately -5°C as a result of the strong contribution of radiation heat loss. The average temperature in the domain was 0.3°C.

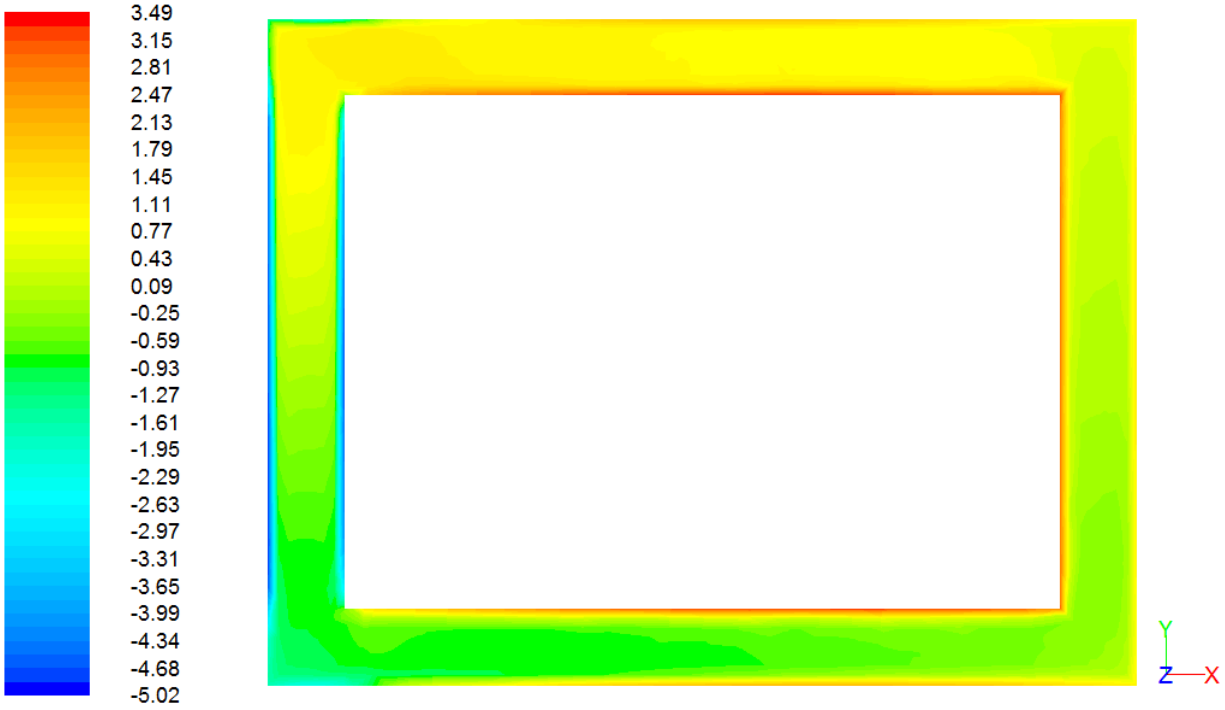

Figure 6.1 – Steady state basic geometry night time temperature (°C) contours (y+ = 46)

Figure 6.2 shows the velocity vectors on the same vertical cross section for the night time scenario with a close up in Figure 6.3.

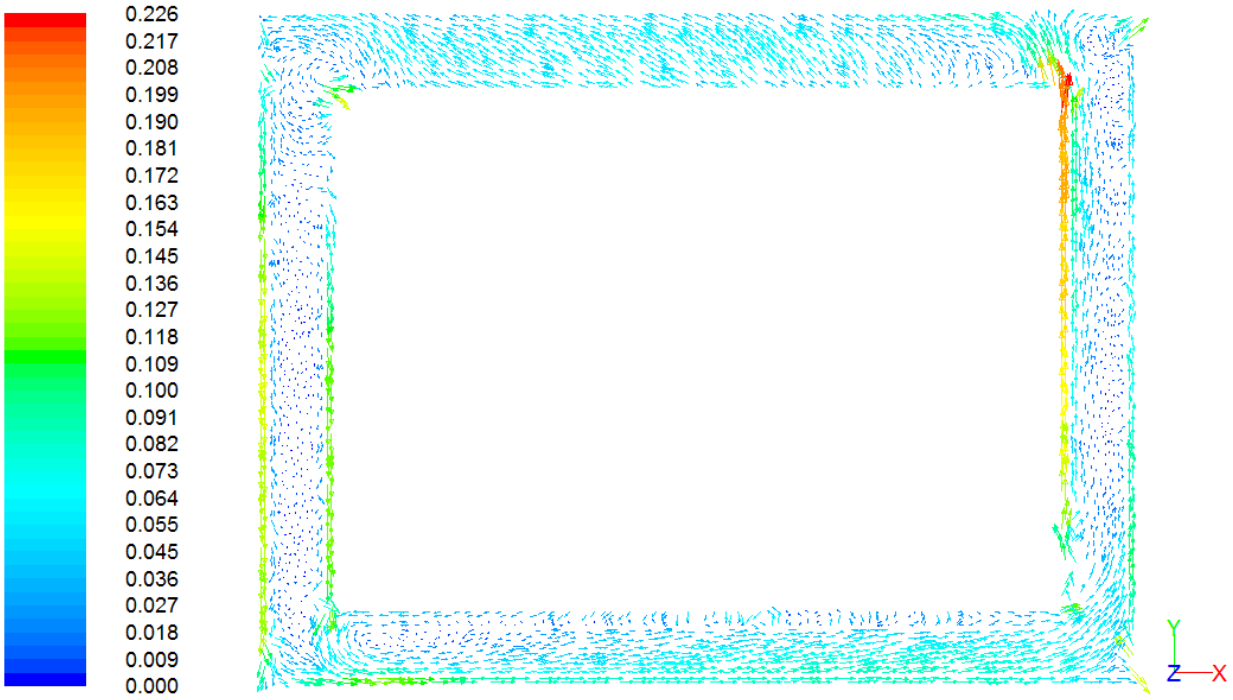

Figure 6.2 - Steady state basic geometry night time velocity (m/s) vectors (y+ = 46)

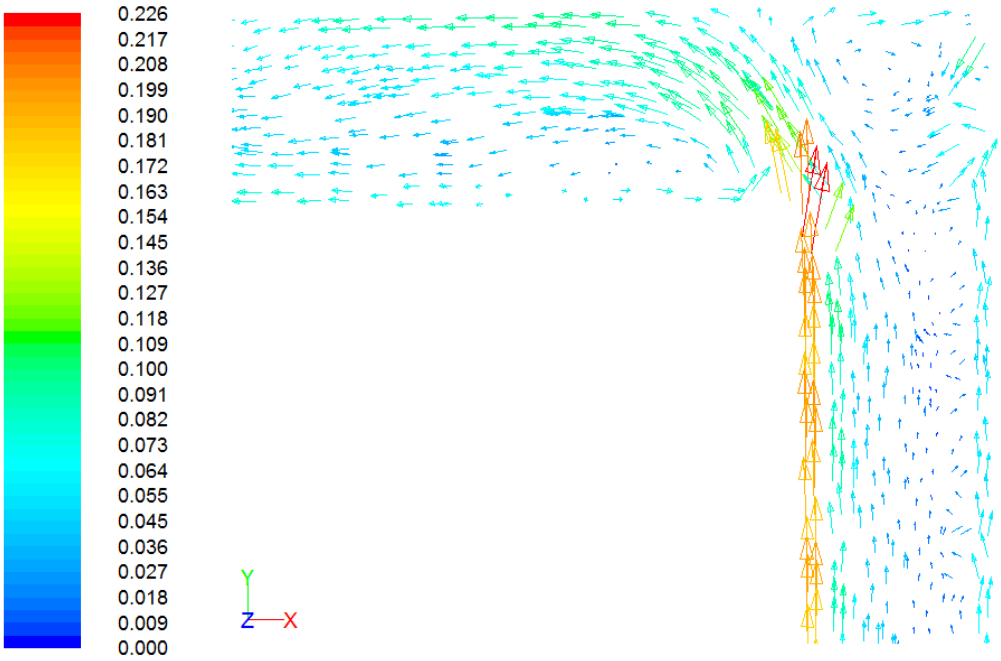

Figure 6.3 - Close-up of Figure 6.2

There was a continuous flow of 0.061m^3/s (0.044m^3/s/m^2) in the counter-clockwise direction. This counter flow is driven by heat loss through the glazing surface in the south perimeter. Therefore, even without solar radiation, the flow is driven by buoyant forces forming a convective loop flow. The reverse volume flow rate is approximately

75% that of the rate for peak solar radiation (See 6.2.2). This result indicates at night heat loss from the core is distributed around the perimeter zone, reducing temperature stratification. The reverse flow also has design implications for an auxiliary heating system in the perimeter space (if needed). Again, the intent would be to distribute auxiliary heat around the perimeter space, such that the inter-zone heat pump could operate more efficiently.

6.2.2 Basic Geometry Day

The results from the daytime simulation using the RNG k-ϵ turbulence model with a coarse grid (y+ = 46) are presented below. Figure 6.4 shows the daytime temperature contours on the vertical section at peak solar irradiation (12:00pm). The average temperature in the domain was 38.5^{o}C. A maximum temperature of 73.3^{o}C was found at the south facing internal wall, 34.5^{o}C higher than the average air temperature. According to sol-air temperature data for January 21 and 45^{o}N Latitude from Hutcheon and Handegord (1995), a south facing dark coloured surface can reach up to 48^{o}C higher than the surrounding air temperature. Behr (1995) studied spandrel glass microenvironments for curtain wall buildings in Missouri, and found that the inside glass temperature surface reached 82.1^{o}C in May 1991. Therefore, it can be concluded that the temperature distribution in the convective loop falls within reasonable limits.

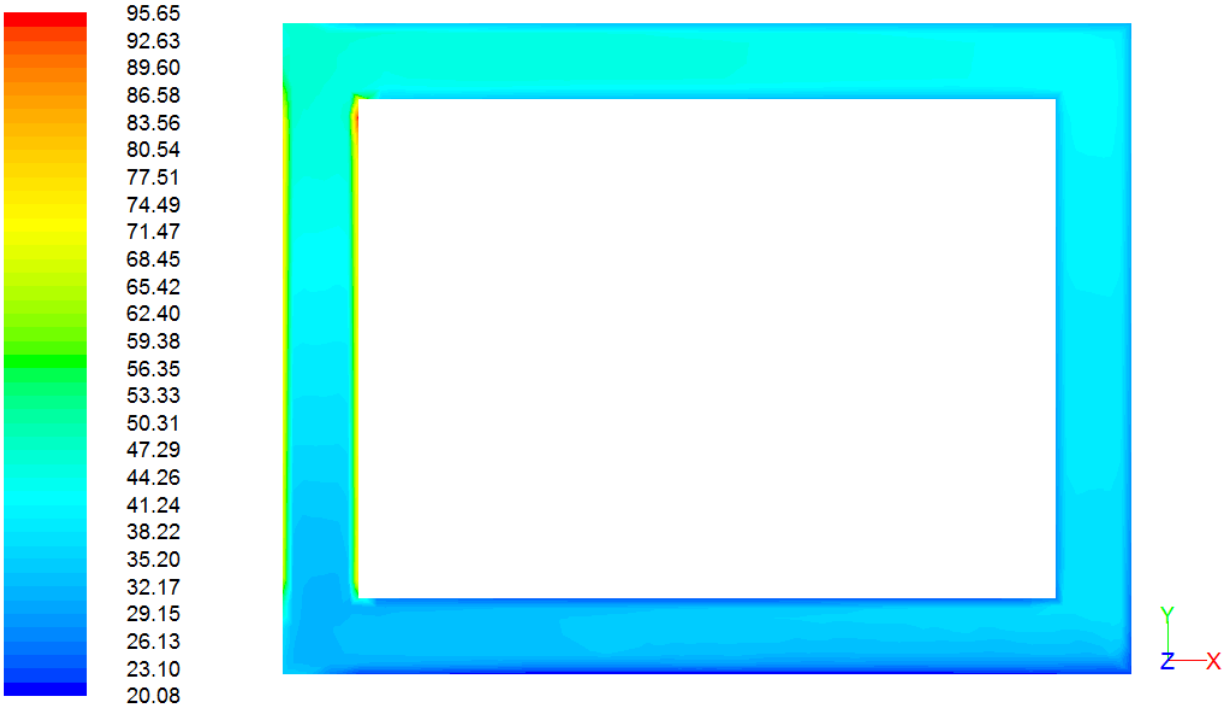

Figure 6.4 - Steady state basic geometry day time temperature (^{o}C) contours, 12:00pm (y+ = 46)

At the very top portion of the internal wall, a localized high temperature region was found, with temperatures up to 95^{o}C. This localized region was found across the entire depth of the surface (and was also present for more

refined meshes). This may be explained by convective heat transfer theory which dictates that the local heat transfer coefficient is lowest at end of the flow path where the boundary layer is larger. However, this must be also considered a possible error and further research beyond the scope of this work is required to investigate this anomaly. Nevertheless this small localized region of high temperature was assumed to have a negligible effect on the average temperature of the south facing internal wall.

It should be noted that average temperatures in the perimeter domain are in excess of comfortable conditions, and well in excess of the 5^0C set point described by Pressnail and Richman (2009). This is a result of the heat pump model not yet being implemented and transient effects not accounted for. Furthermore, the perimeter space's total volume is only 22.9m^3 and is not intended for any occupancy as is the case in the NTED™ house presented thus far. As stated earlier, the purpose of this work was to present a simplified model to better analyze the phenomena and implications for more complex geometries. Figure 6.5 shows the velocity vectors on the vertical cross section for the daytime simulation.

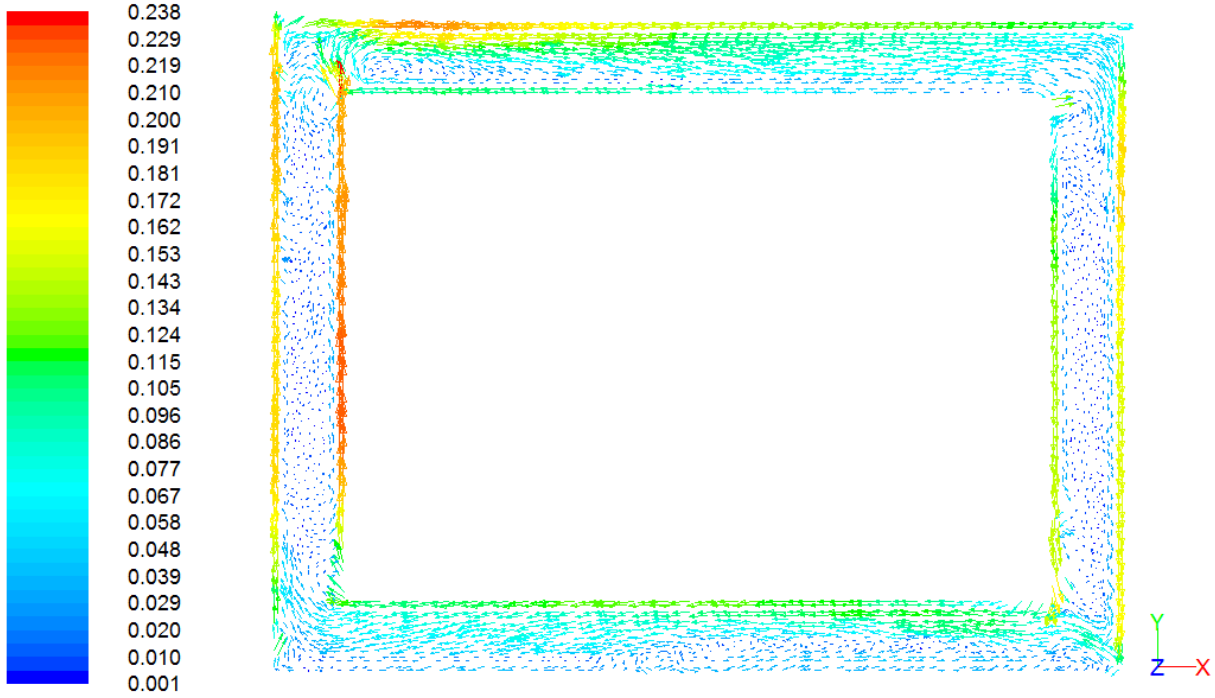

Figure 6.5 - Steady state basic geometry day time velocity (m/s) vector plot, 12:00pm (y+ = 46)

The maximum velocity of 0.24m/s occured at the irradiated internal wall surface where the temperature was highest, as expected for buoyant flow. There was a general clock-wise circular flow around the channel with limited flow reversal along the bottom of the top cavity. The total volume flow through the top and bottom channel were 0.080 m^3/s and –0.080 m^3/s respectively (i.e in opposite directions) or 0.057m^3/s/m^2. The

continuous flow serves as a proof of concept for the convective air loop in a double envelope building. In order to assess the validity of these simulations, the results must be checked for grid independence.

Please refer to Figures 6.10 to 6.13 for close-up view s of the grid independent velocity vector plot.

6.2.3 Grid Independence

The velocity profile along a line at mid height in the south cavity was used to study grid independence in a similar fashion to Rundle et al. (2011). Figure 6.6 shows the velocity profile for the three meshes outlined in Table 5.3, each with a different y+ value for the wall adjacent cell: y+ = 46, y+ = 6, and y+ = 3. The RNG k-ϵ model was used to study grid independence.

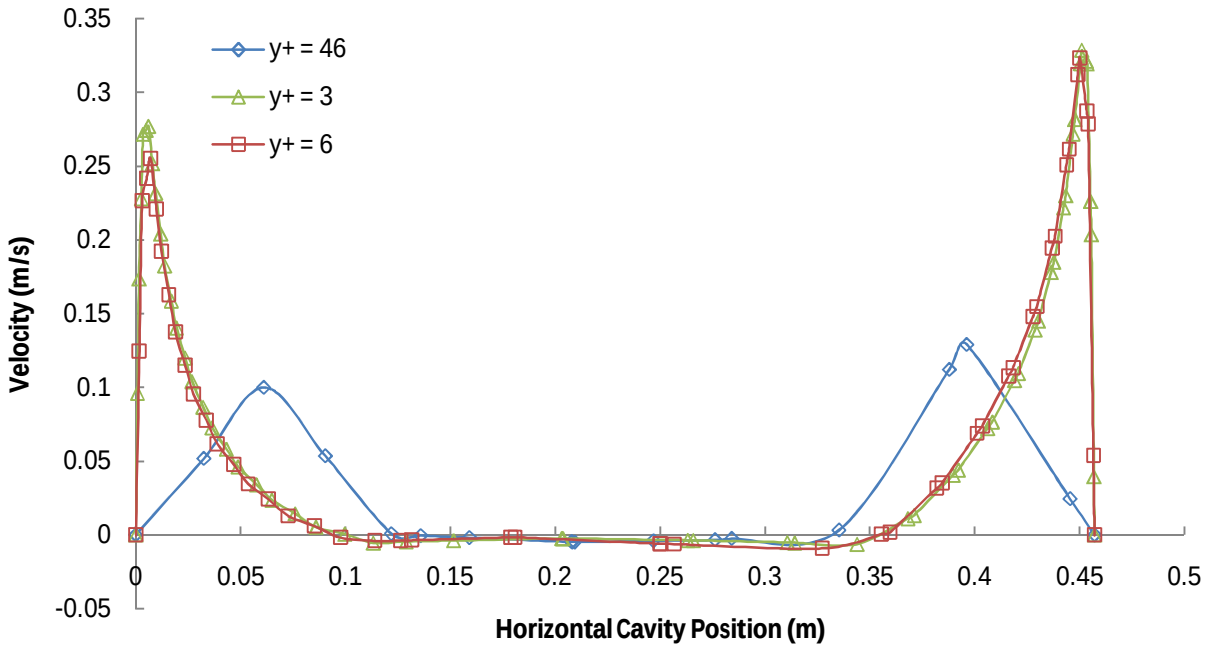

Figure 6.6 - Steady state Basic geometry horizontal velocity magnitude line plot for three mesh densities

The large discrepancy in the y+ = 46 curve is due to the model's use of wall functions to describe the near wall region. The more refined meshes allowed the near wall region to be resolved. The coarse mesh under predicts the maximum velocity magnitude near the wall. Upon further refinement of the y+ = 3 mesh, the velocity profile did not change substantially, indicating that grid independence was achieved.

The temperature along a vertical line centred in the south cavity and spanning the full cavity height is shown in Figure 6.7 for the same three mesh densities.

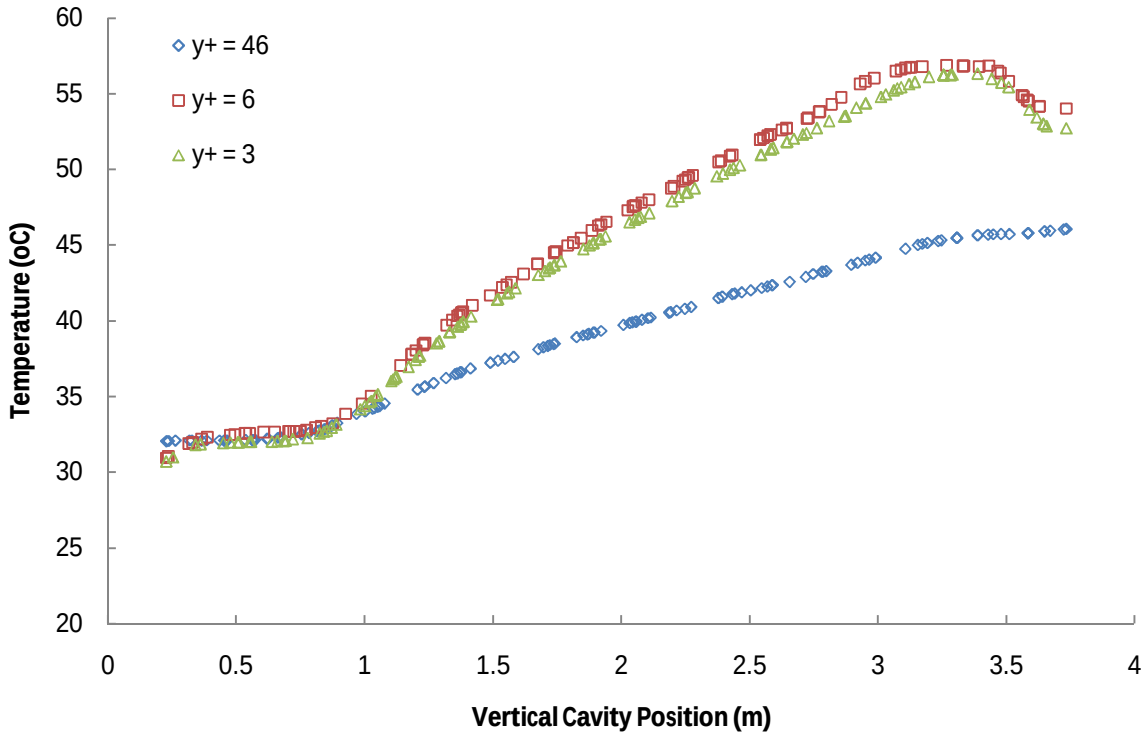

Figure 6.7 - Steady state Basic geometry vertical temperature line plot for three mesh densities

Simulations using the coarse mesh led to under predicted temperatures in the domain. The total average temperature difference between results with the coarse and refined mesh was 42°C -38.5°C = 3.9°C. The maximum temperature difference was 26.4°C.

6.2.4 Turbulence Model Comparison

Figure 6.8 shows the vertical temperature distribution in the south cavity for the RNG k-ϵ and standard k-ω turbulence models for both the refined and coarse meshes. The standard k-ω model led to slightly different temperatures than RNG k-ϵ turbulence for both the refined (y+ = 3) and coarse (y+ = 46) meshes. The difference in the total average temperature between models for the coarse and refined mesh was 1.8°C and 0.3°C respectively. Figure 6.9 shows the horizontal velocity profile in the south cavity for the RNG k-ϵ and standard k-ω models using the refined mesh. There was no substantial difference between the models characterization of the flow field in this region.

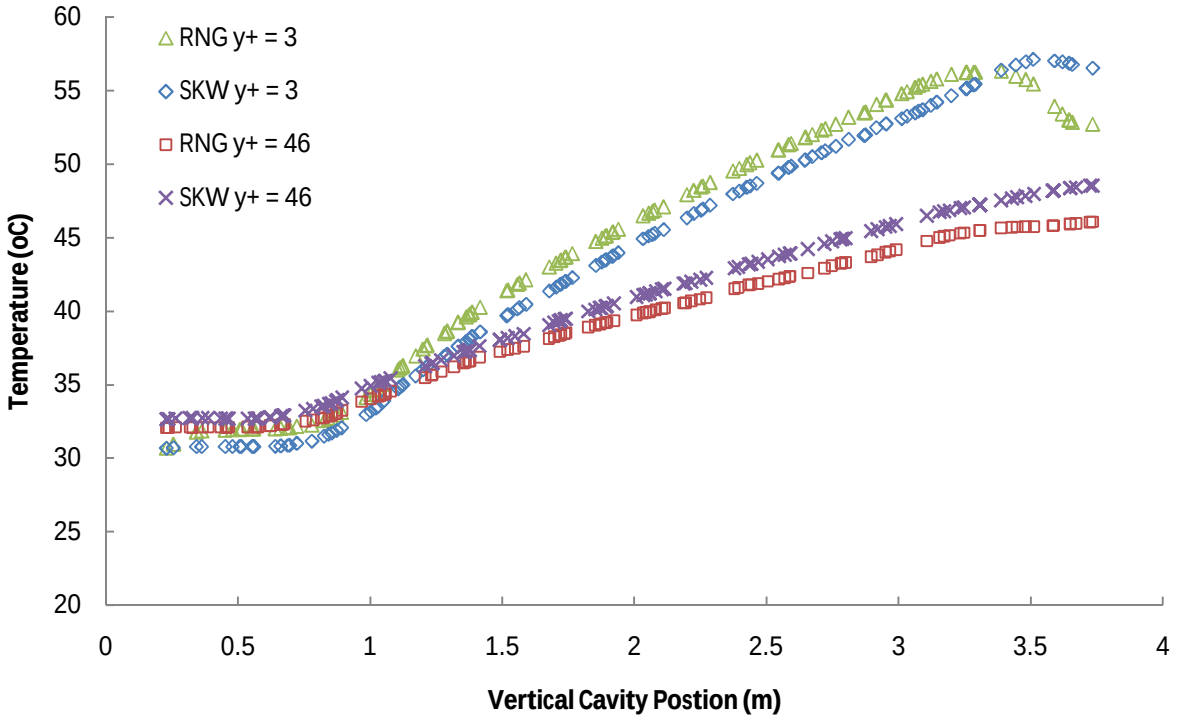

Figure 6.8 - Steady state Basic geometry vertical temperature line plot comparing turbulence models

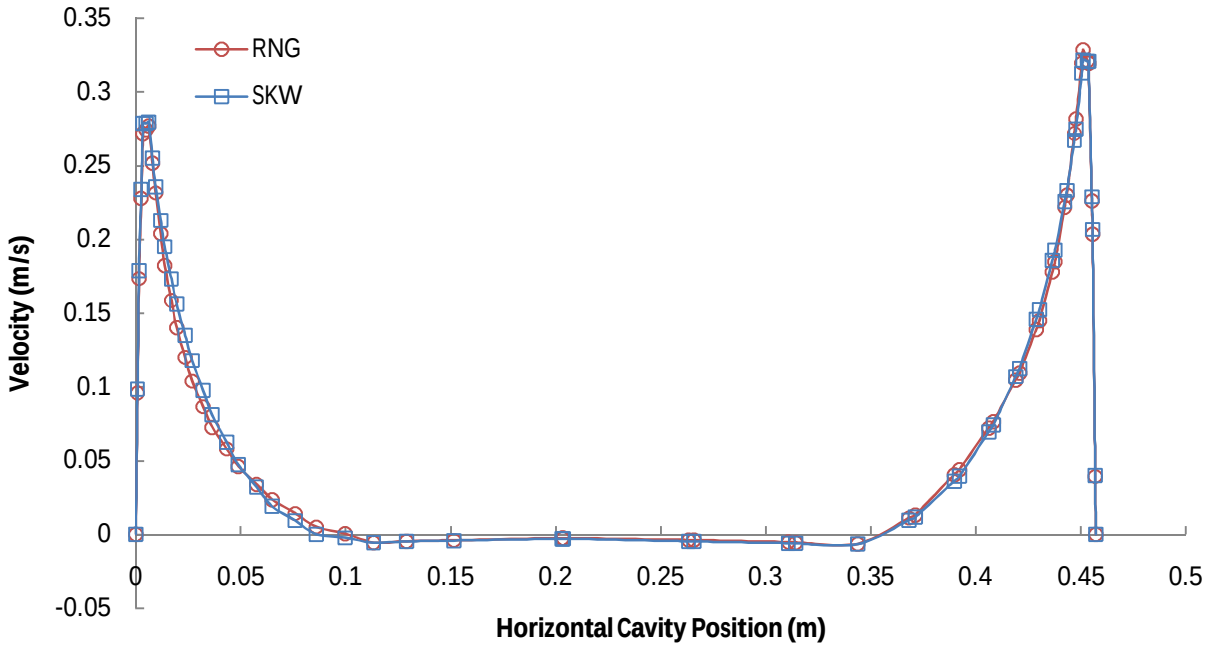

Figure 6.9 - Basic geometry horizontal velocity line plot comparing turbulence models (y+ = 3)

6.2.5 Summary

Figure 6.10 shows the velocity vectors on the vertical section for the refined mesh, representing grid independent results. A maximum velocity of ~0.37 m/s occured at the irradiated internal wall surface where the temperature was highest, as expected for buoyant flow. These velocities fall in the same range as those described by Jones et al. (1982) for the Mastin House. The volume flow rate was 0.049m^3/s or 0.035m^3/s/m^2. The coarse mesh over predicts the volume flow rate significantly, by approximately 48%.

Figures 6.11 to 6.14 show close-up sections of each corner of the loop. Each plot gives an indication of flow reversal.

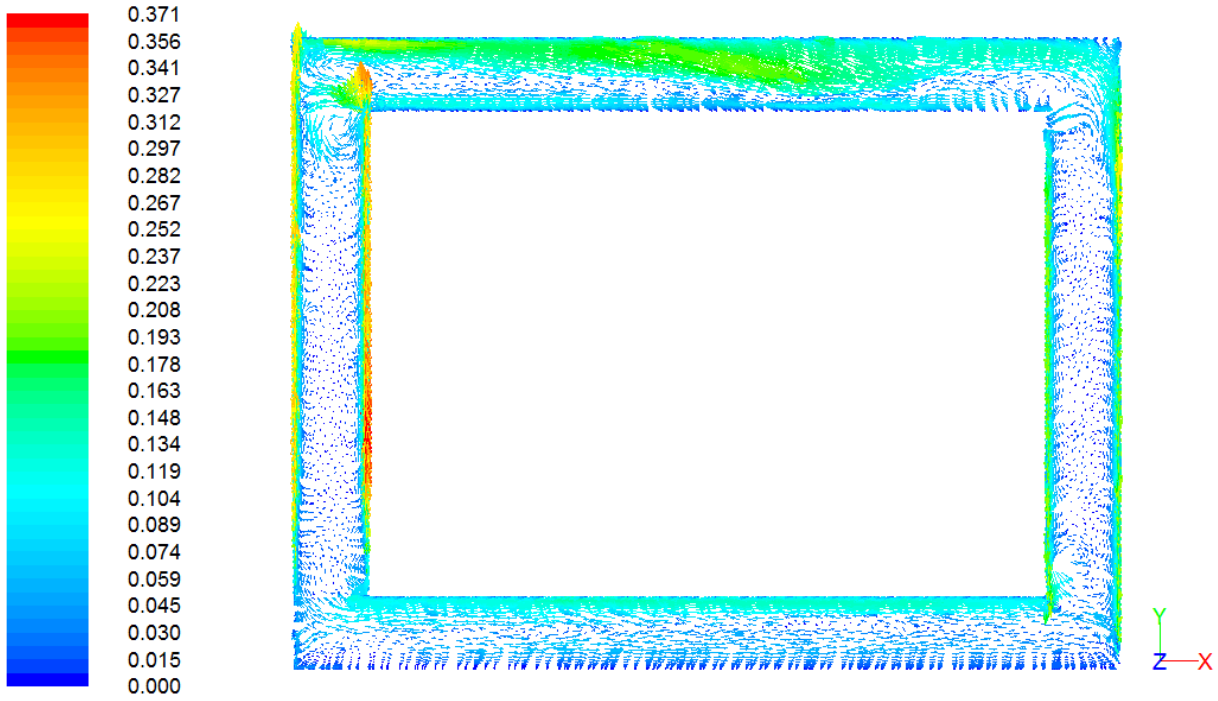

Figure 6.10 - Steady state basic geometry velocity (m/s) vectors for grid independent mesh (y+ = 3)

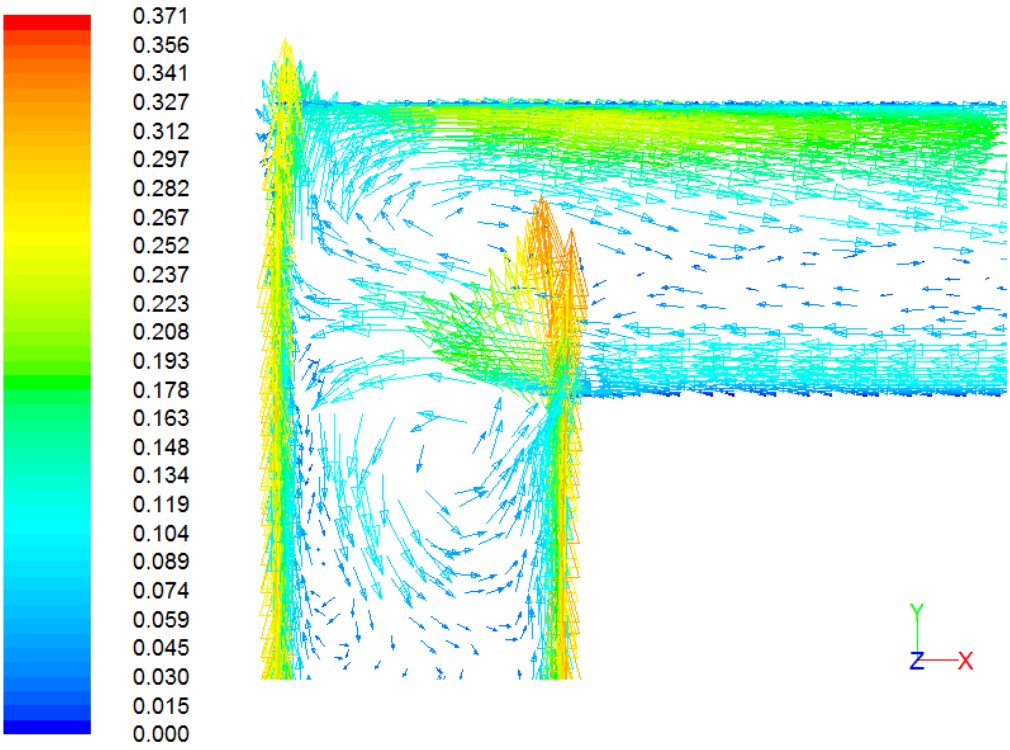

Figure 6.11 – Top left corner close-up of Figure 40 (m/s)

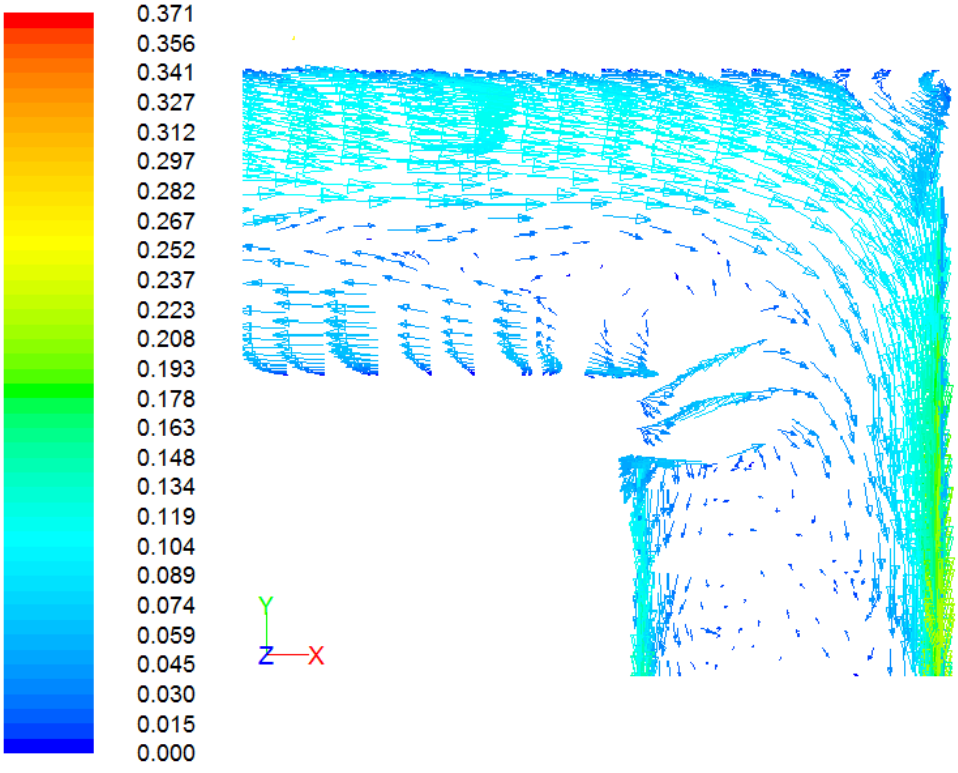

Figure 6.12 - Top right corner close-up of Figure 40 (m/s)

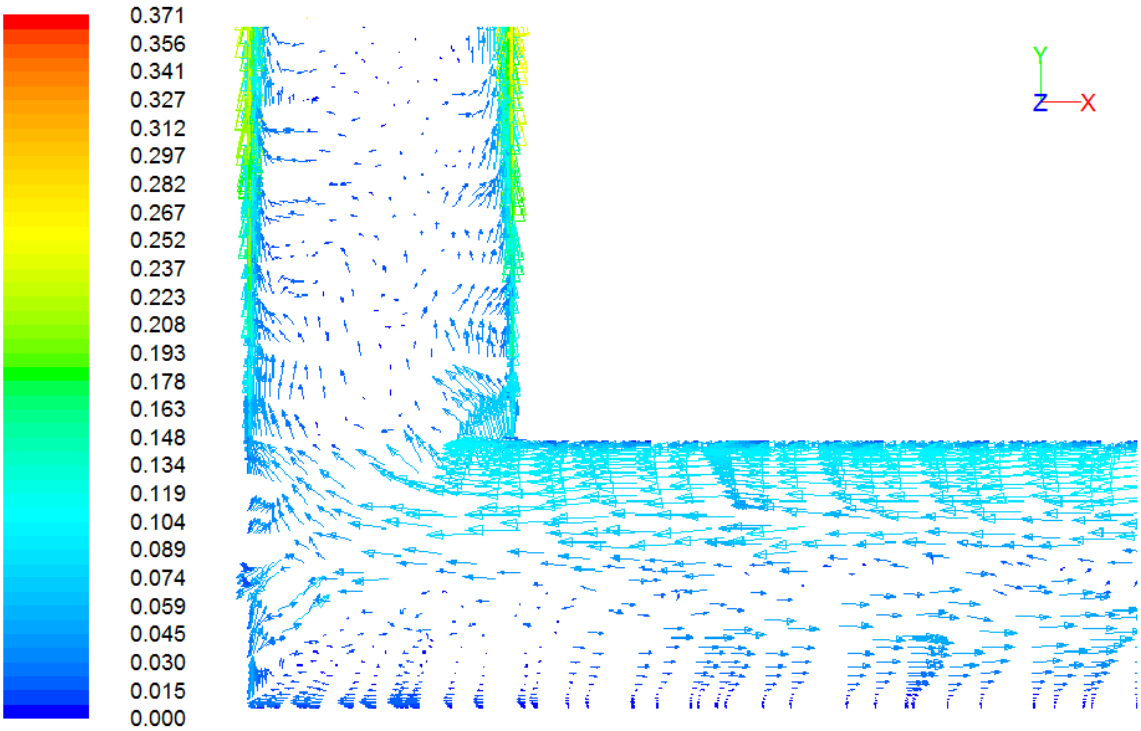

Figure 6.13 - Bottom left corner close-up of Figure 40 (m/s)

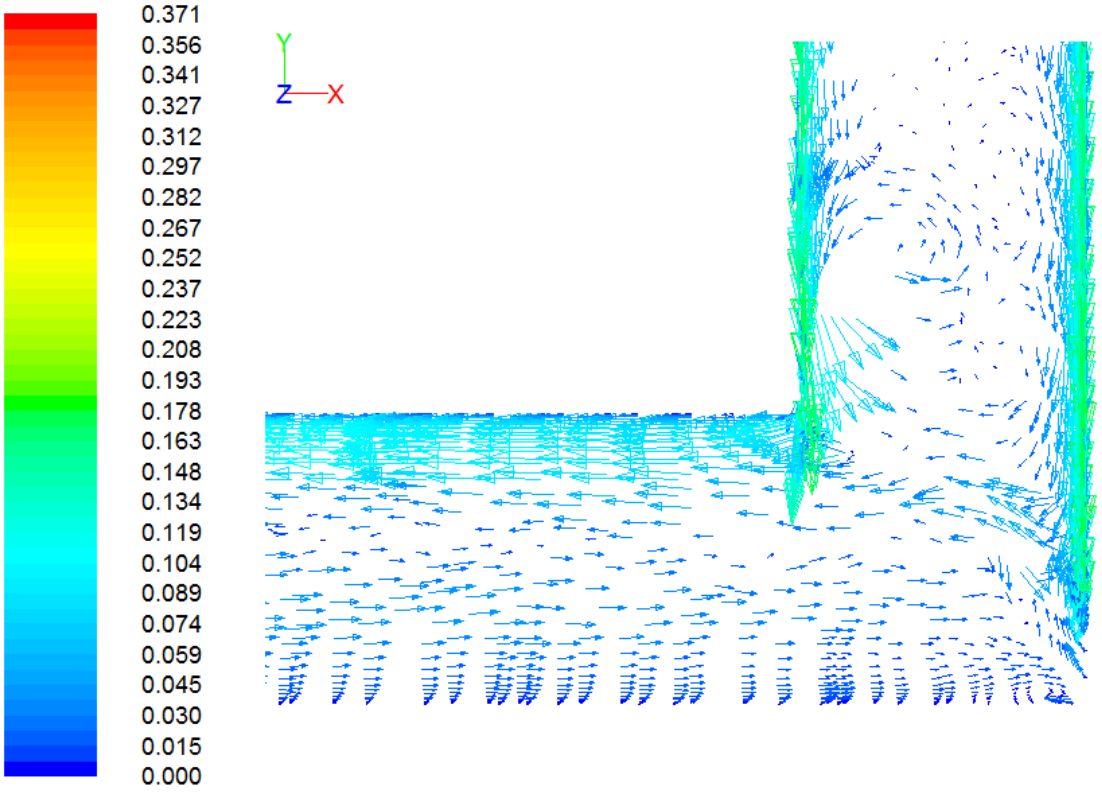

Figure 6.14 - Bottom right corner close-up of Figure 40 (m/s)

Table 6.1 shows the total heat transfer rate though the boundary surfaces. The negative sign indicates that heat is flowing out of the domain. The total heat transfer rate is compared to the total solar gain as dictated by the solar load model. A full break down of the solar load source terms can found in the Appendices Table 10.1. The total heat transfer rate includes all forms of heat transfer including radiation.

Table 6.1 - Boundary surface total heat fluxes

Boundary surface	Total Heat Transfer Rate (W)	Radiation Heat Transfer Rate (W)
External walls	-760	-88
Ground	-462	-333*
Roof	-459	-74
Internal walls	-585	3644
Glazing	-4384	-3150
Net heat transfer rate	-6650	-1
Total solar energy gain	6649	
Energy balance	0.02%	

*This value is not physical since the ground was set to a constant temperature boundary condition

The predominant (72%) heat loss mechanism at the glazing was radiation heat loss. This is a result of the glazing's close proximity to the internal wall surface which is held at a high temperature (73^{o}C); resulting in a high degree of radiation exchange.

Simulations using RNG k-ϵ turbulence and standard k-ω yielded very similar results for both refined and coarse meshes. Since there are no known published experimental results for comparison, it can be assumed that both models are sufficiently accurate. The standard k-ω model was found to consistently reach convergence faster than the RNG k-ϵ model. This is expected as the RNG k-ϵ has a higher degree of complexity. Further research is suggested to determine experimentally which model is most accurate.

The continous flow in the convective loop acts to distribute heat more evenly in the perimeter zone, moderating the temperature stratification. Figure 6.15 shows the vertical temperature distribution in the south cavity for the case where a non-insulating partition wall is inserted into the middle of the top cavity, disrupting the continous loop. In this case, the temperature in the upper cavity reached up to 67^{o}C, compared to 57^{o}C when the complete loop was intact. Correspondingly much of the cavity not in the vicinity of the glazing was at a lower temperature, resulting in much higher levels of stratification then those shown in Figure 6.4. The maximum temperature difference was 26.4^{o}C without the partition wall and 43.3^{o}C with the partition. This result points to a critical implication for the NTED™ house. A disruption of the convective loop would result in the heat pump operating a signficantly lower COP unless the heat pump was located in the direct vicinity of the local high temperature region, i.e in the south cavity space.

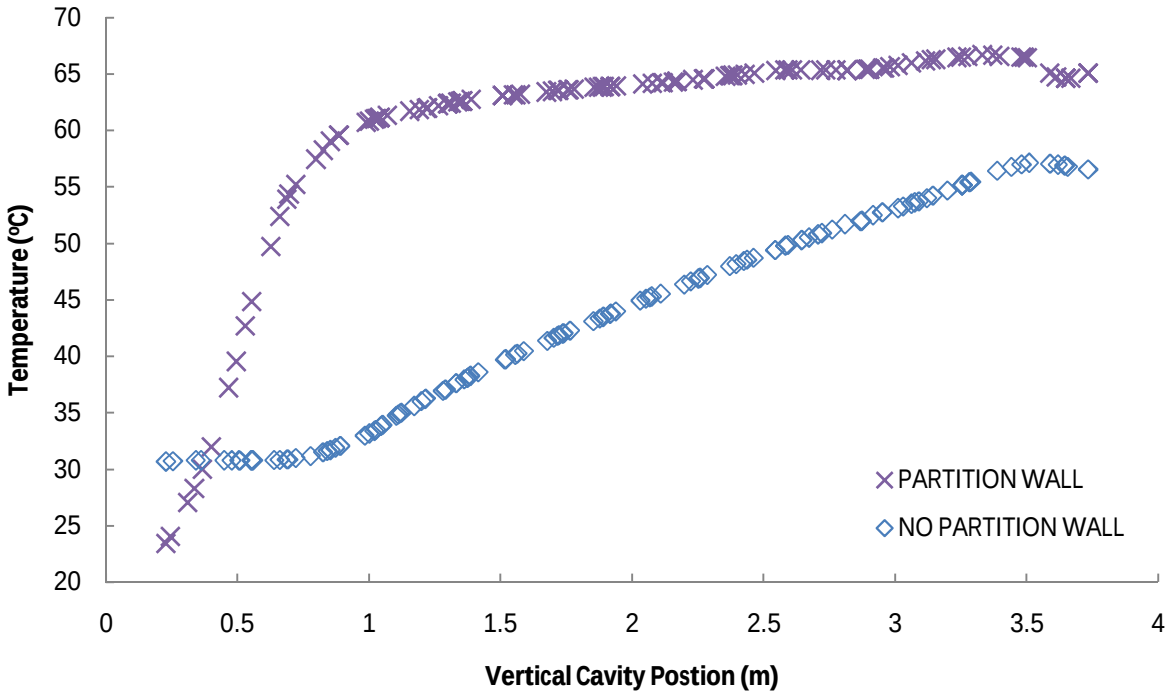

Figure 6.15 - Steady state basic geometry vertical temperature line plot with and without partition wall (y+ = 3)

Table 6.2 shows the average temperature in the domain and the total heat transfer rate through the glazing with and without a partition wall inserted in the top cavity. The partition concentrates more heat in the south cavity where it is lost more effectively through the glazing due to the non-linear fourth order temperature dependence of radiation heat transfer. The average temperature without the partition is higher since heat is distributed more evenly throughout the perimeter space and radiation heat loss is minimized. The continous flow in the convective loop acts to moderate the temperature gradients in the space. Thus the continuous loop allows for greater solar gains. The implication of this is that a convective loop design house realizes greater energy efficiency than a house with no continuous flow path.

Table 6.2 - Summary heat transfer and average temperature with and without partition wall

	Total Average Temperature (^{o}C)	Total Heat Transfer Rate through Glazing (W)
Without partition wall	42.7	-4384
With partition wall	33.2	-5040

6.3 Transient Simulations

6.3.1 Basic Geometry

The transient simulations were initialized with a steady state night simulation. Simulations were run from just before sun rise at 7:45am for approximately ten hours. The solar data was updated every minute. The transient

simulations use the coarse mesh since these simulations are very computationally expensive. As a result the solutions are expected to lack some accuracy; specifically, the temperature stratification is expected to be under predicted while the volume flow rate is expected to be over predicted (Refer to 6.23 and 6.25). Figure 6.16 shows the total average temperature in the domain over the day.

The maximum temperature reached was 31.0^{o}C after 5 hrs 3 mins (12:48pm), and was lower than the steady state result by 7.5^{o}C. The maximum temperature was reached 34 mins after the peak solar radiation (12:14pm) indicating there is a delay in the temperature rise. This implies that steady state was never entirely reached and the cumulative effects of thermal mass were influence the solution.

Figure 6.17 shows the volume flow rate through the perimeter cavity over the day. Initially there is flow in the reverse direction until the flow changes direction after approximately 30 minutes. The average daytime flow rate was 0.084m^3/s or 0.060m^3/s/m^2. The maximum volume flow rate was 0.097 m^3/s or 0.069m^3/s/m^2. The volume flow rate for the steady state case with the coarse mesh was slightly lower at 0.080m^3/s.

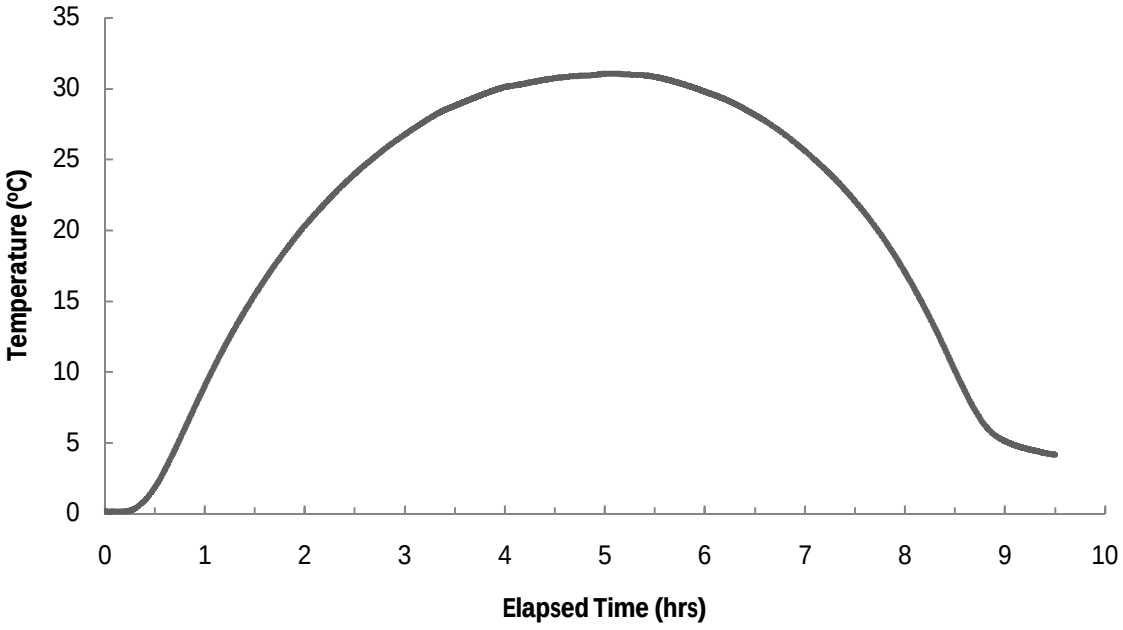

Figure 6.16 - Transient basic geometry average air temperature

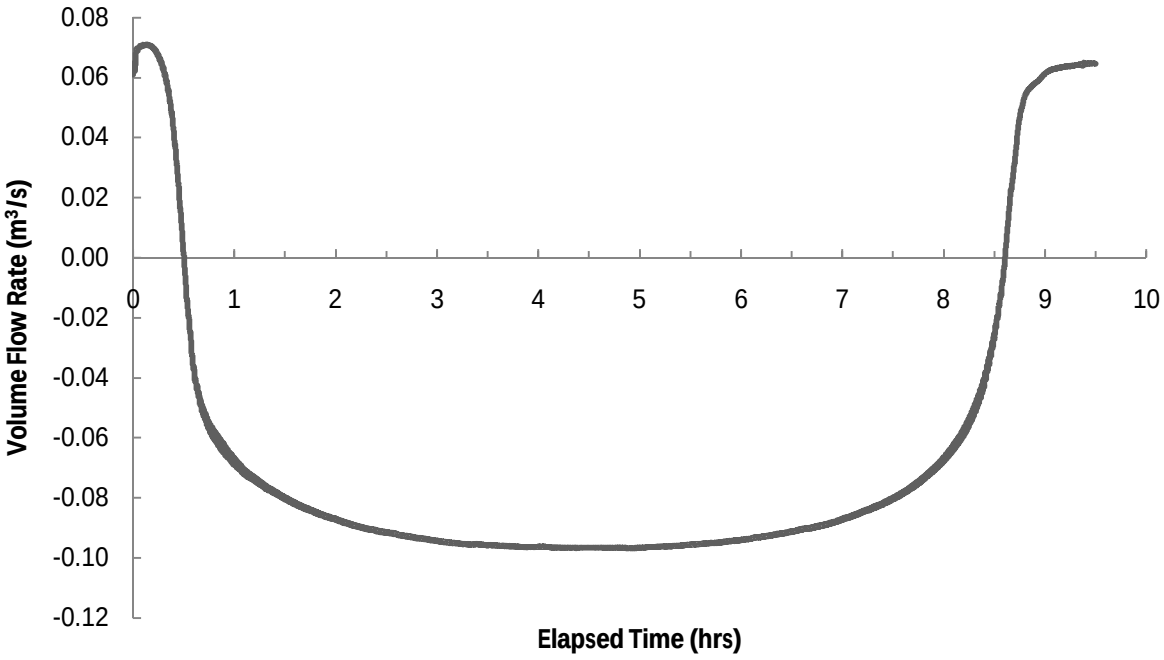

Figure 6.17 - Transient basic geometry volume flow rate

6.3.2 31 Sussex Geometry

Figure 6.18 shows the total average temperature in the domain over the day.

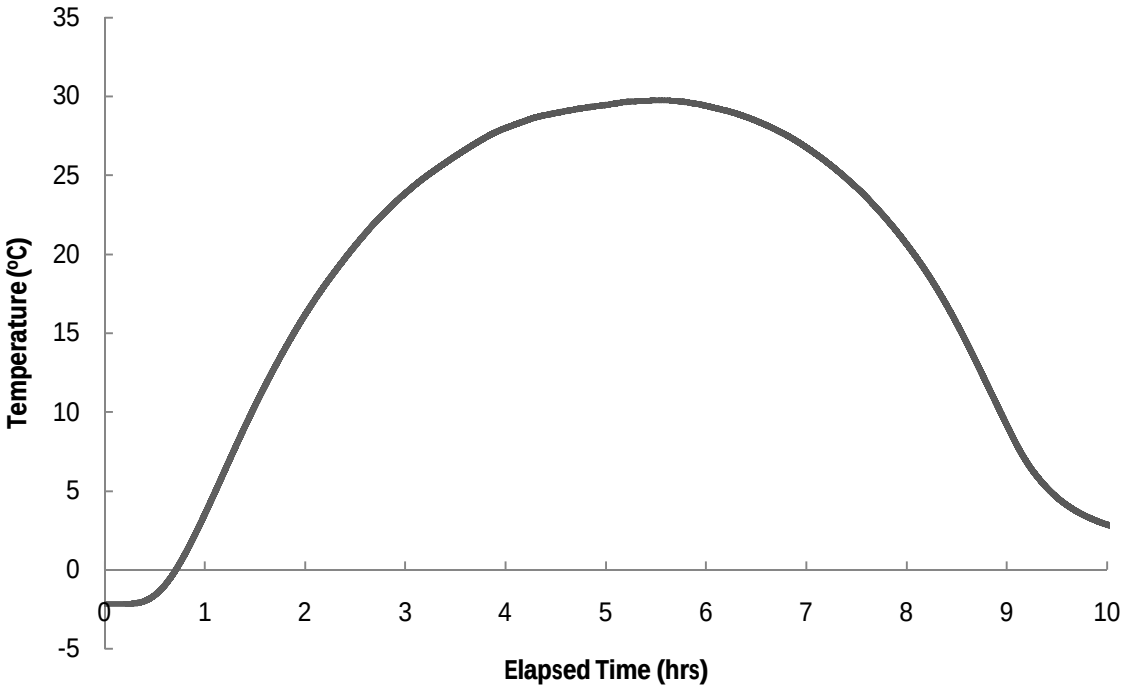

Figure 6.18 - Transient 31 Sussex geometry average temperature

The maximum temperature reached was 29.8°C after 5 hrs 32 mins (1:17pm), lower than the steady state result by 7.5°C. The maximum temperature was reached 63 mins after the peak solar radiation (12:14pm) again indicating there is a delay in the temperature rise. The delay with the 31 Sussex geometry was more substantial than with the basic geometry perhaps due to the larger amount of thermal mass.

Figure 6.19 shows the volume flow rate through the perimeter cavity over the day. The flow follows a similar trend as with the Basic geometry. The average daytime flow rate was 0.58m^3/s or 0.11m^3/s/m^2. The maximum volume flow rate was 0.68 m^3/s or 0.12m^3/s/m^2.

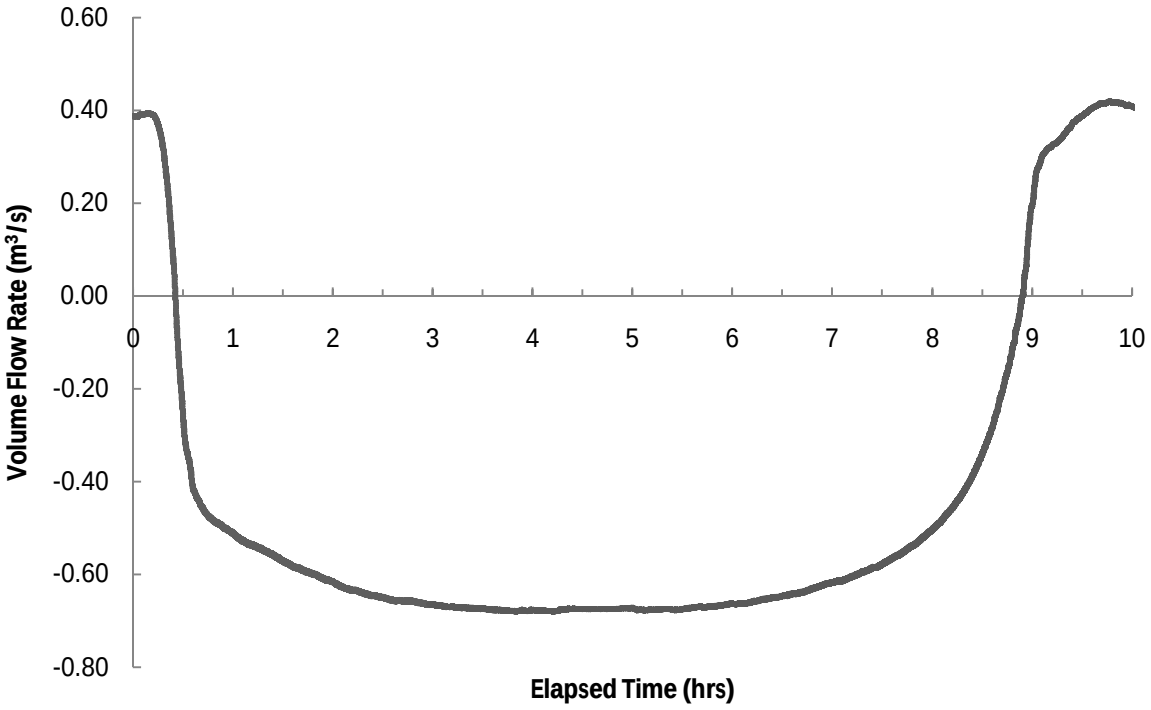

Figure 6.19 - Transient 31 Sussex geometry volume flow rate

6.3.3 Summary

Figure 6.20 shows the velocity vectors on a section in the north-south plane at 12:00pm from the transient simulations. The larger cavity width does not lead to any significant flow reversal. The maximum velocity was 0.40m/s along the south facing internal wall. The flow pattern is very similar to that of the Basic geometry, with a higher velocity flows near the walls and near stagnant flow away from the walls. Therefore the convective loop is not highly dependent on geometry.

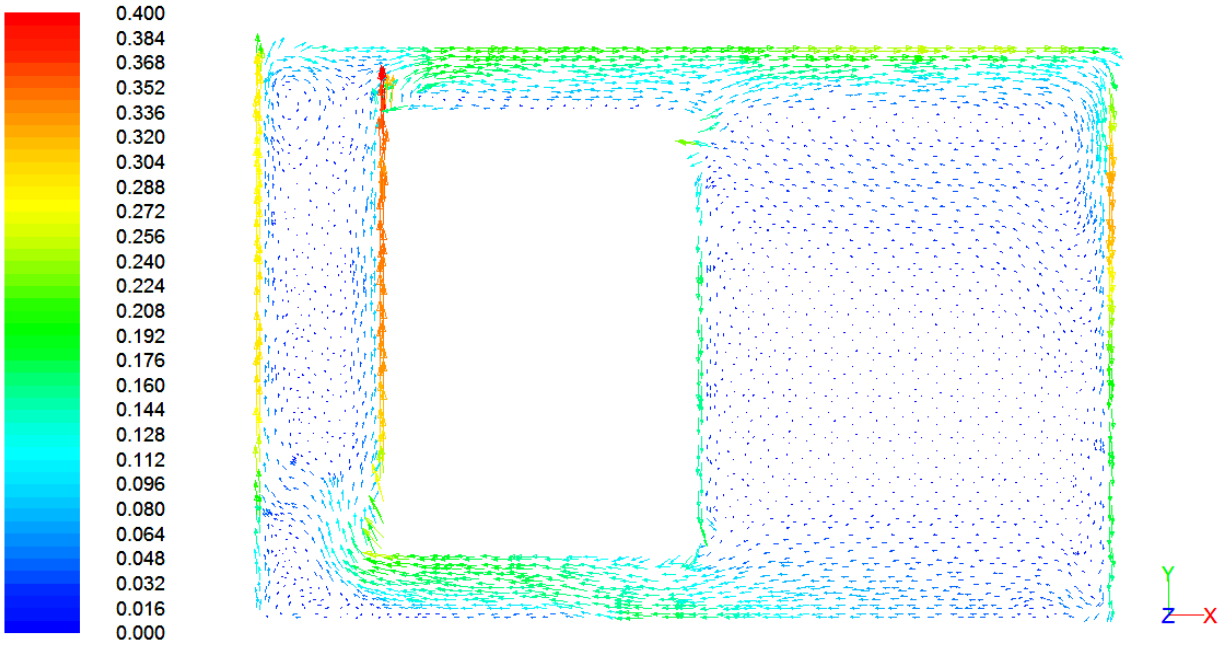

Figure 6.20 - Transient 31 Sussex geometry velocity (m/s) vectors, 12:00pm

6.4 Heat Pump Model

Simulations were run with the heat pump located in the bottom cavity and top cavity. For the bottom location, the heat pump unit was centred under the floor of the core as shown in the Figure 5.9 inset. For the top location, the heat pump was centred above the ceiling of the core. Table 6.3 summarizes the results of simulations for the two heat pump locations. In both cases, the fan was set to a fixed volume flow rate of approximately 0.3m^3/s. The reference temperature T_{ref} from Equation 65 was -10^{o}C for the model where the heat pump was located in the bottom cavity. For the model with the heat pump located in the top cavity, T_{ref} was set to 2^{o}C such that the same heat output was achieved. Figure 6.21 and 6.22 show the temperature contours for the heat pump in the top and bottom location respectively. The volume averaged temperature in the heat pump unit for the bottom and top locations was 2.0^{o}C and 13.5^{o}C corresponding to a heat output of 2408W and 2388W respectively.

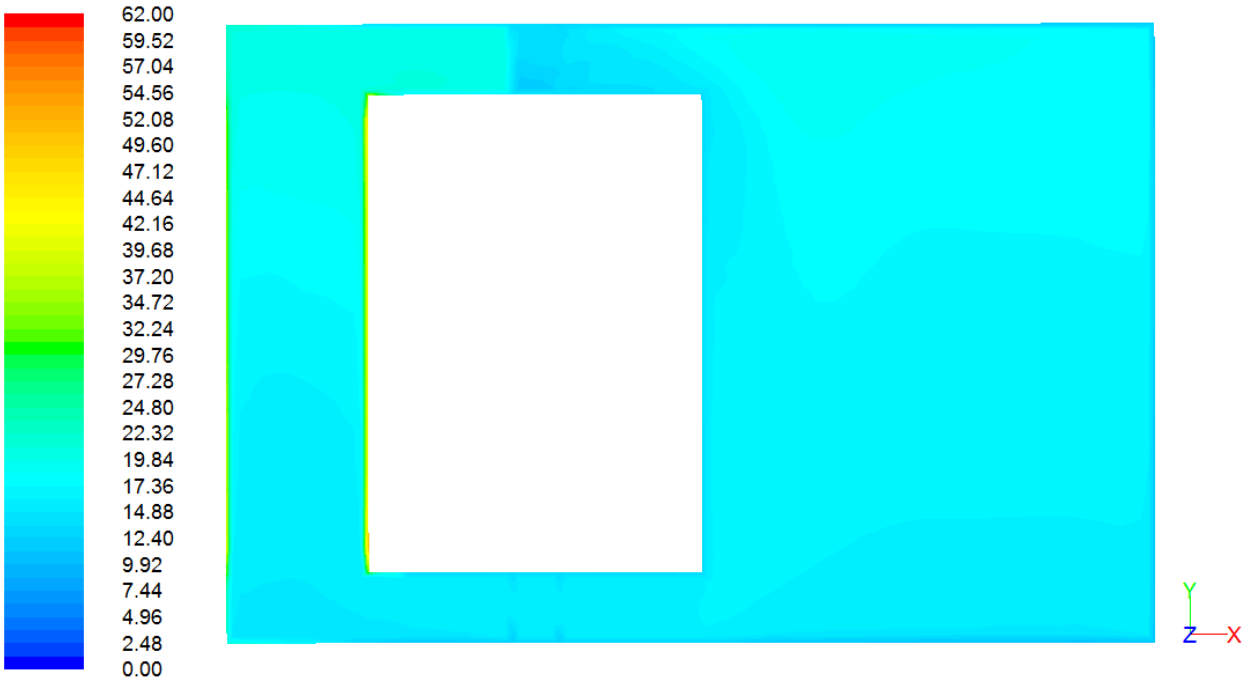

6.21 - Steady state 31 Sussex geometry temperature (^{o}C) contours for heat pump model in top location (y+ = 113)

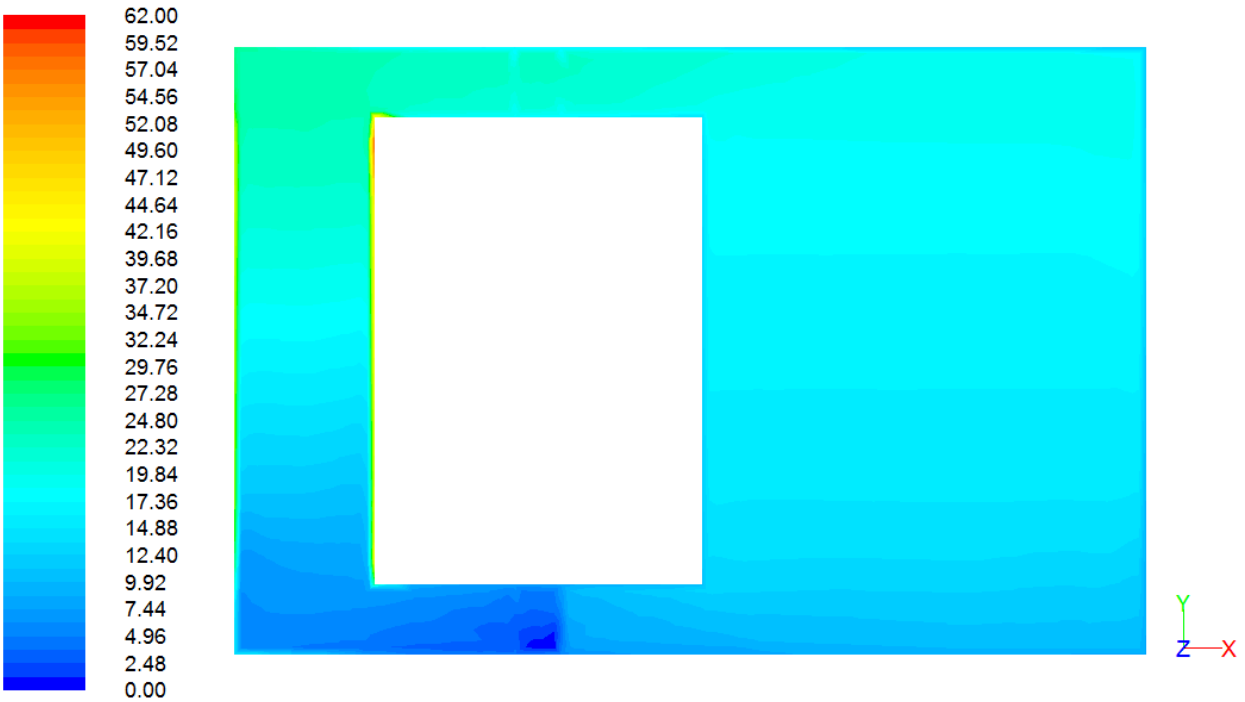

6.22 - Steady state 31 Sussex geometry temperature (^{o}C) contours for heat pump model in bottom location (y+ = 113)

Table 6.3 - Heat pump performance data summary

	Heat out (W)	Fan flow (m^3/s)	Total flow (m^3/s)	Tavg in heat pump (^oC)	Tavg total (^oC)
Bottom	2408	0.29	0.21	2.2	16.3
Top	2388	0.30	0.97	13.5	17.2

Figure 6.23 shows the temperature distribution along a line centred in the south cavity.

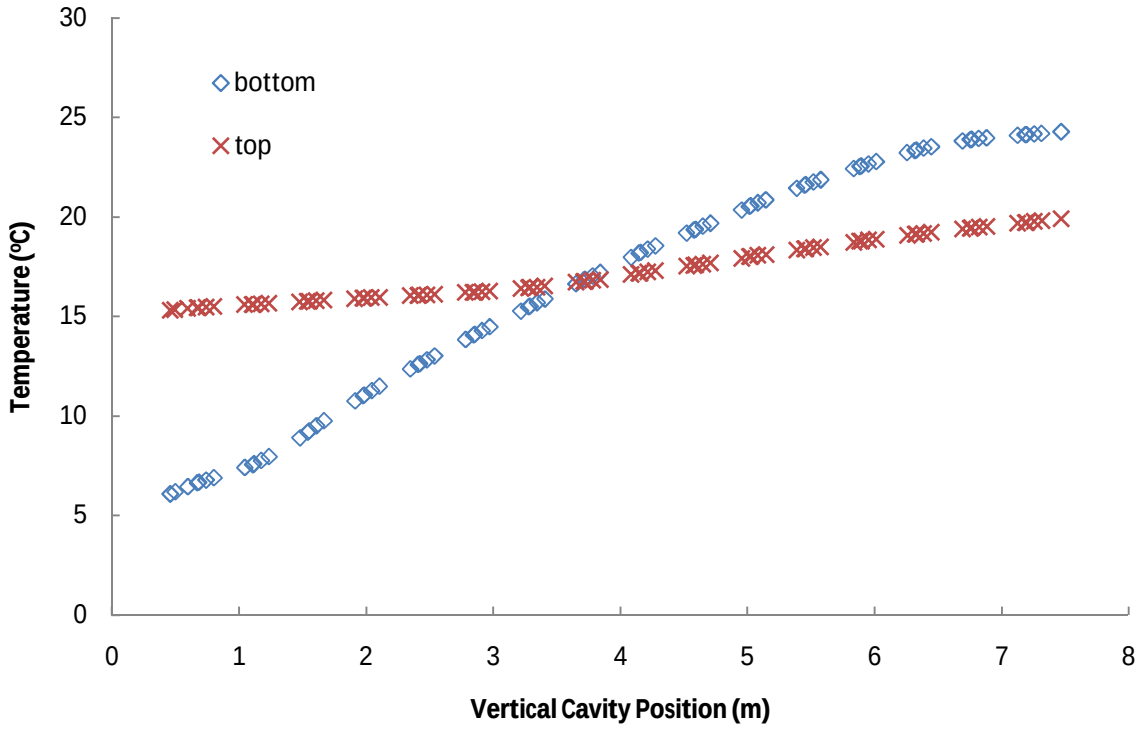

Figure 6.23 - 31 Sussex geometry vertical temperature line plot for top and bottom heat pump locations

With the heat pump located in the bottom cavity, the total volume flow rate through the perimeter is low ($0.21m^3/s$). The temperature was more stratified, with a maximum temperature difference along the vertical cavity height of 18.2^oC. Thus with the heat pump in the bottom location forced convection via fans would be required to properly moderate the temperature in the space. With the heat pump located in the top cavity, the total volume flow rate through the perimeter is significantly higher ($0.97m^3/s$) allowing heat to be more evenly distributed resulting in less temperature stratification. The maximum temperature difference along the vertical cavity height was 4.6^oC.

Figure 6.24 shows the velocity vectors for the heat pump located in the top cavity. Dense air cooled in the heat pump falls rapidly down the north core wall reaching velocities up to 0.7m/s driving the flow.

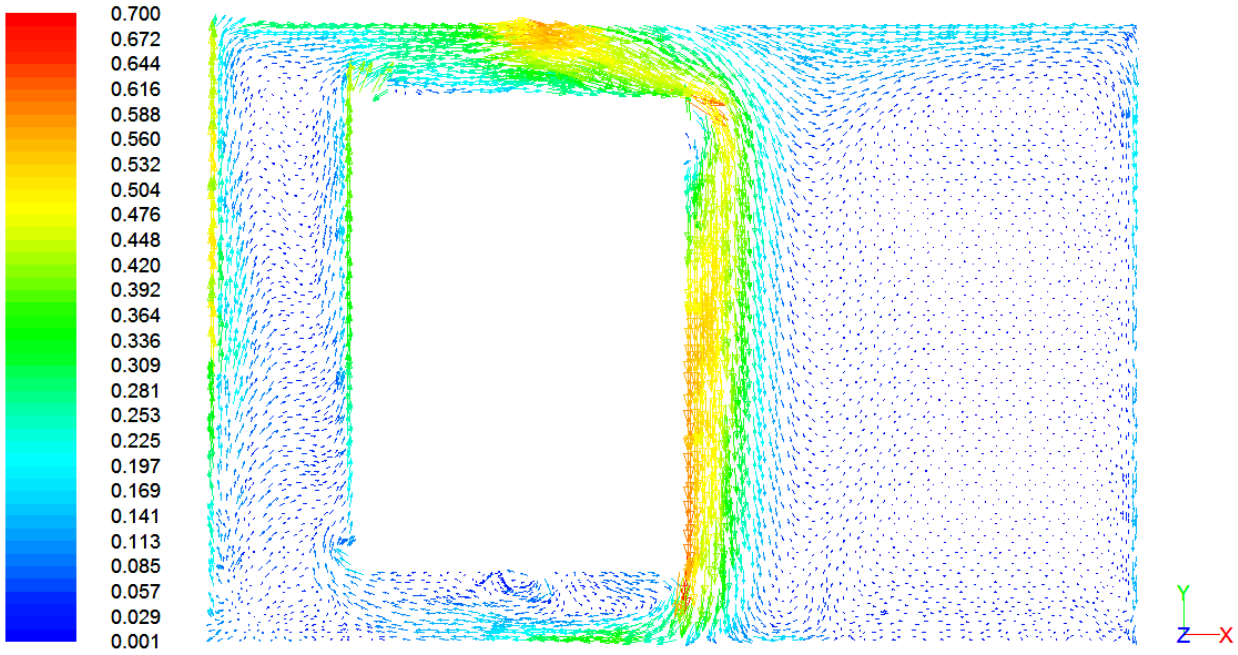

6.24 - Steady state 31 Sussex geometry velocity (m/s) vectors for heat pump model in top location (y+ = 113)

Figure 6.25 shows the temperature dependence on the COP for the Carrier 25HPA5 Performance 15 Series Heat Pump (Dixon, E., 2010). It is assumed that the Mr. Slim heat pumps would have similar temperature dependence.

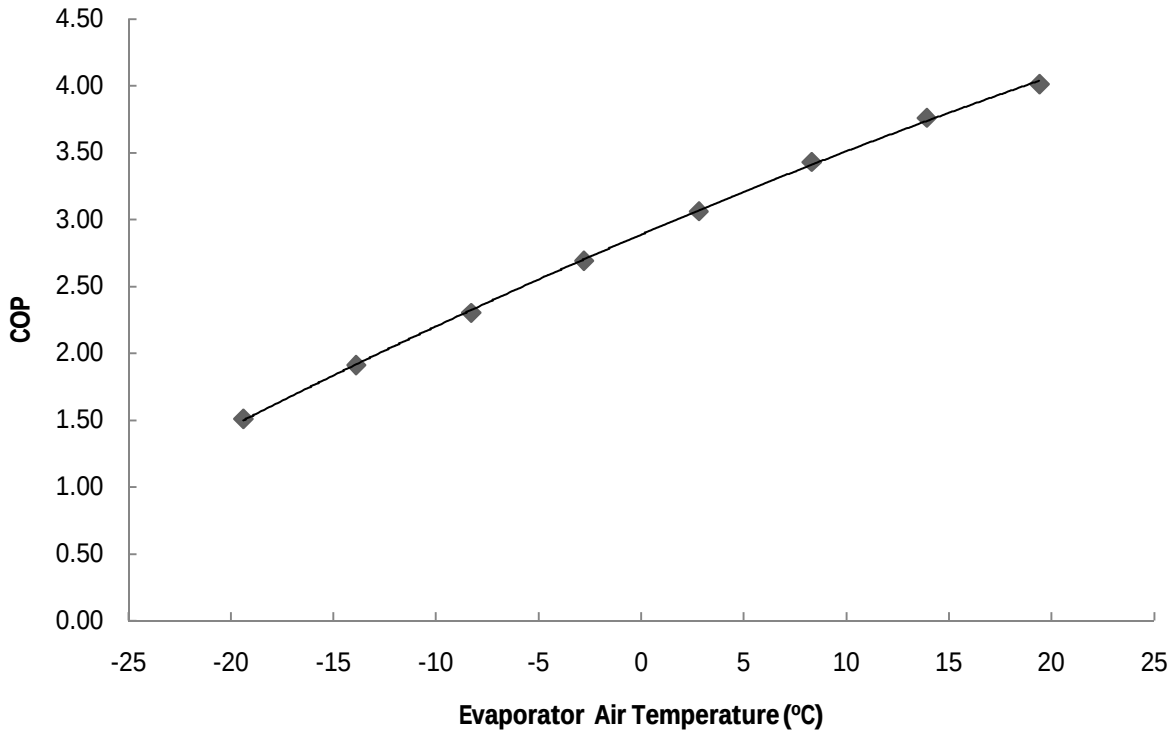

Figure 6.25 - Heat pump COP dependence on temperature

A polynomial regression was performed to determine the relationship between COP and temperature to be

$$COP = -0.00317T^2 + 0.0654T + 2.89$$

For evaporator air temperatures of 2°C and 13.5°C, the COP is 3.02 and 3.33 respectively. Therefore, based on the performance of this heat pump, a temperature difference of 11.5°C will affect the COP by approximately 21%. Therefore, positioning the heat pump in the top location leads to significant energy savings over the bottom location, enhancing the overall performance of the NTED™ house.

Clearly, temperature stratification has more immediate effects than energy savings, i.e. occupant thermal comfort. Occupant comfort played a significant role in the judging the performance of past double envelope houses including the Mastin House (Jones et al., 1982). Large temperature swings through the elevation of a house not only affect occupant comfort, but may also have energy consequences if they lead to a change in occupant behaviour, such as opening windows or using auxiliary heating devices. All these factors will significantly affect how the NTED™ is accepted by the general public.

7 Conclusions

A model of a convective loop in the NTED™ low energy house was created using commercial CFD software. A complete review of experimental and simulation studies on double envelope houses and prior work on the NTED™ was presented. A literature review of CFD simulation studies on air flow in cavities, solar chimneys, double skin facades, and atria provided insight into model selection and mesh considerations. A grid independence study on a simplified "Basic" geometry was performed to verify the models accuracy. A refined mesh was necessary for a grid independent solution. Simulations using the coarse mesh resulted in an over prediction of volume flow rates and correspondingly a lower degree of temperature stratification. Results using the coarse mesh also resulted in lower average temperatures in the domain. However, simulations using the coarse mesh provided a relatively accurate approximation, capturing the important flow features and temperature distributions. This was important since all transient simulations were performed using coarse meshes due to computational restraints.

Steady state simulations were performed on the Basic geometry analyzing the convective loop behaviour during the night and day time operation in Toronto, ON for the heating season. Buoyancy driven flow in the convective loop allowed solar gains to be effectively distributed around the perimeter space. The performance of the convective loop was assessed by determining the volume flow rates and temperature stratification in the space. The maximum volume flow rate was $0.049 m^3/s$ or $0.035 m^3/s/m^2$ with a maximum velocity of 0.37m/s. The maximum temperature difference through the height of the loop was 26.4^oC. Night time simulations resulted in a flow in a reverse direction and of a magnitude 75% less than that in the forward direction during peak solar irradiation.

The convective loop acted to moderate the temperature distribution in the perimeter, reducing stratification. Disrupting the convective loop with an internal partition wall led to dramatically higher levels of temperature stratification and led to a higher degree of overall heat loss due to the non-linearity of radiation heat transfer. The maximum temperature difference without the partition wall was 43.3^oC, 64% greater than with a complete uninterrupted loop.

Transient simulations were performed to assess natural convective flow over the entire day. Transient simulations illustrated a time delay in temperature rise as a result of the thermal diffusivity of the building materials. The maximum average temperature occurred over 30 minutes after the time of peak solar irradiation. Furthermore, the maximum average temperature reached was approximately 8^oC less than the average temperature found for steady state results at the maximum irradiation level. This indicates that a steady state never truly occurred, and thus transient simulations were required for accurate results.

The model was applied to the "31 Sussex" geometry representing the NTED™ low energy house. Transient simulations were performed on the 31 Sussex geometry to assess the convective loops performance over the entire day. The Basic and 31 Sussex geometries were found to have very similar flow regimes and temperature

profiles despite their significant difference in scale and dimension. In both cases, little flow reversal or circulation was apparent. The maximum volume flow rate was 0.68 m^3/s or 0.12$m^3/s/m^2$. The larger flow rate was due to the larger glazing area relative to the convective loop channel area.

A simplified heat pump model was created and applied to the 31 Sussex geometry to determine how its operation affects the heat distribution in the perimeter space of the NTED™ low energy house. In order to optimize heat recovery from the perimeter space and minimize temperature stratification, two models with different heat pump locations were compared. Simulations were run with the heat pump located in the top and bottom cavity of the convective loop. The top cavity location was found to be most effective for the NTED™ house. The volume flow rate was approximately 5 times greater, leading to more even heat distribution and less temperature stratification. The maximum temperature difference through the height of the building for the bottom and top heat pump locations was 18.2^oC and 4.6^oC respectively. Thus with the heat pump in the bottom location, forced convection via fans would be required to properly moderate the temperature in the space. Locating the heat pump in the top location allowed the heat pump to extract heat from the air at a temperature 13.5^oC higher. As a result, it is expected the heat pump could operate at a COP of 21% greater than with the heat pump located in the bottom cavity.

8 Limitations and Future Research

The major limitation of this work follows from the use of the highly simplified Basic and 31 Sussex geometries. The convective loop would behave much differently for more complex geometries. Simulations do however indicate that the flow regime is located very near to the boundary surfaces. Thus any complex geometry located away from the walls would not likely affect the flow in a significant manner as long as a complete closed loop with limited disruptions was present near the wall surfaces.

The heat pump model was highly simplified. The pressure drop through the heat pump should be accounted for using empirical data in future studies. The heat exchanger was modelled as a single surface using the Radiator boundary condition which resulted in uniform heat transfer over the surface. ANSYS Fluent also offers more advanced 3D heat exchanger models which could be applied in future studies. The Macro Heat Exchanger Model is requires a fluid domain divided into macro cells to represent an auxiliary fluid path which can be in a serpentine or parallel pass geometry. A more detailed heat exchange model termed the Dual Cell Model is available where the primary and auxiliary flow are solved on separate co-located meshes which are coupled to allow for heat transfer. Ideally, technical drawings of the heat pump in AutoCAD could be exported to ANSYS ICEM CFD where a solid mesh could be applied to the important components. ANSYS Fluent also provides a more detailed fan model based on an empirical fan curves which includes the effects of swirl (see ANSYS Theory Guide, 2009).

The heat pump output was based on a simple 1D heat load calculation for the core space. A more accurate method would involve meshing the core space and adjusting the heat output to achieve a 21^{o}C core set point. Furthermore, the heat output would vary over the day as the boundary conditions change, thus a transient simulation would be required using user defined function (UDF's) to specify the output over time. Applying the heat pump model to a transient simulation would provide more valuable results towards optimizing heat recovery and is an area for future research.

A full investigation on the potential for forced convection in the NTED™ house is an area for future research. Forced convection via fans functions to distribute heat more effectively in the convective loop at the expense of fan power. The use of forced convection via fans is a relatively simple means for moderating temperature in the convective loop. Although a fan is always present in a heat pump assembly, multiple fans carefully placed around the perimeter could provide the necessary air flow if natural convection is found to be insufficient. However, fan power consumption will reduce overall energy performance. A further study into the fan power necessary to optimize the heat pump output and achieve the desired degree of temperature stratification in the space would be valuable.

Finally, the model should be validated against similar experimental benchmark problems as is often done in the literature for CFD simulations. The effects of air infiltration through the building envelope were not included in the model and should be studied further

9 Appendices

9.1 Simulation Data

9.1.1 Solar load data

Table 9.1 – Basic geometry solar load data for Dec 21 12:00pm, Toronto, ON

```
Fair Weather Conditions:
  Sun Direction Vector:  X: -0.915161, Y: 0.399037, Z: 0.057009
  Sunshine Fraction: 1
  Direct Normal Solar Irradiation (at Earth's surface) [W/m^2]: 863.806
  Diffuse Solar Irradiation - vertical surface: [W/m^2]: 59.7668
  Diffuse Solar Irradiation - horizontal surface [W/m^2]: 49.2369
  Ground Reflected Solar Irradiation - vertical surface [W/m^2]: 39.3927
Internally Scattered Energy [W]: 780.49, Ambient Flux [W/m^2]: 41.9825
Boundary ID: 18, Integral Energy Source [W]: 1.980816e+003
Boundary ID: 70076, Integral Energy Source [W]: 4.668267e+003
Total Integral Energy Source [W]: 6.649084e+003
Compute Time:  0 sec
Done.
```

Table 9.2 - 31 Sussex geometry solar load data for Dec 21, 12:00pm, Toronto, ON

```
Fair Weather Conditions:
  Sun Direction Vector:  X: -0.915161, Y: 0.399037, Z: 0.057009
  Sunshine Fraction: 1
  Direct Normal Solar Irradiation (at Earth's surface) [W/m^2]: 863.806
  Diffuse Solar Irradiation - vertical surface: [W/m^2]: 59.7668
  Diffuse Solar Irradiation - horizontal surface [W/m^2]: 49.2369
  Ground Reflected Solar Irradiation - vertical surface [W/m^2]: 39.3927
Internally Scattered Energy [W]: 3152, Ambient Flux [W/m^2]: 42.4098
Boundary ID: 18, Integral Energy Source [W]: 7.930433e+003
Boundary ID: 70076, Integral Energy Source [W]: 1.936924e+004
Total Integral Energy Source [W]: 2.729968e+004
Compute Time:  0 sec
```

Table 9.3 - 31 Sussex solar load data averaged over the day of Dec 21, Toronto, ON

```
Internally Scattered Energy [W]: 2041.7, Ambient Flux [W/m^2]: 26.8664
Boundary ID: 18, Integral Energy Source [W]: 4.836022e+003
Boundary ID: 70076, Integral Energy Source [W]: 1.141074e+004
Boundary ID: 80093, Integral Energy Source [W]: 2.246374e+001
Boundary ID: 80094, Integral Energy Source [W]: 2.246374e+001
Total Integral Energy Source [W]: 1.629169e+004
Compute Time:  0 sec
```

9.1.2 Total heat flux data

Table 9.4 - Basic geometry night simulation fluxes, y+ = 46, RNG

Total Heat Transfer Rate	(w)	Radiation Heat Transfer Rate	(w)
eastwall	-14.11022	eastwall	-6.6807856
floor	139.09868	floor	107.72411
ground	-18.600422	ground	-52.249554
insidewall	238.92603	insidewall	174.9861
northwall	-46.19524	northwall	-60.220662
roof	-59.780584	roof	-59.896391
south_insidewall	137.30769	south_insidewall	189.64236
southwall_bottom	-2.5543587	southwall_bottom	-1.2598876
southwall_middle	-357.85316	southwall_middle	-285.21697
southwall_top	-3.3665725	southwall_top	0.64625964
westwall	-14.065809	westwall	-7.1103519
Net	-1.1939778	Net	0.36423847

Table 9.5 - Basic geometry day simulation fluxes, y+ = 46, RNG

Total Heat Transfer Rate	(w)	Radiation Heat Transfer Rate	(w)
eastwall	-165.72028	eastwall	-58.62695
floor	-26.567369	floor	215.18107
ground	-445.43198	ground	-352.94836
insidewall	-164.08173	insidewall	98.091108
northwall	-268.49657	northwall	-24.859922
roof	-397.53468	roof	-52.047408
south_insidewall	-330.06375	south_insidewall	3569.8088
southwall_bottom	-35.897163	southwall_bottom	-43.719825
southwall_middle	-4603.1634	southwall_middle	-3245.3051
southwall_top	-46.405177	southwall_top	-47.194666
westwall	-164.8587	westwall	-58.49699
Net	-6648.2208	Net	-0.11821826

Table 9.6 - Basic geometry day simulation fluxes, y+ = 6, RNG

Total Heat Transfer Rate	(w)	Radiation Heat Transfer Rate	(w)
eastwall	-185.93198	eastwall	0.22678988
floor	-34.292597	floor	263.88114
ground	-445.19275	ground	-426.25243
insidewall	-251.12082	insidewall	45.918903
northwall	-319.65796	northwall	-15.342551
roof	-465.92323	roof	12.994781
south_insidewall	-306.41071	south_insidewall	3294.4152
southwall_bottom	-32.233734	southwall_bottom	-37.553329
southwall_middle	-4368.9133	southwall_middle	-3130.8121
southwall_top	-53.69316	southwall_top	-10.344147
westwall	-186.01682	westwall	2.77644
Net	-6649.387	Net	-0.091315876

Table 9.7 - Basic geometry day simulation fluxes, y+ = 3, RNG

Total Heat Transfer Rate	(w)
eastwall	-183.91477
floor	-31.747661
ground	-462.07547
insidewall	-244.34523
northwall	-306.57346
roof	-458.66071
south_insidewall	-308.6827
southwall_bottom	-32.698992
southwall_middle	-4384.2672
southwall_top	-53.207124
westwall	-183.36219
Net	-6649.5355

Radiation Heat Transfer Rate	(w)
eastwall	-5.4880909
floor	182.35949
ground	-332.98197
insidewall	134.41436
northwall	-22.180571
roof	-73.84571
south_insidewall	3327.575
southwall_bottom	-39.184127
southwall_middle	-3149.7014
southwall_top	-16.367711
westwall	-4.6669567
Net	-0.067770635

Table 9.8 - Basic geometry day simulation fluxes, y+ = 46, SKW

Total Heat Transfer Rate	(w)
eastwall	-168.68574
floor	-35.184103
ground	-479.5925
insidewall	-177.14154
northwall	-276.2535
roof	-401.60183
south_insidewall	-324.22075
southwall_bottom	-36.144394
southwall_middle	-4534.502
southwall_top	-47.009179
westwall	-168.47381
Net	-6648.8093

Radiation Heat Transfer Rate	(w)
eastwall	-56.538615
floor	177.59163
ground	-302.96466
insidewall	136.27163
northwall	-27.510919
roof	-80.760223
south_insidewall	3500.2536
southwall_bottom	-43.211272
southwall_middle	-3202.6391
southwall_top	-44.330266
westwall	-55.946365
Net	0.21544232

Table 9.9 - Basic geometry day simulation fluxes, y+ = 3, SKW

Total Heat Transfer Rate	(w)
eastwall	-183.91477
floor	-31.747661
ground	-462.07547
insidewall	-244.34523
northwall	-306.57346
roof	-458.66071
south_insidewall	-308.6827
southwall_bottom	-32.698992
southwall_middle	-4384.2672
southwall_top	-53.207124
westwall	-183.36219
Net	-6649.5355

Radiation Heat Transfer Rate	(w)
eastwall	-5.4880909
floor	182.35949
ground	-332.98197
insidewall	134.41436
northwall	-22.180571
roof	-73.84571
south_insidewall	3327.575
southwall_bottom	-39.184127
southwall_middle	-3149.7014
southwall_top	-16.367711
westwall	-4.6669567
Net	-0.067770635

Table 9.10 - Basic geometry with partition day simulation fluxes, y+ = 3, SKW

Total Heat Transfer Rate	(w)
eastwall	-146.79721
floor	27.06061
ground	-311.34601
insidewall	-56.407369
northwall	-131.58367
partition	187.20524
partition-shadow	-187.78154
roof	-387.24829
south_insidewall	-352.28525
southwall_bottom	-32.63657
southwall_middle	-5040.327
southwall_top	-58.678006
westwall	-142.46357
Net	-6633.2886

Radiation Heat Transfer Rate	(w)
eastwall	-3.4106135
floor	177.71778
ground	-281.28584
insidewall	43.175173
northwall	-62.629075
partition	114.85085
partition-shadow	-65.064077
roof	3.3132736
south_insidewall	3721.1208
southwall_bottom	-64.794144
southwall_middle	-3558.6146
southwall_top	-18.364034
westwall	-8.8006436
Net	-2.7851376

*Heat pump simulations were run with the average daily irradiation level shown in Table 10.10. Simulations performed with heat pump in top and bottom locations of 31 Sussex geometry.

Table 9.11 - 31 Sussex geometry top heat pump location simulation fluxes, y+ = 113, SKW

Total Heat Transfer Rate	(w)
eastwall	-805.73747
floor	115.17745
floor:003	2.4811017
ground	-1101.1296
ground:001	-8.4768967
heatpump2	-2388.2517
insidewall	226.65193
insidewall:004	2.3604152
northwall	-530.10378
roof	-886.73269
roof:002	-6.5056891
south_insidewall	-560.83122
southwall_bottom	-95.413201
southwall_middle	-9333.0222
southwall_top	-98.531834
westwall	-805.71772
Net	-16273.783

Radiation Heat Transfer Rate	(w)
eastwall	-307.83613
floor	237.48063
floor:003	4.1128098
ground	-777.98857
ground:001	-3.8217131
heatpump2	0
insidewall	567.82206
insidewall:004	-1.5429855
northwall	-26.563388
roof	-198.64578
roof:002	-4.4600844
south_insidewall	7381.6775
southwall_bottom	-143.00677
southwall_middle	-6311.4002
southwall_top	-127.20941
westwall	-305.86034
Net	-17.242293

Table 9.12 – 31 Sussex geometry, bottom heat pump location simulation fluxes, y+ = 113, SKW

Total Heat Transfer Rate	(w)
eastwall	-762.44466
floor	184.70453
floor:003	5.0134451
ground	-778.3397
ground:001	-2.3674657
heatpump	-2468.4007
insidewall	235.82256
insidewall:004	1.0207409
northwall	-490.38934
roof	-926.84431
roof:002	-7.8192803
south_insidewall	-608.5305
southwall_bottom	-75.316338
southwall_middle	-9686.9614
southwall_top	-110.04999
westwall	-762.48374
Net	-16253.386

Radiation Heat Transfer Rate	(w)
eastwall	-370.26211
floor	255.28843
floor:003	1.0733269
ground	-992.59584
ground:001	-10.263348
heatpump	0
insidewall	537.47626
insidewall:004	3.1713408
northwall	-50.568907
roof	-53.27761
roof:002	-1.149596
south_insidewall	7830.2903
southwall_bottom	-204.74635
southwall_middle	-6447.0258
southwall_top	-122.79971
westwall	-364.98349
Net	9.6268967

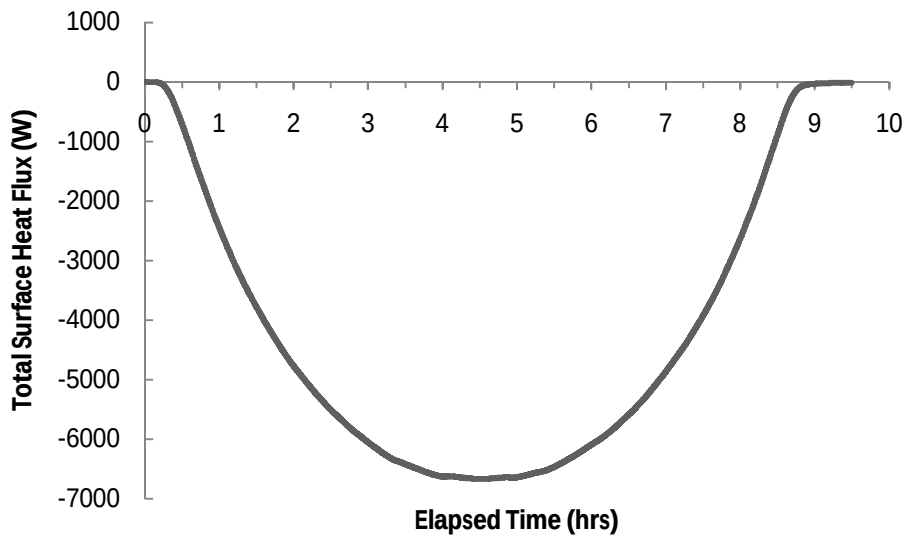

Figure 9.1 - Basic geometry transient simulation total heat flux, y+ = 46, SKW

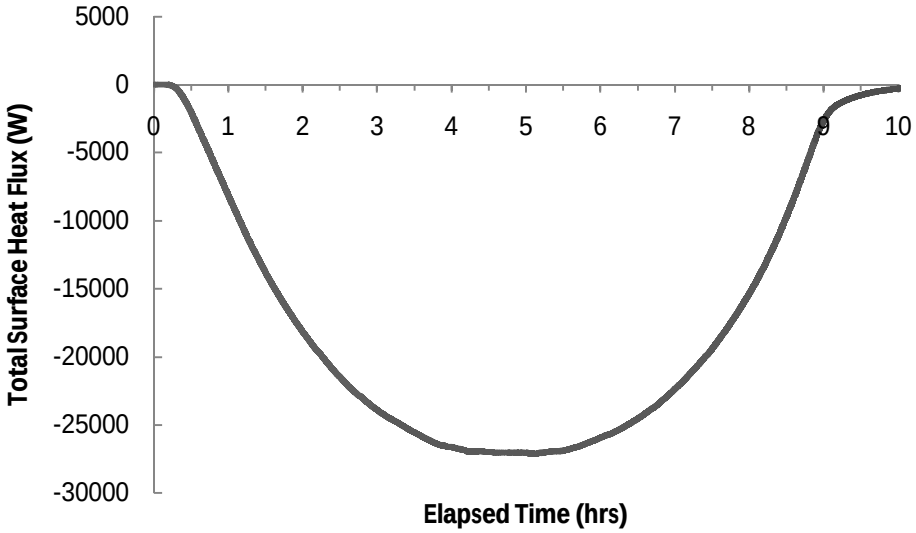

Figure 9.2 - 31 Sussex geometry transient simulation total heat flux, y+ = 132, SKW

9.2 31 Sussex Drawings

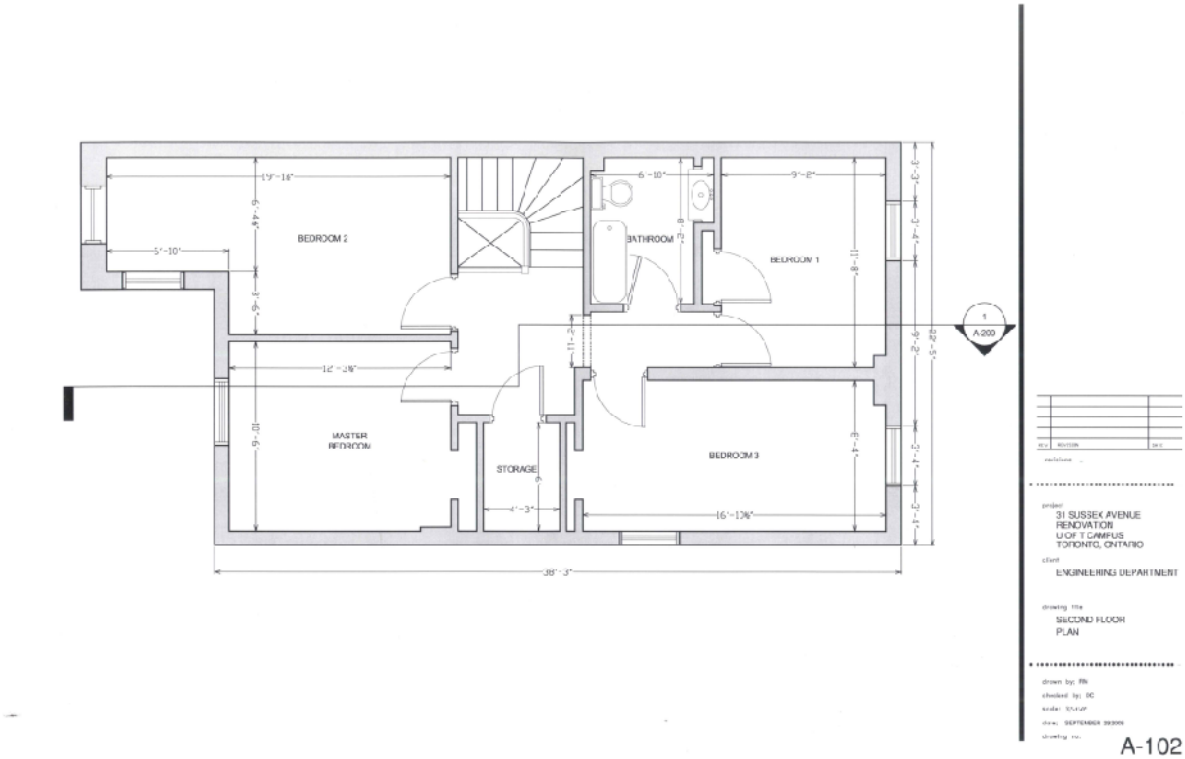

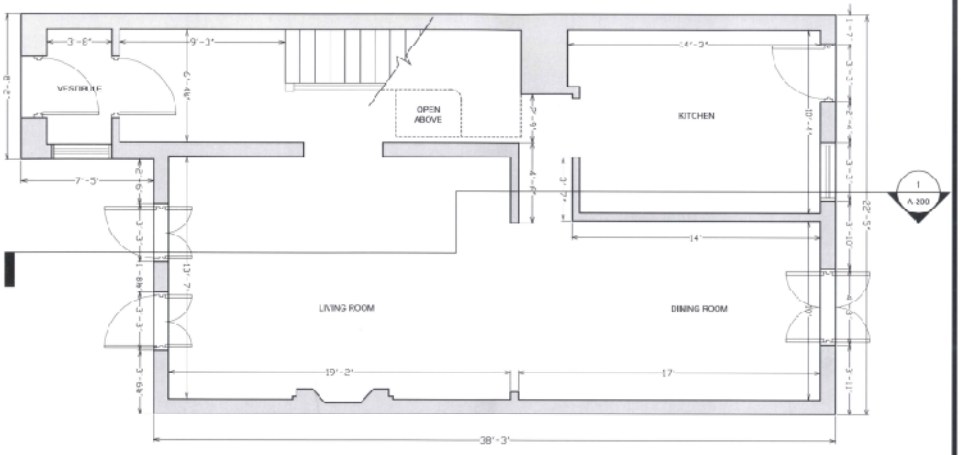

REV	REVISION	DATE

revisions -

project
31 SUSSEX AVENUE
RENOVATION
U OF T CAMPUS
TORONTO, ONTARIO

client
ENGINEERING DEPARTMENT

drawing title
GROUND FLOOR
PLAN

drawn by: RM
checked by: DC
scale: 1/4"=1'-0"
date: SEPTEMBER 29 2009
drawing no.

A-101

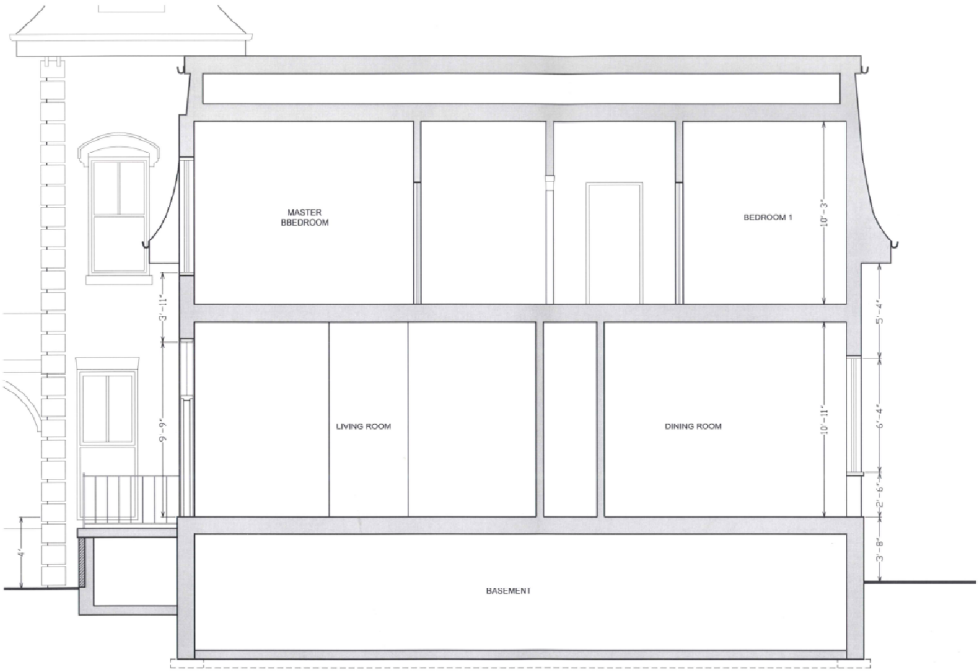

1 **SECTION**
Scale: 1/4" = 1'-0"

REV	REVISION	DATE

revisions -

project
31 SUSSEX AVENUE
RENOVATION
U OF T CAMPUS
TORONTO, ONTARIO

client
ENGINEERING DEPARTMENT

drawing title
NORTH SOUTH
SECTION

drawn by: RM
checked by: DC
scale: 1/4"=1'-0"
date: SEPTEMBER 09 2009
drawing no.

A-200

10 References

ASHRAE (2009). American Society of Heating, Refrigerating and Air-Conditioning Engineers. *2009 ASHRAE handbook: fundamentals SI.* Atlanta, GA: American Society of Heating, Refrigerating and Air-Conditioning Engineers, Inc.

ANSYS Fluent 12.0 Theory Guide, (2009) ANSYS Inc.

ANSYS Fluent 12.0 User Guide, (2009) ANSYS Inc.

ANSYS Fluent 12.0 Tutorial Guide, (2009) ANSYS Inc.

Allen, B. M., & Ribando, R. J. (1983). Computational analysis of a double-shell solar house. *Energy, 8*(11), 871-881.

Behr, R. A. (1995). On-site investigations of spandrel glass microenvironments. *Building and Environment, 30*(1), 61-72

Chen, B., Maloney, J., Wang, T. C., & Demmel, D. (1981). PERFORMANCE RESULTS OF THE DENNIS DEMMEL 'DOUBLE SHELL' HOME, HARTINGTON, NEBRASKA. 59-63. *Proceedings of the 6th national passive solar conference, September 8-12, 1981, Portland, Oregon* (1981). In Hayes J., Kolar W. A. and International Solar Energy Society. American Section.

Coussirat, M., Guardo, A., Jou, E., Egusquiza, E., Cuerva, E., & Alavedra, P. (2008). Performance and influence of numerical sub-models on the CFD simulation of free and forced convection in double-glazed ventilated façades. *Energy and Buildings, 40*(10), 1781-1789.

Gan, G. (1998). Prediction of turbulent buoyant flow using an RNG k-ε model. *Numerical Heat Transfer; Part A: Applications, 33*(2), 169-189.

Gan, G. (2006). Simulation of buoyancy-induced flow in open cavities for natural ventilation. *Energy and Buildings, 38*(5), 410-420.

Gan, G. (2010). Simulation of buoyancy-driven natural ventilation of buildings - impact of computational domain. *Energy and Buildings, 42*(8), 1290-1300.

Dixon, E., Pressnail, K., Richman, R. & Touchie, M. (2010). Thermal Performance of the Exterior Envelopes of Whole Buildings XI International Conference: *NTED: An innovative design using nested thermal envelopes to achieve significant reductions in energy use.*

Dixon, E. (2010). M.A.Sc. Thesis. Ryerson University, Department of Architectural Science. “Energy Model Development and Heating Energy Investigation of the Nested Thermal Envelope Design (NTED™)”

Ghaffari, H. T., & Jones, R. J. (1981). GROUND COUPLING AND SINGLE-BLOW THERMAL STORAGE IN A DOUBLE-ENVELOPE HOUSE. , *4* .(1) 530-534.

Goethals, K., Janssens, A., (2009), SENSITIVITY ANALYSIS OF PREDICTED CONVECTIVE HEAT TRANSFER AT INTERNAL BUILDING SURFACES TO DIFFUSER MODELLING IN CFD. Eleventh International IBPSA Conference. Glasgow, Scotland. July 27-30, 2009

Hastings, R., Mørck, O., & International Energy Agency. Solar Heating and Cooling Programme. (2000). *Solar air systems: A design handbook*. London: James & James.

Hutcheon, N. B. (1989). In Handegord G. O. P. (Ed.), *Building science for a cold climate* (SI metric ed.). Fredericton, N.B.: Construction Technology Centre Atlantic

Hsu, Z. H., Hopkins, D. C., & Chiang, C. W. (1981). STUDY OF A DOUBLE-SHELL SOLAR HOUSE WITH NATURAL AND FORCED CONVECTION. , *4* .(2) 1052-1055.

Jones, R. F., & Dennehy, G. (1982). MASTIN DOUBLE-ENVELOPE HOUSE: A THERMAL PERFORMANCE EVALUATION. *Passive Solar Journal, 1*(3), 151-173.

National Climate Data and Information Archive. 2010. Environment Canada. Accessed July 1st 2011. http://www.climate.weatheroffice.gc.ca

Ontario Building Code (OBC). 2006. *Ontario building code 2006: Containing the building code act and O. Reg. 350/06 amended to). Reg 205/08.* Toronto, ON: Queen's Printer for Ontario.

Mr. Slim M-Series Specifications. 2011. Mitsubishi Electric Sales Canada Inc. Accessed July 1st 2011. http://www.mitsubishielectric.ca/en/hvac/m-series/specifications.html

Passive Systems Division. (Eds.), Newark, DE: Publication Office, American Section, International Solar Energy Society.

Pressnail, K.D., Richman, R., Kirsch, A.M. (2008). 12th Canadian Conference on Building Science and Technology, Montreal, QC, 2009: *An innovate approach to low-energy building performance using nested thermal envelopes.*

Reno, V. (1980). THERMODYNAMICS AND FLUID DYNAMICS OF THE DOUBLE SHELL (ENVELOPE) HOUSE. , *5* 513-517.

Rundle, C. A., Lightstone, M. F., Oosthuizen, P., Karava, P., & Mouriki, E. (2011). Validation of computational fluid dynamics simulations for atria geometries. *Building and Environment, 46*(7), 1343-1353

The Engineering Toolbox. Accessed July 1st 2011. http://www.engineeringtoolbox.com/

Versteeg, H. K., & Malalasekera, W. (2007). *An introduction to computational fluid dynamics : The finite volume method* (2nd ed.). Harlow, England ; New York: Pearson Education Ltd.

Walsh, P. C., & Leong, W. H. (2004). Effectiveness of several turbulence models in natural convection. *International Journal of Numerical Methods for Heat and Fluid Flow, 14*(5), 633-648.

White, F. M. (2003). *Fluid mechanics* (5th ed.). Boston: McGraw-Hill